NUI Galway
OÉ Gaillimh

Computational Studies of Hypericin and Porphyrin Derivatives for Photodynamic Therapy

Spectra, Membrane Simulations, and Protein Interactions

Emma Sofia Elisabeth Eriksson, M.Sc.

Thesis presented for the Ph.D. Degree
of the
National University of Ireland, Galway

School of Chemistry
National University of Ireland, Galway
August 2011

Head of School: Professor Paul V. Murphy
Supervisor: Professor Leif A. Eriksson

If we knew what it was we were doing, it would not be called research, would it?

- Albert Einstein

TABLE OF CONTENTS

ABSTRACT **1**

LIST OF PAPERS INCLUDED IN THIS THESIS **3**

LIST OF PAPERS NOT INCLUDED IN THIS THESIS **4**

LIST OF ABBREVIATIONS AND UNITS **5**

CHAPTER 1. INTRODUCTION TO PHOTODYNAMIC THERAPY AND PHOTOSENSITIZERS **7**

1.1. Photodynamic therapy (PDT) 7
1.1.1. Evolution of PDT 7
1.1.2. Mechanism of photosensitization in PDT 8
1.1.3. Photosensitizers 9
1.2. Hypericin 13
1.2.1. Chemical properties of hypericin 13
1.2.2. Mechanisms of photosensitization with hypericin 14
1.2.3. Hypericin as an antitumour and antiviral agent 17
1.2.3.1. Antitumour activity 17
1.2.3.2. Anitviral activity 18
1.2.4. Transportation and carriers of hypericin 19
1.2.4.1. Low-density lipoproteins 19
1.2.4.2. Serum albumins 20
1.2.4.3. Liposomes 21
1.2.5. Location and activity of hypericin in intracellular sites 21
1.2.5.1. Mitochondria 22
1.2.5.2. Endoplasmic reticulum (ER) 23
1.2.5.3. Cell membrane and nucleus 24
1.2.5.4. Lysosome 24
1.2.6. Modified hypericin derivatives 24
1.2.6.1. Hypericin derivatives with red-shifted absorption 25
1.2.6.2. Hypericin derivatives with modified solubility 26
1.2.6.3. Hypericin derivatives with enhanced ROS production 27
1.2.6.4. Hypericin combined with other photosensitizers 28
1.3. Tetrapyrrole compounds 29
1.3.1. Porphyrin and chlorin 29
1.3.2. Protoporphyrin and phytoporphyrin 30
1.3.3. Tookad 31
1.3.4. Foscan 32
1.3.5. Chlorin e6 and chlorin p6 32
1.4. Aims and objectives 35
1.4.1. Paper I 35
1.4.2. Paper II and IV 35
1.4.3. Paper VII 35
1.4.4. Paper III, V and VI 35

CHAPTER 2. THEORETICAL BACKGROUND OF COMPUTATIONAL CHEMISTRY 37
2.1. Quantum mechanics 37
2.1.1. The Schrödinger equation 37
2.1.2. Hartree-Fock (HF) 40
2.1.3. Basis sets 42
2.1.4. Density functional theory (DFT) 45
2.1.4.1. Hybrid methods 47
2.1.5. Time-dependent density functional theory (TD-DFT) 49
2.1.5.1. Performance of functionals in TD-DFT excited state calculations 50
2.2. Molecular mechanics 53
2.2.1. Principles of molecular mechanics 53
2.2.2. Molecular dynamics 55
2.2.3. Molecular docking 57
2.2.4. Homology modelling 58

CHAPTER 3. REDOX AND DEBROMINATION REACTIONS OF BROMINATED HYPERICIN 61
3.1. Computational methodology 61
3.2. Results and discussion 62

CHAPTER 4. PROPERTIES AND PERMEABILITY OF HYPERICIN AND BROMINATED HYPERICIN IN LIPID MEMBRANES 69
4.1. Computational methodology 69
4.2. Results and discussion 71

CHAPTER 5. SARCO(ENDO)PLASMIC RETICULUM Ca^{2+} ATPase IS A POSSIBLE TARGET FOR HYPERICIN 79
5.1. Computational methodology 80
5.2. Results and discussion 81

CHAPTER 6. CALCULATIONS OF ABSORPTION SPECTRA OF TETRAPYRROLE COMPOUNDS AND COMPUTATIONAL DESIGN OF NEW PHOTOSENSITIZERS FOR PDT 91
6.1. Computational methodology 92
6.2. Can range-separated and hybrid DFT functionals predict low-lying excitations? A Tookad case study 93
6.3. Predictive power of long-range corrected functionals on the spectroscopic properties of tetrapyrrole derivatives for PDT 99
6.4. Computational design of chlorin based photosensitizers with enhanced absorption properties 106

CONCLUSIONS 115

ACKNOWLEDGEMENTS 117

REFERENCES 119

ABSTRACT

Photosensitizing compounds with potential application in anticancer treatment with photodynamic therapy were investigated by means of computational methods in the studies presented in this thesis.

Hypericin and brominated derivatives were studied regarding possible reaction mechanisms and interactions with membranes and proteins. Monobrominated hypericin was found to possibly dissociate in an oxygen-independent reaction, providing an alternative pathway that can produce radical species in tumours. Hypericin, mono- and tetrabrominated hypericin showed strong preference for lipid membranes, in which monobrominated hypericin displayed the highest permeation, indicating that this molecule would have the highest probability to enter a cell through diffusion. Hypericin molecules that have the ability to reach the interior of a cell are prone to initiate damage to intracellular molecular targets, such as the endoplasmic reticulum Ca^{2+} ATPase SERCA, with which hypericin was found to interact strongly.

Benchmarking studies of functionals used in TD-DFT were performed in order to determine suitable methodologies for predicting absorption spectra of photosensitizing tetrapyrrole compounds. The studies provide an evaluation of the potential to use long-range corrected functionals in computer-assisted design of photosensitizers for photodynamic therapy. Based on the results from the benchmarking studies, modified chlorin derivatives with strong absorption in the therapeutic window of photodynamic therapy were designed, representing suitable starting points for further experimental evaluation.

The presented studies of hypericin and tetrapyrrole compounds provide detailed knowledge on possible reaction mechanisms, spectroscopic properties, and interactions with biomolecular systems. This information contributes to deep insight into the action of these compounds and can be of great importance in the development of photodynamic agents with improved therapeutic properties.

LIST OF PAPERS INCLUDED IN THIS THESIS

I. Eriksson, Emma S. E.; Guedes, Rita C.; Eriksson, Leif A. (2008) **Redox and debromination reactions of brominated hypericin.** *International Journal of Quantum Chemistry* 108, 1921-1929.
Reproduced by permission of John Wiley & Sons.
http://onlinelibrary.wiley.com/doi/10.1002/qua.21689/full

II. Eriksson, Emma S. E.; dos Santos, Daniel J. V. A.; Guedes, Rita C.; Eriksson, Leif A. (2009) **Properties and permeability of hypericin and brominated hypericin in lipid membranes.** *Journal of Chemical Theory and Computation* 5, 3139-3149.
Reproduced by permission of the American Chemical Society.
http://pubs.acs.org/doi/abs/10.1021/ct9002702

III. Tian, Boxue X.; Eriksson, Emma S. E.; Eriksson, Leif A. (2010) **Can range separated and hybrid DFT functionals predict low-lying excitations? A Tookad case study.** *Journal of Chemical Theory and Computation* 6, 2086-2094.
Reproduced by permission of the American Chemical Society.
http://pubs.acs.org/doi/abs/10.1021/ct100148h

IV. Eriksson, Emma S. E. and Eriksson, Leif A. (2011) **The influence of cholesterol on the properties and permeability of hypericin derivatives in lipid membranes.** *Journal of Chemical Theory and Computation* 7, 560-574.
Reproduced by permission of the American Chemical Society.
http://pubs.acs.org/doi/abs/10.1021/ct100528u

V. Eriksson, Emma S. E. and Eriksson, Leif A. (2011) **Predictive power of long-range corrected functionals on the spectroscopic properties of tetrapyrrole derivatives for photodynamic therapy.** *Physical Chemistry Chemical Physics* 13, 7207-7217.
Reproduced by permission of the PCCP Owner Societies.
http://pubs.rsc.org/en/content/articlelanding/2011/CP/C0CP02792H

VI. Eriksson, Emma S. E. and Eriksson, Leif A. (2011) **Computational design of chlorin based photosensitizers with enhanced absorption properties.** *Physical Chemistry Chemical Physics* 13, 11590-11596.
Reproduced by permission of the PCCP Owner Societies.
http://pubs.rsc.org/en/content/articlelanding/2011/cp/c1cp20715f

VII. Eriksson, Emma S. E. and Eriksson, Leif A. (2011) **Sarco(endo)plasmic reticulum Ca^{2+} ATPase (SERCA) is a possible target for hypericin.** Manuscript.

My contribution to the papers

Paper I-II, IV-VII: All calculations, analysis, and preparation of manuscripts.

Paper III: Interpretation of results and preparation of manuscript.

LIST OF PAPERS NOT INCLUDED IN THIS THESIS

VIII. Penketh, Philip G.; Baumann, Raymond P.; Shyam, Krishnamurthy; Williamson, Hugh S.; Ishiguro, Kimiko; Zhu, Rui; Eriksson, Emma S. E.; Eriksson, Leif A.; Sartorelli Alan C. (2011) **1,2-Bis(methylsulfonyl)-1-(2-chloroethyl)-2-[[1-(4-nitrophenyl)ethoxy]carbonyl]hydrazine (KS119): A cytotoxic prodrug with two stable conformations differing in biological and physical properties.** *Chemical Biology & Drug Design* 78, 513-526.

LIST OF ABBREVIATIONS AND UNITS

AEA	adiabatic electron affinity
B3LYP	Becke three-parameter (exchange), Lee, Yang and Parr (correlation)
BChl	bacteriochlorophyll
BHQ	di-*tert*-butylhydroquinone
BPheid	bacteriopheophorbide
Chl	chlorophyll
DFT	density functional theory
DPPC	dipalmitoylphosphatidylcholine
ER	endoplasmic reticulum
GGA	generalized gradient approximation
GTO	Gaussian type orbital
HDL	high-density lipoprotein
HF	Hartee-Fock
HOMO	highest occupied molecular orbital
IEF-PCM	integral equation formalism of the polarizable continuum model
LDA	local density approximation
LDL	low-density lipoprotein
LUMO	lowest unoccupied molecular orbital
MD	molecular dynamics
MM	molecular mechanics
NPe6	mono-L-aspartyl chlorin e6
PDB	Protein Data Bank
PDT	photodynamic therapy
QM	quantum mechanics
ROS	reactive oxygen species
SERCA	sarco(endo)plasmic reticulum Ca^{2+} ATPase
STO	Slater type orbital
TG	thapsigargin

TD-DFT	time-dependent density functional theory
THF	tetrahydrofuran

Å	Ångström = 10^{-10} m
eV	electron volt
fs	femtosecond = 10^{-15} s
K	Kelvin
kcal/mol	kilocalories/mol
kJ/mol	kilojoules/mol
nm	nanometer = 10^{-9} m
μm	micrometer = 10^{-6} m
μs	microsecond = 10^{-6} s

CHAPTER 1. INTRODUCTION TO PHOTODYNAMIC THERAPY AND PHOTOSENSITIZERS

In the studies reported herein, hypericin and tetrapyrrole compounds were investigated in the context of their potential application as photosensitizing agents in cancer therapy. This introductory chapter provides a general view of the treatment method and the photosensitizers included in the studies. The specific aims and objectives of the presented studies are given in the end of this chapter.

1.1. Photodynamic therapy (PDT)

1.1.1. Evolution of PDT

PDT is a medical technique used to treat both malignant and non-malignant disorders. Three components are required in PDT; light, oxygen, and a photosensitizer.

For several thousands of years, light therapy, also referred to as phototherapy, has been used in medical treatment of a large number of disorders.[1] After the introduction of light therapy came photochemotherapy, in which both light and a photosensitizer are required agents. Photochemotherapy is a well-known technique that has caught particular attention as an effective method to treat psoriasis using psoralen photosensitizers.[2] The early stages of formal PDT began with experiments performed on tumours and other skin disorders more than 100 years ago.[3, 4] In 1913 Meyer-Betz injected himself with hematoporphyrin and showed that this caused photosensitivity of the areas exposed to light.[5] In the 1970s PDT with hematoporphyrin derivatives were extensively developed and tested in mice and humans.[6-10]

Even to this day, tumours are often preferentially treated with PDT; the treatment can be specifically directed at cancerous tissues and is often faster, easier, and less painful than traditional cancer treatment. As light does not have the ability to reach deep into the body, superficial tumours have been the main targets so far. However, with new techniques such as endoscopes or fibre optic

catheters, light can also be used to treat tumours located in internal organs. Beyond anti-tumour therapies, PDT can be used to treat non-malignant conditions such as psoriasis,[11] acne,[12] and age-related macular degeneration,[13] as well as pre-malignant actinic keratosis.[14] Sterilization of virus-contaminated blood is another possible field of application.[15] PDT might also be used in antimicrobial treatment of local infections.[16, 17]

1.1.2. Mechanism of photosensitization in PDT

As seen in Figure 1.1, a modified Jablonski diagram shows possible photophysical processes and reactions for photosensitizers. Upon light irradiation, the photosensitizer is excited from the ground singlet state, S_0, to the first excited singlet state, S_1, (reaction **1**; Figure 1.1), followed by intersystem crossing (ISC) to the first triplet state, T_1 (reaction **4**; Figure 1.1). If intersystem crossing does not occur, the compound returns to the ground singlet state via emission of fluorescence (reaction **2**; Figure 1.1) or through radiationless transition (internal conversion; reaction **3**; Figure 1.1). The triplet state is usually long-lived, which gives enough time for reactions with the environment. In the presence of molecular oxygen (O_2), these reactions can generate reactive oxygen species (ROS), which act as to damage cells.

Reactions with molecular oxygen following the triplet state of the photosensitizer are classified as oxygen-dependent type I and type II reactions.[18] In general, an oxygen-dependent type I reaction involves initial hydrogen abstraction from the photosensitizer or electron transfer between the photosensitizer and a substrate, both of which generate free radicals or radical ions that, in turn, can react with molecular oxygen to form ROS, such as superoxide radical anions ($O_2^{\bullet-}$), hydrogen peroxide (H_2O_2), and hydroxyl radicals ($OH^{\bullet}$) (reaction **6**; Figure 1.1).

In oxygen-dependent type II reactions, the excitation energy of the photosensitizer is directly transferred to molecular oxygen, forming singlet oxygen when ground triplet state oxygen is excited to the first excited singlet state, while the photosensitizer returns to the ground singlet state (reaction **7**;

Figure 1.1). If no reactions with oxygen from the triplet state occur, the photosensitizer can return to the ground singlet state via emission of phosphorescence (reaction **5**; Figure 1.1).

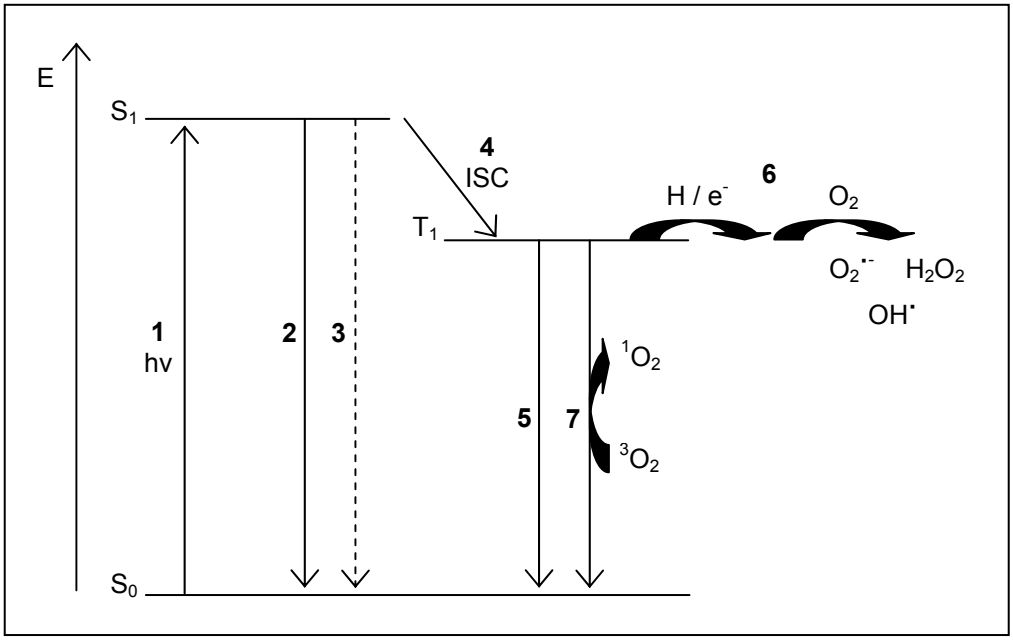

Figure 1.1. Modified Jablonski diagram displaying the photophysical processes of photosensitizers. **1**: Excitation, **2**: fluorescence, **3**: radiationless transition (internal conversion), **4**: intersystem crossing, **5**: phosphorescence, **6**: hydrogen/electron transfer between the triplet state photosensitizer and the environment, followed by reactions with molecular oxygen, **7**: energy transfer to ground triplet state oxygen.

1.1.3. Photosensitizers

An ideal photosensitizer is required to possess strong absorption at long wavelengths and have a high ROS quantum yield. It is however equally important that the photosensitizer is chemically stable and that it is non-toxic in the absence of light in order to avoid oxidative damage to healthy tissues that are not exposed to light. The photosensitizer should also preferably accumulate in tumour tissues and have a high clearance rate, in order to avoid long-lasting photosensitization.

Wavelengths of the light used in PDT are in the range of 600-900 nm,[19] and the specific wavelength depends on the red-most absorption peak of the photosensitizer. Despite the fact that many photosensitizers absorb significantly less in this region of the spectrum compared to shorter wavelengths, light at longer wavelengths is preferably used in PDT due to its beneficial properties. This light has the ability to reach deeper into tissues, hence enabling treatment of larger and less superficial tumours. The tissue penetration depth for light at 630 nm is about 2-3 mm whereas at 700-800 nm it is increased to 5-6 mm,[20] thus providing a deeper therapeutic effect. The stronger the light absorption at the wavelength used in PDT, the lower the required light dose. Another advantage with light at long wavelengths is that overlapping absorption of endogenous molecules, such as hemoglobin, is reduced. Wavelengths over 900 nm are usually not applicable in PDT as the energy of the photons decreases with increased wavelength and the energy must be enough to excite a photosensitizer.

Molecules constituting conjugated π-electron systems, created by alternating single and double bonds, enable light absorption and thus have the potential of being used as photosensitizers. Upon light absorption, an electron in a π-bonding molecular orbital is excited to a π-antibonding molecular orbital ($\pi \rightarrow \pi^*$). The most energetically favourable $\pi \rightarrow \pi^*$ transition occurs from the highest occupied π-bonding molecular orbital (HOMO) to the lowest unoccupied π-antibonding molecular orbital (LUMO). With an increased conjugated system, the energy gap between HOMO and LUMO is reduced and less energy is required for excitation. The absorption is subsequently shifted to longer wavelength.

A crucial requirement for a photosensitizer is that it has the ability to produce ROS, of which singlet oxygen is one of the most predominantly formed species. In order to produce singlet oxygen, the energy of the triplet state of the photosensitizer must be higher than the energy needed to excite oxygen from its ground triplet state to the first singlet state (0.98 eV[21]). The ability of many photosensitizers to selectively accumulate to a high extent in

tumour tissue and the fact that only the region of the body that is subject to treatment is irradiated make PDT a highly specific treatment method due to the short lifetime and subsequent limited migration of ROS. Singlet oxygen, as an example, has a lifetime of <0.04 μs that indicates a radius of action of <0.02 μm.[22] ROS induce controlled cell death via apoptosis or sudden cell death via necrosis. The specific mode of cell death depends on the location of the photosensitizer, the drug and light dose, and the cell line.[23, 24]

Photosensitizers often have the ability to selectively accumulate, consequently localizing the action of PDT to tumour tissue rather than to healthy tissue. This selectivity is mainly due to the physiological differences between tumour and normal tissues. Tumours display a large interstitial volume, contain a large number of receptors for lipoproteins[25, 26] that are common carriers of photosensitizers, and contain a larger amount of newly synthesized collagen[27] that photosensitizers, such as hypericin[28] and porphyrins,[29] have high affinity for. Tumours also have low extracellular pH[30, 31] that increases the lipophilicity of some photosensitizers due to protonation and thereby enhances the uptake into tissues.[32] In order to facilitate the uptake into tumours, formulations with the photosensitizer conjugated to antibodies, low-density lipoproteins (LDL) or liposomes are used.[33]

The first hematoporphyrin mixtures used as photosensitizers were in a later stage purified to form Photofrin® (Porfimer sodium), a mixture of monomers, dimers and oligomers of porphyrins linked together by ether, ester or carbon-carbon bonds.[34, 35] Photofrin was the first photosensitizer for which marketing clearance was obtained and it is the most widely used photosensitizer in PDT, approved for treatment of esophageal, bladder, gastric, cervical, and lung cancers.[36] Although Photofrin has been successfully used in PDT, it also possesses several drawbacks that make it a non-ideal photosensitizer. The compound possesses weak absorption at long wavelengths, which results in non-optimal tissue penetration and high required drug and light doses. Photofrin also displays weak tumour selectivity and causes long-lasting skin photosensitization.

Hematoporphyrin derivatives such as Photofrin are classified as first generation photosensitizers, and in order to overcome the problems associated with these compounds, second generation photosensitizers with improved PDT properties, such as strong light absorption at long wavelengths, high ability to generate ROS and minimal side effects, have been the focus of extensive research effort during the last decades. Development of photosensitizers that can improve PDT as a cancer treatment method would, apart from making existing treatment schemes more efficient, also enable advances to use the method for treatment of several additional cancer types. Photosensitizers are usually developed starting from already available photosensitizing compounds and through structural modifications the photodynamic properties, solubility, and synthetic aspects are modulated. A majority of the photosensitizers that have reached the preclinical stage are cyclic tetrapyrrole compounds (porphyrin based), but also non-porphyrin photosensitizers exist.

Sections 1.2 and 1.3 give a detailed account of the photosensitizers that were included in the studies presented herein.

1.2. Hypericin

1.2.1. Chemical properties of hypericin

Hypericin (1, 3, 4, 6, 8, 13-Hexahydroxy-10, 11-dimethylphenanthro[1, 10, 9, 8-opqra]perylene-7, 14-dione) (Figure 1.2) belongs to the group of non-porphyrin photosensitizers and is one of the most powerful photosensitizers found in nature. Hypericin is one of several natural phenanthroperylene quinones found in species of the genus *Hypericum* from which extracts have been utilized for thousands of years in traditional medicine in treatment of skin diseases and wounds, mental disorders, and several other conditions.[37] Preparations containing St. John's wort (*Hypericum perforatum*) were early used as "mood-altering substances" and are even today successfully used in treatment of depression.[38] Several species of *Hypericum* have been observed to cause severe photosensitization, with symptoms such as skin irritation, edemas, increased body temperature and eventually death (the symptoms are collectively called *hypericism*) in animals ingesting large quantities of *Hypericum* weed and being exposed to strong sunlight.[39-41] The photosensitizing effect is due to the chromophoric system of the phenanthroperylene quinones that absorbs light, and hydroxyl- and alkyl group substituents contribute to enhance the photosensitizing properties of the compounds.

Hypericin, the compound that is mainly responsible for the photosensitizing action, was first isolated from St. John's wort in 1911,[42] its chemical formula ($C_{30}H_{16}O_8$) was reported in 1942,[43] and the correct structure was published in 1950.[44] In plants the compound is found in the form of *bay*-hypericinate ions that bind potassium and form dark coloured granules.[45] A *bay*-hydroxyl group (Figure 1.2) of hypericin displays a pK_a value of 1.8 in aqueous systems,[37] indicating that the compound exists in its deprotonated form at physiological pH. Deprotonation of the remaining hydroxyl groups occurs at pH values around 9.[37]

As the hypericin content in plants is very low, synthesis is preferable. The first full synthesis of hypericin was performed by Brockmann et al. in 1957.[46]

The precursor of hypericin, emodin anthrone, can be obtained either from reduction of emodin extracted from the bark of breaking buckthorn (*Cortex frangulae*),[47] or from synthesis.[46, 48]

Hypericin also exists in some insect species in which the function might be to protect the organism against sunlight by contributing to dark pigmentation of the epidermis.[49] Compounds structurally related to hypericin have, apart from in *Hypericum* species, been found in fungus,[50] crinoids,[51, 52] lichens,[53, 54] buckwheat,[55] and flour beetles.[49]

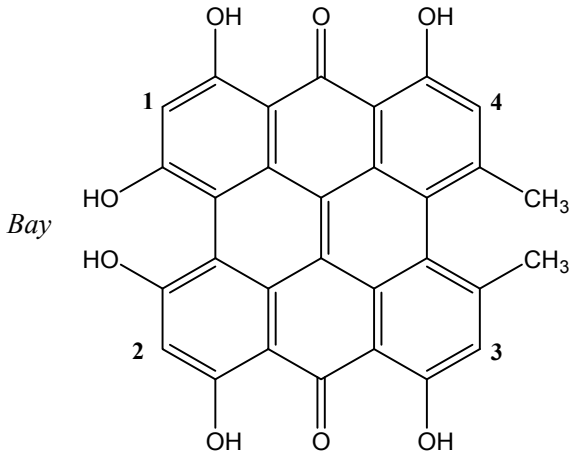

Figure 1.2. The hypericin molecule. The numbers 1-4 indicate the positions where bromine substitution was modeled (IUPAC labeling: positions 2, 5, 9, 12).

Although the potential of using hypericin in combination with light in medical therapy has been known for a long period of time, it was not until about 20 years ago that it was discovered to possess antitumour and antiviral activity associated with light. This has led to the proposal that hypericin can be utilized as a photosensitizer in PDT.

1.2.2. Mechanisms of photosensitization with hypericin

The property of hypericin that makes it a powerful photosensitizer is its ability to generate singlet oxygen and other ROS in the presence of light. However, it

is still not clear by which mechanism the molecule acts. Numerous pathways that could explain the strong activity observed for hypericin have been proposed and investigated experimentally and theoretically. The results from the studies indicate that most probably not one single mechanism exists but several acting in parallel.

Hypericin exhibits strong absorption at 500-600 nm,[56] with a maximum absorption at 590 nm.[57] This absorption peak corresponds to excitation from the ground singlet state to the first excited singlet state. The second lowest excitation is found at 425-485 nm,[56] with the maximum absorption at 480 nm.[57] After excitation to an excited singlet state the molecule relaxes to the first excited singlet state from which the molecule can easily be converted to the first triplet state through intersystem crossing (cf. Figure 1.1). The difference between the first excited singlet and the first triplet state is approximately 210 nm, corresponding to 0.62 eV.[58] From the triplet state, the reaction can follow different pathways, of which the two most studied are oxygen-dependent type I and type II reactions[59] that generate ROS (Figure 1.3).

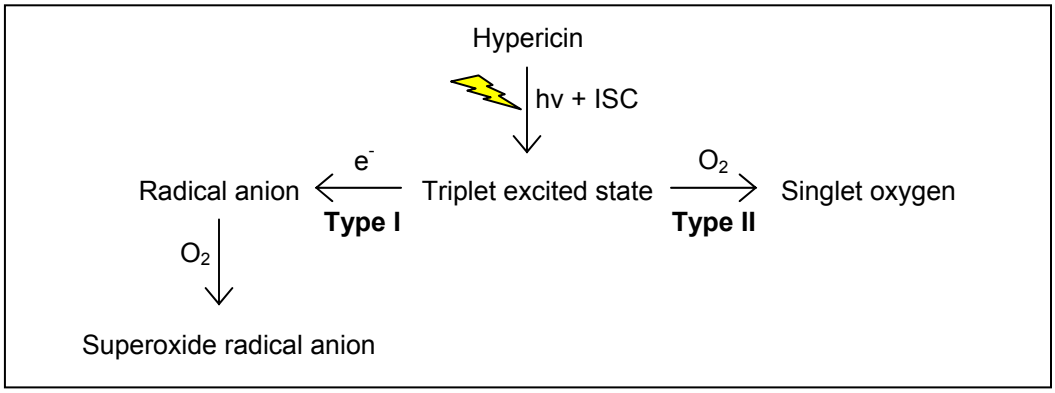

Figure 1.3. Oxygen-dependent type I and II reactions for hypericin.

In oxygen-dependent type I reactions, the hypericin molecule is in its triplet state reduced by an electron-donor, generating a hypericin semiquinone radical anion that is prone to react with molecular targets. The hypericin radical anion has been detected in electron paramagnetic resonance experiments after

photoactivation and was found to be predominantly formed under anaerobic conditions at high hypericin concentrations.[60, 61] Under aerobic conditions, the hypericin radical can reduce molecular oxygen to produce reactive superoxide radical anions.[60] Theoretical data indicates that the reaction in which molecular oxygen extracts an electron from the hypericin radical anion is associated with an energy gain, suggesting that this is a possible reaction.[58] This finding is supported by experimental observations.[62, 63] The superoxide radical anion can be further transformed into hydrogen peroxide and hydroxyl radicals. Hypericin has been found to produce hydrogen peroxide.[64]

In oxygen-dependent type II reactions, the triplet state hypericin molecule is quenched by molecular oxygen, resulting in generation of singlet oxygen and the regeneration of hypericin in its ground state. Energetically, this has also been shown to be a viable route.[58] However, depending on the local environment, this process may compete with the type I reaction in which the electron affinity of hypericin strive to generate hypericin in the reduced form. The quantum yield for formation of singlet oxygen was first estimated to be as high as 0.73,[65, 66] but the number has later been revised to 0.36 in ethanol and less than 0.02 in water.[67] In liposomes, the quantum yield is 0.35-0.43.[68 69]

Another suggested mechanism, apart from the oxygen-dependent type I and type II reactions, is that the excited hypericin molecule is ionized by direct transfer of an electron to molecular oxygen, generating superoxide radical anions and hypericin in the form of a radical cation.[62, 70] Oxygen does not have the ability to oxidize the hypericin molecule directly from the excited singlet state, but from the triplet state oxidation is possible.[58]

Hypericin in its triplet state can also be reduced by another hypericin molecule, a reaction that generates a hypericin radical anion and a hypericin radical cation.[70] This auto-ionization is possible if the second hypericin molecule is also in the triplet state.[58] However, this reaction would require a high local concentration of hypericin. Photogenerated protons that are transferred from the hypericin molecule upon irradiation can also play important roles in the activity of hypericin as it has been found to acidify the surrounding.[71-75]

1.2.3. Hypericin as an antitumour and antiviral agent

1.2.3.1. Antitumour activity

The antitumour activity of hypericin has been demonstrated on various carcinoma cell lines and tumours in the presence of light. In 1990 Thomas et al. performed the first *in vivo* experiment with hypericin, which showed destruction of mammary carcinoma cells in mice.[76] *In vivo* experiments on mice with transplanted squamous cell carcinoma tumours injected directly with hypericin showed potential of using hypericin in treatment of recurrent or inoperable cancers in head and neck.[77, 78] Decreased tumour growth of unresectable pancreatic cancer in mice has been reported as well.[79] A small clinical trial with hypericin intralesionally injected into skin cancer carcinomas (basal cell carcinoma and squamous cell carcinoma) in humans and irradiated with visible light resulted in promising tumour regression.[80]

The activity of hypericin on mouse mammary carcinoma cells was early shown to be both light and oxygen dependent, and the photosensitizing effect was found to be equivalent to that of Photofrin.[81] This was followed by numerous studies that showed that hypericin also possesses strong *in vitro* activity on neoplastic cells,[82] pulmonary squamous cell carcinoma, melanoma, colon adenocarcinoma, oral squamous cell carcinoma, breast adenocarcinoma, fibrosarcoma[83] bladder carcinoma,[84] skin carcinoma, and cervix carcinoma.[85] The research interest in hypericin as a cytotoxic agent has increased in recent years and additional *in vitro* studies have shown light-dependent activity of hypericin on cells such as rhabdomyosarcoma,[86] hepatoblastoma and pediatric hepatocellular carcinoma,[87] human renal carcinoma,[88] and umbilical endothelial and glioma cells.[89]

The ability of hypericin to selectively accumulate in tumour tissue has suggested a potential application in photophysical diagnosis, a useful technique to detect early stage tumours in order to initiate suitable treatment. Tumours can be imaged by the fluorescence from hypericin and clinical studies performed to detect bladder tumours showed high sensitivity and specificity.[90-92]

1.2.3.2. Anitviral activity

Apart from the toxicity against tumours, hypericin also displays antiviral activity. Enveloped viruses such as human immunodeficiency virus (HIV),[93-98] sindbis,[94, 95] murine cytomegalo,[94, 95] hepatitis B,[99] herpes simplex,[100-102] vesicular stomatitis,[98, 101] influenza A,[98, 100] radiation leukemia,[93, 103] and equine anemia[104] viruses respond to treatment with hypericin and light *in vitro*. Toxicity against non-enveloped viruses has not been observed,[100, 101] indicating that the antiviral activity involves viral lipid membrane structures. Inactivation of viral function has been suggested to occur through inhibition of viral fusion function,[98] or through disturbance in virus shedding, budding or assembly at the cell membrane.[93, 105] Cross-linking of viral membrane proteins have also been suggested,[98, 99] as well as inhibition of virus replication, as shown for HIV.[93, 106]

In vivo studies on the antiviral activity of hypericin have been performed with diverse outcomes. Studies on the action of hypericin against herpes simplex,[100] radiation leukemia,[105] Friend leukemia,[93, 100, 105, 107] and murine leukemia[93] viruses in mice have shown positive results, and several early studies on the activity of hypericin against HIV in humans reported preliminary results that indicated potential application in the therapeutically field.[108-111] However, more recent phase I studies of HIV and hepatitis C infected individuals showed no antiretroviral activity and instead severe phototoxicity.[112, 113]

The potential of using hypericin as an antiviral drug in humans is considered to be limited due to the fact that the light does not have the ability to reach all regions of the body. In attempts to overcome this problem experiments have been performed with the aim to investigate the possibility to place light-generating molecules such as luciferin and luciferase in the proximity of the hypericin molecule or covalently bound to it in order to fulfil the requirements of PDT.[114, 115] However, the generated chemiluminiscent light was not strong enough to achieve antiviral activity.

Despite the clear limitations of hypericin as an antiviral drug *in vivo* it might instead be of interest *ex vivo* in the field of virus-contaminated transfusion

blood as HIV[116] and bovine viral diarrhea viruses[117] in blood has been inactivated by treatment with hypericin and light. However, high doses of hypericin are required to obtain effective antiviral activity and damage to the red blood cells caused by irradiation has to be considered in connection to this and has been an obstacle in the development of this technique.

1.2.4. Transportation and carriers of hypericin

Transportation of drug molecules in the body, often in assistance of a carrier, and the intracellular location depend on the properties of the molecules. For drug molecules to reach possible cellular targets they need to be able to penetrate the plasma membrane of the cell. The exact target for hypericin and the transportation in the body are not yet fully understood, and various possible cellular targets and carriers have been suggested.

Hypericin can penetrate the plasma membrane through diffusion.[81] However, the molecule is highly hydrophobic and insoluble in aqueous solutions and would preferably interact with biological molecules in the blood that could also assist in entering cells. Hypericin is insoluble in water but easily dissolves in organic solvents such as alcohols.[118] Upon addition of water the hypericin molecules aggregate and form multimers, leading to dramatic changes in absorption and emission properties.[118] Photodynamic properties, such as generation of singlet oxygen, are also negatively altered by the presence of water.[119] At low concentrations of hypericin in solution dimers are formed,[119] whereas at higher concentrations H-aggregates consisting of at least four molecules positioned face to face have been observed.[118] Interaction with biological molecules would help to solubilise the molecule and prevent aggregation, which would otherwise suppress the activity of the molecule.

1.2.4.1. Low-density lipoproteins

Hypericin accumulates most probably in LDL and to a lower extent in high-density lipoproteins (HDL) when administrated into the blood stream.[120]

Human plasma LDL has been found to be high-capacity carriers for several photosensitizers used in PDT.[121-123] As many as 20-30 non-aggregated hypericin molecules have the ability to bind to and accumulate in each LDL molecule, possibly in the interfacial lipid region between the surface and the core.[124, 125] The activity of the hypericin molecules is probably retained also inside the LDL as the molecules do not aggregate. As rapid cell proliferation and membrane growth, which are associated with fast-growing tumour cells, require high turnover of cholesterol, normally carried by LDL, an enhanced expression of LDL receptors is observed in these cells.[25, 26] LDL receptor endocytosis would subsequently be a possible mechanism by which hypericin carried by LDL enter cells. The uptake of hypericin into cells is higher in the presence of LDL and when the number of LDL receptors on the cell surface is increased.[126] Taking advantage of this, PDT treatment could be directed to tumour tissues using LDL accumulating photosensitizers such as hypericin as molecules attached to LDL would to a higher extent be taken up by tumour cells than normal cells.

1.2.4.2. Serum albumins

Human serum albumin transports several substances in the blood, such as metals, fatty acids, amino acids, hormones, and many therapeutic drugs.[127] Serum albumins as carriers of various drug molecules and the interactions with those have been extensively studied. Detailed information on interactions with hypericin are available,[118, 128-131] but hypericin accumulates to a lower extent in human serum albumin than in LDL.[120] Serum albumin may release the carried substance when it reaches the target tissue, and the carried molecules are possibly taken up by the tissues through diffusion. However, hypericin binds strongly to human serum albumin and this may affect the number of molecules available for diffusion into the target tissue.

1.2.4.3. Liposomes

The use of liposomes as carriers of hydrophobic drug molecules has been shown to enhance the delivery and uptake into target tissues.[132] These formulations are particularly advantageous for the delivery of photosensitizers with low water solubility, as aggregation is prevented and the molecules can be delivered to the target tissues in their monomeric form.[33, 133] Hypericin binds easily to the lipid phase of liposomes,[69] and the light absorbance is red-shifted[134] and significantly enhanced[69] for hypericin embedded in liposomes compare to aqueous solution.

Second generation photosensitizers bound to liposomes or antibodies constitute a new class of photosensitizers, third generation photosensitizers, that can improve PDT treatment.

1.2.5. Location and activity of hypericin in intracellular sites

In order to study how photosensitizers act, it is crucial to determine where in the cell they localize. As the ROS generated from the photoreactions have short lifetimes and thus only diffuse very short distances, the site of action is in the very close proximity to the location of the photosensitizer. Studies have found hypericin in almost all cell components and the exact intracellular target is still not determined. The exact mechanism of cell death in hypericin-treated cells also remains to be fully examined. Apoptosis is the most commonly observed mechanism by which hypericin treated cells undergo cell death, but if the hypericin or light dose is increased, the mechanism can be shifted to necrosis.[135]

The hydrophobic character of the hypericin molecule indicates that it would preferentially accumulate in membranes. Hypericin has recently been shown to interact strongly with cholesterol and form tight complexes due their common planar structures that allow for π electron interactions.[136] The presence of cholesterol can hence contribute to the preferred location of hypericin in lipid membranes. The hypericin molecules were found in large concentrations in cholesterol rich domains rather than in less ordered regions with lipids. Viral membranes have been indicated to be targets for hypericin in viruses as non-

enveloped viruses are not inactivated,[100, 101] giving further evidence for the preference for membrane accumulation. Hypericin can cause damage to membranes by initiating lipid peroxidation reactions[137-139] or depolarization of the membrane (decreased plasma membrane potential), or reducing the activity of the Na^+, K^+-ATPase,[139] effects that seriously influence the condition of a cell.

1.2.5.1. Mitochondria

Mitochondria are likely to be possible targets for hypericin in which it accumulates.[140-142] Various mitochondrial enzymes have been shown to be inhibited[141, 143] or released[144] upon treatment with hypericin. Hypericin has also been shown to damage the electron transport chain in mitochondria, with the primary target indicated to be the quinone reducing centre Q_i in complex III (cytochrome bc_1) where it acts as a possible redox substrate.[145] The photodamage is possibly initiated by the formation of a hypericin semiquinone radical anion as a result of electron donation at Q_i.

Cells treated with hypericin show a decrease in intracellular pH,[144, 146] an observation that can be a result of a possible attempt to preserve mitochondrial functionality by pumping protons out of the mitochondria by the F_1F_0-ATPase.[147] Another possible cause of the pH drop is proton transfer from the excited state hypericin molecule.

Mitochondrial pathways are involved in many apoptosis cascades in PDT-treated cells, also when photosensitizers are not located in mitochondria, indicating that mitochondria play an essential role. Stimuli from intra- and extracellular stresses results in mitochondrial outer membrane permeabilization followed by release of apoptogenic molecules such as cytochrome c into the cytosole, which has been detected in cells treated with hypericin.[135, 148] The release of cytochrome c initiates a cascade of events that eventually ends up in apoptosis.[24, 135, 149, 150] Apoptosis pathways can also be activated by death receptors in cells treated with hypericin.[151-153] Extrinsic “death” signals such as tumour necrosis factor (TNF), TNF related apoptosis inducing ligand (TRAIL)

and Fas ligand (FasL) can bind to receptors at the cell surface and recruit proteins and caspases, forming a death-inducing signalling complex (DISC) that in turn activates apoptosis cascades involving a series of caspases.[154]

1.2.5.2. Endoplasmic reticulum (ER)

As hypericin interacts strongly with cholesterol,[136] cholesterol trafficking[155] can explain that hypericin has been found in various intracellular membrane sites. Intermembrane trafficking of hypericin in complexes with cholesterol can thus mediate transport of hypericin from the mitochondria to the ER.[147]

Studies have confirmed that the ER and the Golgi apparatus are highly probable sites for hypericin accumulation.[85, 156, 157] PDT-treatment with hypericin provokes a rapid rise in cytosolic Ca^{2+} concentration, which is due to release of Ca^{2+} from intracellular stores such as ER, possibly as a result of oxidative damage.[158] A subsequent reduction in Ca^{2+} concentration in the ER is observed. A consequence of decreased Ca^{2+} levels in the ER is "ER stress", which is characterized by disruptions in folding, modifying and sorting of newly synthesized proteins. Irreversible ER stress can lead to initiation of the unfolded protein response, which in turn can initiate cascade pathways that lead to apoptosis.[159] Hypericin has been shown to initiate the unfolded protein response.[160]

The altered Ca^{2+} levels were found to be related to a significant reduction in protein levels of the sarco(endo)plasmic reticulum Ca^{2+} ATPase (SERCA), an important membrane protein that catalyzes ATP-dependent transport of Ca^{2+} into the lumen of the ER and sarcoplasmic reticulum (SR) in order to maintain a constant low resting concentration of Ca^{2+} in the cytosole. Singlet oxygen generated by hypericin is a probable cause of oxidative damage to SERCA.

Mitochondrial apoptosis pathways were found to be activated downstream from the SERCA degradation, indicating that ROS induced damage of SERCA are the initial events that trigger the apoptosis cascade.[158, 161] After depletion of intracellular Ca^{2+} stores caused by hypericin, the proapoptotic BAX and BAK proteins are essential for initiation of mitochondrial outer membrane

permeabilization and subsequent apoptotic cell death.[158, 161] In cells deficient in these proteins a non-apoptotic pathway not involving caspases is followed, which leads to autophagic cell death. Autophagic cell death is initiated as an attempt to remove oxidatively damaged organelles, as this is a natural survival mechanism. Apoptotic and autophagic cell death are likely to function in parallel, with autophagic cell death possibly acting as a backup mechanism.

1.2.5.3. Cell membrane and nucleus

Hypericin also accumulates in the cell membrane due to its hydrophobic character.[81, 134, 162, 163] It has been suggested that only after long-term incubation the hypericin molecule can penetrate the plasma membrane and eventually reach the nucleus.[162] However several additional studies have reported that hypericin easily locates in the nucleus.[134, 162, 163] Hypericin has a preference for guanine and adenine nucleic bases to which it, through its hydroxyl groups, forms hydrogen bonds.[164-166] Several photosensitizers are known to damage nucleic acids.[167-170]

1.2.5.4. Lysosome

Hypericin encapsulated in LDL has been found to be transported to lysosomes[153, 171] as cholesterol, which is normally carried by LDL, is transported to this site for hydrolysation. Hypericin causes lysosomal damage, upon which lysosomal proteases such as cathepsins are released, as an initiation step that triggers the mitochondrial apoptosis pathway.[140] Although hypericin accumulates in lysosomes, this site is not believed to be the primary target.

1.2.6. Modified hypericin derivatives

Hypericin possesses several properties that make it a promising photosensitizer for application in PDT. The molecule absorbs strongly at fairly long wavelengths, displays minimal dark toxicity, accumulates selectively in tumour tissue, and causes phototoxicity in tumours. However, hypericin displays two

main drawbacks. First, the absorption lies slightly outside the therapeutic window of PDT. A shift in wavelength would, apart from increase the light penetration depth into tissues, also prevent competing absorption by heme proteins and other endogenous chromophores at shorter wavelengths. Secondly, the molecule is highly insoluble under physiological conditions and this likely affects the photodynamic efficiency. The efficiency of PDT with hypericin can also be enhanced by an increased quantum yield of ROS formation.

As extraction of hypericin from plants is very expensive and modifications of the hypericin molecule often are difficult to carry out, syntheses of modified hypericin derivatives are preferentially done by introducing modifications at an early stage of the synthesis, starting from modified emodin derivatives.

A large number of second generation hypericin derivatives have been developed. However, the requirements for an ideal photosensitizer in all aspects are difficult to fulfil and result in that only a small number of compounds have the potential for effectively being used in PDT. The following sections provide a summary of second generation hypericin derivatives that have shown promising PDT properties.

1.2.6.1. Hypericin derivatives with red-shifted absorption

The absorption wavelength of hypericin can be shifted either by substituting the aromatic protons by conjugated substituents or by extending conjugation via the two methyl groups. Numerous studies have reported hypericin derivatives with red-shifted absorption, however, a majority of the derivatives have not been found to possess sufficient photosensitizing activity. Derivatives that have been found to exhibit red-shifted absorption in addition to promising photosensitizing potential, with respect to their ability to produce ROS, include a styrene derivative[172] and several heterocyclically substituted derivatives.[173] Hypericin derivatives with fused heterocycles are thought to display red-shifted absorption due to the extended conjugated π-system, but none of the synthesized compounds had the ability to both shift the absorption and maintain the photosensitizing activity of hypericin.[174, 175] One of the compounds was

shown to be more active than hypericin in the sense of ROS production, but did not display any shift in absorption.
Although some hypericin derivatives display red-shifted absorption, the shift is not large enough to offer any significant improvement in light penetration.

1.2.6.2. Hypericin derivatives with modified solubility

Many hypericin derivatives have been developed with the aim to increase the water solubility that would make intravenous injection possible. Although hydrophilic compounds have the advantage of being soluble under physiological conditions, a certain degree of lipophilicity is a requirement for cellular uptake, as the molecules must have the ability to penetrate the plasma membrane. Several hydrophilic derivatives have been found to be inactive or less cytotoxic than the parent hypericin molecule, most probably due to a decreased level of drug uptake into cells.[85, 171] However, a water-soluble hypericin-polyvinylpyrrolidone (PVP) complex has showed increased phototoxicity on crayfish neurons compared to the parent hypericin compound,[176] and has been shown to display appropriate properties for being used as a fluorescent dye in bladder cancer diagnosis.[177] A carbohydrate substituted hypericin derivative with enhanced solubility, highly effective ROS production and possible interactions with DNA displays one of the most promising hypericin derivatives that have been developed.[178]
Due to the presence of various substituents, the binding properties to biomolecules such as plasma constituents might be altered compared to unsubstituted hypericin. Hydrophilic derivatives, in general, display a clear preference for HDL instead of LDL.[85] Hypericin derivatives with increased lipophilicity, in the form of long lipophilic chains, have been synthesized as well, of which one of the derivatives displayed phototoxicity and cellular uptake into cancer cells similar to that of unsubstituted hypericin.[179]

Most second generation hypericin derivatives include substitutions at the hypericin core in order to maintain the acidity of the hydroxyl groups. However, a small number of hypericin derivatives with substituents at the

hydroxyl groups have been synthesized. A hypericin derivative with all six hydroxyl groups methylated was found to increase the singlet oxygen yield compared to unsubstituted hypericin.[180] Due to the decreased hydrophobicity of this derivative, it was shown to bind more easily to HDL than LDL,[85] and the binding to liposomes was decreased.[180]

A hypericin derivative with two propionyl dicyclohexylurea groups is thought to display enhanced hydrogen bond capacity that could influence binding to solubilising agents or cellular targets due to the presence of four additional carbonyl groups.[181] This compound, as well as a hypericin substituted with dithioacetal moieties, displayed ROS production comparable to that of hypericin and are believed to possess promising photodynamic properties.[181] A cationic quaternary trimethyl anilinium hypericin derivative has been found to be a potent bacteriocidal photosensitizer active at low concentrations.[182]

1.2.6.3. Hypericin derivatives with enhanced ROS production

The ROS production can also be altered by other substituents than the ones discussed above. This can be accomplished by for example heavy-atom substitution of the aromatic protons as this enhances intersystem crossing to the triplet state, consequently leading to increased formation of ROS.[183]

Brominated hypericin derivatives have been suggested to meet some of the requirements of improved photosensitizers. Di-, tri- and tetrabromohypericin exhibit antiviral activity against herpes simplex and influenza viruses.[184] Tetrabrominated hypericin possesses potent toxicity on cancer cells[156] and displays an increased quantum yield of singlet oxygen formation compared to hypericin.[180, 183] Bromination, as well as chlorination and fluorination, increases the electron affinity of hypericin and can thus increase the quantum efficiency of superoxide formation through oxygen-dependent type I reactions.[185] Monobrominated hypericin displays slightly red-shifted absorption spectra compared to hypericin, and with increased level of bromination a small increase in the shift is observed.[185, 186] Tetra-brominated hypericin exhibits a higher binding constant to liposomes than unsubstituted hypericin, as well as higher

singlet oxygen quantum yield when bound to liposomes.[180] Brominated hypericins are possible to synthesize[186] and are naturally found in the deep sea crinoid *Gymnocrinus richeri*.[52]

1.2.6.4. Hypericin combined with other photosensitizers

Apart from the commonly synthesized second generation hypericin derivatives, attempts have been made to combine hypericin with other photosensitizers, either involving covalently bound complexes or formulations containing mixtures of photosensitizers.

Hypericin has been bound to porphyrins in order to generate a photosensitizing agent that could possibly enhance the activity of both compounds.[187] One of the synthesized diastereomeric compounds displayed higher ability to generate singlet oxygen and other ROS compared to hypericin. Another study has shown that the photosensitizing effects can be enhanced by combining several photosensitizers in the same treatment to achieve synergistic effect. Treatment of cancer cells with a combination of hypericin and 5-aminolevulinic acid (5-ALA) irradiated with white light was found to significantly increase the phototoxic effect compared to treatment with 5-ALA alone.[188]

1.3. Tetrapyrrole compounds

1.3.1. Porphyrin and chlorin

Tetrapyrrole compounds constitute, like hypericin, highly conjugated systems that enable light absorption. Porphyrins are based on a macrocycle of four pyrrole rings connected by methine bridges (Figure 1.4A). Porphyrins absorb strongly in the visible region, corresponding to the B-band (Soret band), and also at longer wavelengths, corresponding to the Q-band. The Q-band consists of two components of which the one at longest wavelength corresponds to excitation from the ground singlet state to the first excited singlet state. For unsubstituted porphyrin (porphin) the strongest absorption peak is positioned at 397 nm, whereas the weaker red-most absorption peak is positioned at 617 nm.[189] Protoporphyrin IX and phytoporphyrin (Section 1.3.2) are two naturally occurring porphyrin based compounds.

Chlorin (17,18-dihydroporphyrin; Figure 1.4B) differs from porphyrin in that a double bond has been reduced, generating a macrocycle containing three pyrrole and one pyrroline ring. Unsubstituted chlorin displays its red-most absorption at 626 nm, i.e. slightly red-shifted absorption compared to porphyrin.[190] Chlorin and bacterichlorin, in which two double bonds at opposite pyrrole rings have been reduced (7,8,17,18-tetrahydroporphyrin), are precursors to the natural photosynthetic pigments chlorophyll (Chl) and bacterichlorophyll (BChl).

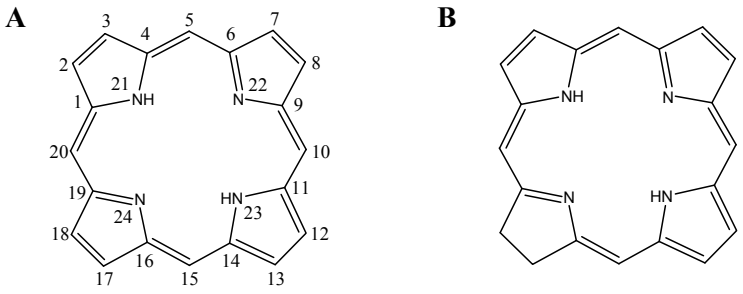

Figure 1.4. Schematic figures of (A) porphyrin and (B) chlorin.

In addition to Photofrin, the most widely used photosensitizer, many second generation tetrapyrrole photosensitizers with promising photodynamic properties have been developed, of which some have been approved for PDT. Chlorin based compounds hold more promise to be utilized as photosensitizers in PDT due to the general feature that chlorin (and bacterichlorin) compounds display the red-most absorption maximum at longer wavelengths compared with the corresponding porphyrin compounds, and the absorption is also strengthened. This enables deeper light penetration into tissues and requires lower drug and light doses, hence provides a more efficient PDT treatment. The deeper light penetration depth indicates that chlorin photosensitizers can be suitable for treatment of large and bulky tumours.

Second generation chlorin photosensitizers that have shown promising photodynamic properties include Foscan® (Section 1.3.4) and mono-L-aspartyl chlorin e6 (Section 1.3.5). One of the most promising chlorin based second generation photosensitizers is Tookad, a bacteriopheophorbide (BPheid) containing palladium (Section 1.3.3).

More complex tetrapyrrole compounds such as metalloporphyrins (e.g. Lutrin), porphycenes, purpurins (e.g. Purlytin), and phthalocyanines have also been developed, of which some have reached clinical trials.

The photosensitizing tetrapyrrole compounds discussed in the following sections were included in the studies presented herein.

1.3.2. Protoporphyrin and phytoporphyrin

Protoporphyrin IX (Figure 1.5A) is one of the most essential porphyrin compounds in nature as it forms the heme group of hemoglobin, the oxygen carrier in the blood, upon binding of iron. The first photosensitizer used in PDT, hematoporphyrin (Section 1.1), is a porphyrin compound structurally related to protoporphyrin IX. While protoporphyrin IX can be used as a photosensitizer, it is administered in the form of a prodrug, 5-ALA (Levulan®) that is enzymatically transformed into protoporphyrin IX in the biosynthesis of protoheme.[191] 5-ALA has been extensively studied and successfully used in

PDT treatment of skin disorders and cancer[192] since 1990 when it was subject to initial clinical trials.[193] Due to a reduced activity of ferrochelatase, the enzyme that incorporates iron into protoporphyrin IX, in tumour cells, the accumulation of protoporphyrin IX is greater than in normal cells.[194] Second-generation 5-ALA derivatives with increased lipophilicity have been developed in order to enhance cellular uptake. The methyl ester (Metvix®) has been approved for arctinic keratosis[195, 196] and basal cell carcinoma,[197-200] and the hexyl ester (Hexvix®) has shown promising properties for being used in fluorescent diagnosis of bladder cancer.[201-203]

Phytoporphyrin (phylloerythrin; Figure 1.5B) is a photoactive porphyrin derivative structurally related to protoporphyrin IX. Phytoporphyrin is formed in the microbial degradation of Chl in the gastro intestinal tract and was early detected in the blood of grazing animals with liver dysfunction in which phytoporphyrin was accumulated in tissues due to insufficient excretion.[204] These animals clearly suffered from severe photosensitization when exposed to strong sunlight.

1.3.3. Tookad

Tookad (WST09, Figure 1.5C), is a palladium containing BChl derivative in which the phytyl group ($C_{20}H_{39}$) at the propionyl residue has been replaced by a hydrogen atom, giving Pd-bacteriopheophorbide (Pd-BPheid). A common feature for all BChls is that the red-most absorption band is the strongest one, as opposed to a majority of photosensitizers that display only weak absorption in the red region and significantly stronger absorption in the visible region. The red-most absorption band of Tookad displays a high molar extinction coefficient and is significantly shifted towards the near-infrared region, at 763 nm.[205] PDT-treatment with Tookad thus reaches deeper into tissues compared with photosensitizers such as Photofrin (cf. red-most absorption at 630 nm).

Tookad-PDT has shown significant phototoxicity on several different carcinoma cells lines and tumours as a result of tumour vascular damage.[205-211] Phase I[212-214] and phase II[215] clinical trials performed on prostate cancer patients

have shown promising outcome. Tookad induces minimal side-effects, mainly due to very fast clearance rate from the body, which reduces accumulation in the skin tissue and thereby minimizes photosensitivity.[216] Tookad possesses several highly advantageous properties for being used in PDT.

1.3.4. Foscan

Foscan (*meso*-tetra-hydroxyphenylchlorin, *m*-THPC, temoporfin, Figure 1.5D) is a very potent photosensitizer that is highly hydrophobic due to the presence of four phenyl groups. These groups would possibly also contribute to a red-shift in the absorption wavelength, but they are positioned ~90 degrees out of plane from the chlorin macrocycle and thus do not significantly contribute to the conjugation. The red-most absorption maximum is subsequently not significantly shifted compared to unsubstituted chlorin, and is found around 650 nm.[217] However, the extinction coefficient for this absorption high, which provides a high efficiency of the drug and a strong response of the treatment is obtained with small doses and with low light intensity. If a similar response would be expected for Photofrin, drug doses and light intensities up to 100 times higher would be required.[218]

Foscan has proven to be effective in clinical trials of patients with oral, lip, and various other squamous cell carcinomas in the head and neck region and was approved for treatment of head and neck cancers in Europe in 2001.[219-221] Foscan has been found to specifically accumulate in brain tumours rather than in normal brain tissue, suggesting that Foscan-mediated PDT can be used in this type of treatment.[222] Despite several advantages of PDT-treatment with Foscan, a significant drawback is prolonged skin photosensitivity shown in many patients.

1.3.5. Chlorin e6 and chlorin p6

Chlorin e6 (Figure 1.5E) and chlorin p6 (Figure 1.5F) belong to a group of hydrophilic chlorin derivatives. Chlorin e6 and chlorin p6 differ only in that the

propenoic acid at position 15 (cf. numbering in Figure 1.4A) in chlorin e6 is replaced by a methanoic acid in chlorin p6. The carboxylic acid substituents make the compounds hydrophilic, but due to their presence on the same side of the macrocycle they also give the compounds amphiphilic character. Chlorin e6 and chlorin p6 show promising singlet oxygen yields in solution,[223, 224] and have been found to possess photocytotoxic properties.[225-227] These compounds also display suitable absorption properties for PDT, with the red-most absorption maximum in the 650-660 nm range.[228 229]

The potential of chlorin e6 and chlorin p6, as well as their alkyl esters, to be utilized in PDT has however not been as extensively explored as the mono-L-aspartyl chlorin e6 (NPe6, talaporfin sodium, Laserphyrin®) derivative. NPe6 is substituted with an aspartic acid at the propionic acid residue at position 17 (cf. numbering in Figure 4A) and due to an additional ionizable carboxylic group, this compound is more hydrophilic than the parent chlorin e6 compound, which is advantageous for administration in the blood. NPe6 displays the red-most absorption maximum in the same range as chlorin e6 and chlorin p6. Clinical trials with NPe6 have shown positive results for treatment of subcutaneous tumours and superficial lung cancer, and the compound has been approved for treatment of early stage lung cancer.[230, 231] NPe6 is associated with a rapid clearance from the blood stream, which causes minimal photosensitivity in the patients under treatment.[230, 231]

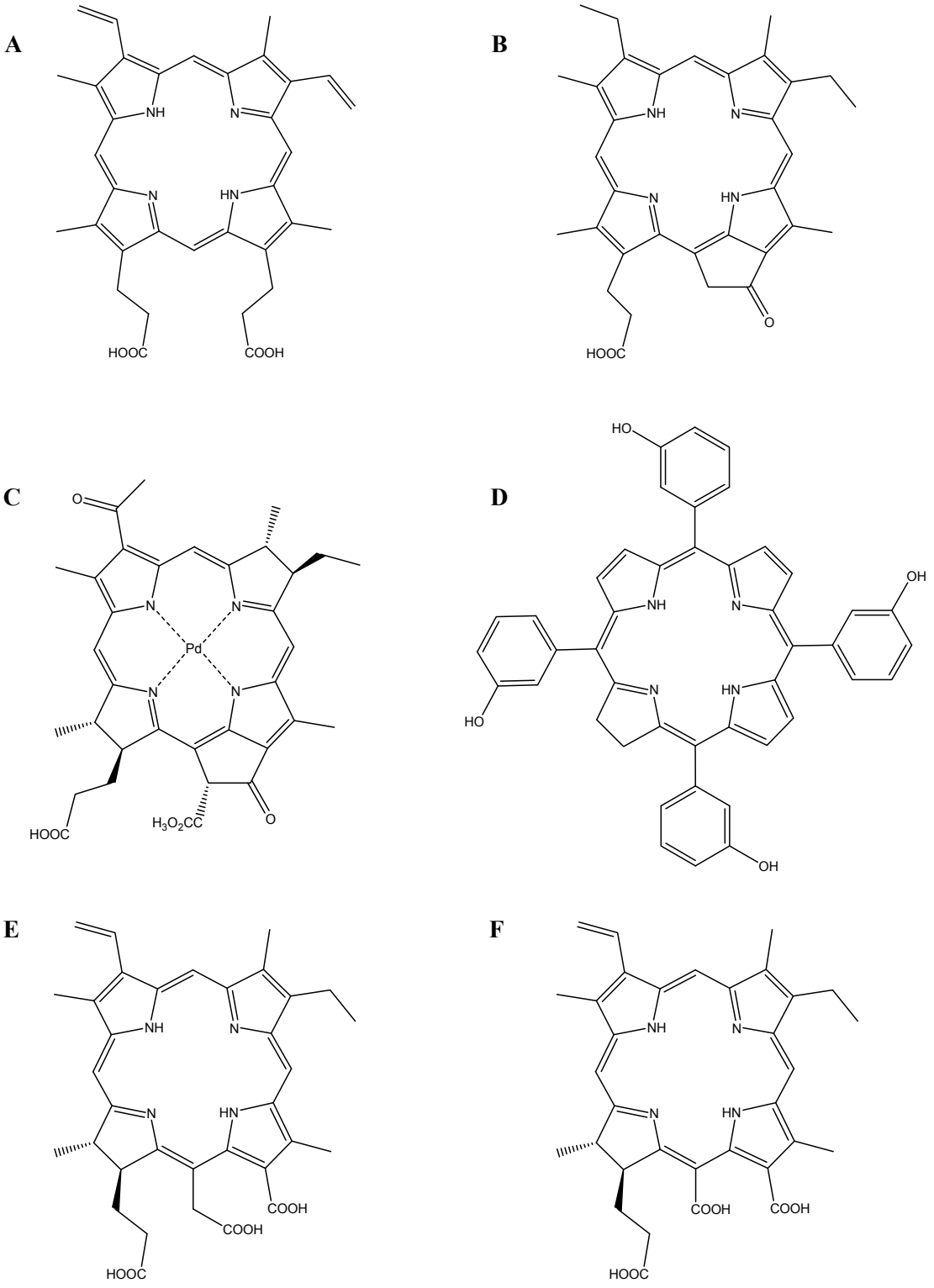

Figure 1.5. Schematic figures of (A) protoporphyrin IX, (B) phytoporphyrin, (C) Tookad, (D) Foscan, (E) chlorin e6, and (F) chlorin p6.

1.4. Aims and objectives

1.4.1. Paper I

The aim of the first study was to determine possible reactions that second generation hypericin derivatives substituted with bromine at different positions can undergo after light excitation. Redox reactions followed by debromination generate hypericin radicals, which can react with biological molecules or molecular oxygen.

1.4.2. Paper II and IV

MD simulations of hypericin and brominated derivatives in lipid membranes were performed in order to study their properties and permeability therein. This information is essential in order to determine the ability of drug molecules to penetrate plasma membranes. Effects of the level of bromination of hypericin and the presence of cholesterol in the membranes were studied.

1.4.3. Paper VII

Interactions between hypericin and the Ca^{2+} pump SERCA in the ER membrane were studied using homology modelling, docking and MD simulations in order to determine if the protein is a possible cellular target for hypericin. The binding modes of hypericin in various possible binding sites were studied, and the strengths of binding were compared to known SERCA inhibitors.

1.4.4. Paper III, V and VI

The performance of long-range corrected functionals used in TD-DFT to calculate absorption spectra of tetrapyrrole compounds for PDT was investigated in order to determine suitable methodologies for computational prediction of photosensitizers with suitable absorption properties. Furthermore, modified chlorin derivatives with strong absorption in the therapeutic window of PDT were designed.

CHAPTER 2. THEORETICAL BACKGROUND OF COMPUTATIONAL CHEMISTRY

Computational techniques have evolved as important tools in the field of chemistry, with applications such as predicting molecular structures, reaction mechanisms, and properties relating to biological activities. The most common models that computational methods are based on are quantum mechanics (QM) and molecular mechanics (MM). This chapter aims to give an overview of the methods and the theoretical principles which they are based on. A more comprehensive description can be found in standard text books,[232-235] which are used as basis for the summary below.

2.1. Quantum mechanics

In QM calculations, electrons are explicitly considered and this makes QM methods useful in calculating properties related to the electronic distribution, important for example when studying chemical reactions in which bonds are broken and formed. QM methods generate accurate results but due to time-consuming calculations their application is limited to relatively small systems that can be handled in a reasonable period of time.

2.1.1. The Schrödinger equation

The time-dependent Schrödinger equation describes how the quantum state of a system varies with time, and for a single particle with mass *m* it is written,

$$\left\{-\frac{\hbar^2}{2m}\nabla^2 + V\right\}\Psi(\boldsymbol{r},t) = i\hbar\frac{\partial\Psi(\boldsymbol{r},t)}{\partial t} \qquad (2.1)$$

where $\hbar$ is Planck's constant divided by 2π and i is the square root of -1. The position of the particle in space is given by the vector $\boldsymbol{r} = x\boldsymbol{i} + y\boldsymbol{j} + z\boldsymbol{k}$. V represents the external field in which the particle moves and Ψ is the wavefunction that describes the motion of the particle. ∇^2 is the Laplacian operator,

$$\nabla^2 = \frac{\partial^2}{\partial x^2} + \frac{\partial^2}{\partial y^2} + \frac{\partial^2}{\partial z^2} \tag{2.2}$$

When the external potential V is independent of time ($V(\mathbf{r})$) the wavefunction can be written as a product of a spatial part and a time part, $\Psi(\boldsymbol{r}, t) = \Psi(\boldsymbol{r}) f(t)$, which gives,

$$f(t)\left\{-\frac{\hbar^2}{2m}\nabla^2 + V\right\}\Psi(\boldsymbol{r}) = \Psi(\boldsymbol{r}) i\hbar \frac{\partial f(t)}{\partial t} \tag{2.3}$$

that after dividing both sides by $\Psi(\boldsymbol{r}) f(t)$ generates,

$$\frac{1}{\Psi(\boldsymbol{r})}\left\{-\frac{\hbar^2}{2m}\nabla^2 + V\right\}\Psi(\boldsymbol{r}) = \frac{i\hbar}{f(t)}\frac{\partial f(t)}{\partial t} \tag{2.4}$$

The left side is independent of t and the right side must therefore also be independent of t. In the same way, the right side is independent of $\boldsymbol{r}$ and subsequently the left side must also be independent of $\boldsymbol{r}$. It is clear that both sides can be set equal to the same constant, E. This gives rise to two differential equations,

$$\left\{-\frac{\hbar^2}{2m}\nabla^2 + V\right\}\Psi(\boldsymbol{r}) = E\Psi(\mathbf{r}) \tag{2.5}$$

and

$$\frac{1}{f(t)}\frac{\partial f(t)}{\partial t} = -\frac{iE}{\hbar} \tag{2.6}$$

The latter equation is solved to yield,

$$f(t) = e^{-iEt/\hbar} \tag{2.7}$$

and subsequently we obtain,

$$\Psi(\boldsymbol{r}, t) = \Psi(\boldsymbol{r}) e^{-iEt/\hbar} \tag{2.8}$$

that states that $\Psi(\boldsymbol{r})$ differs from $\Psi(\boldsymbol{r}, t)$ only by a phase factor of constant magnitude.

Equation 2.5 is the time-independent Schrödinger equation, which can be written,

$$\hat{H}\Psi(\boldsymbol{r}) = E\Psi(\boldsymbol{r}) \tag{2.9}$$

where $\hat{H}$ is the Hamiltonian operator,

$$\hat{H} = -\frac{\hbar^2}{2m}\nabla^2 + V \tag{2.10}$$

$\hat{H}$ operates on the wavefunction (the eigenfunction) and generates a value of the energy E (the eigenvalue) multiplied by the wavefunction. $\hat{H}$ contains kinetic and potential energy for all particles in the system.

The Schrödinger equation can only be exactly solved for systems containing at most one electron. For one-electron systems the Hamiltonian is written as a sum of the kinetic energy of the electron and the Coulombic interaction between the electron and the nucleus (containing Z protons) separated by the distance r,

$$\hat{H} = -\frac{\hbar^2}{2m}\nabla^2 - \frac{Ze^2}{4\pi\varepsilon_0 r} \tag{2.11}$$

Larger systems, containing more than one electron, cannot be exactly solved and the wavefunction can adopt several functional forms. The problematic issue of a system containing more than one electron is the correlation between the electrons, which arises due to their spin. In order to solve the Schrödinger equation for most chemical systems, several approximate methods are available.

2.1.2. Hartree-Fock (HF)

In order to study systems that contain more than one electron, approximations have to be applied. In the HF method a number of approximations are made.

The Born-Oppenheimer approximation was the first approximation used to solve the Schrödinger equation for a molecular system.[236] The approximation separates the motion of the nuclei from that of the electrons. This decoupling can be performed due to the fact that protons and neutrons are approximately 1,800 times heavier than the electrons. The movement of the electrons is thus much faster than the nuclear movement and the electrons can therefore adjust almost instantaneously to any movement of the nuclei. The nuclei are for that reason considered to be fixed, giving the nuclear kinetic energy term equal to zero and the potential between nuclei to be constant. The total wavefunction can then be written in the form of a nuclear part Ψ_N and an electronic part Ψ_e. The total energy of the system equals the sum of the nuclear and electronic energies and the Schrödinger equation is written,

$$\hat{H}^{B-O}\Psi_N\Psi_e = (E_N + E_e)\Psi_N\Psi_e \quad (2.12)$$

The Hamiltonian operator contains kinetic energy (*T*) of the electrons and potential energy (*V*) for all particles, nuclei (*N*) and electrons (*e*), in the system,

$$\hat{H}^{B-O} = \hat{T}_e + \hat{V}_{NN} + \hat{V}_{Ne} + \hat{V}_{ee} \quad (2.13)$$

In the case of molecules, it is desirable to find a way to determine which proposed wavefunction is the best one, since no exact one can be obtained. The variation theorem can be used to solve this problem. The variation theorem states that the energy calculated from an approximate wavefunction is always greater than the exact ground state energy. To improve the wavefunction, the energy is thus minimized.

The wavefunction can be written in a way that describes the electrons as independent of each other, with each electron in a different orbital. For a system with *N* electrons, one-electron spin orbitals, χ_1, χ_2, χ_3,…, χ_N, can be written. Each spin orbital is a product of a spatial function and a spin function. This is

the first assumption in the independent particle approximation that HF is based on. The total wavefunction for the system can then be written in the form of a Hartree product,

$$\Psi(1,2,\dots,N) = \chi_1(1)\chi_2(2)\dots\chi_N(N) \tag{2.14}$$

However, this way of writing the wavefunction does not satisfy the antisymmetry principle since the exchange of two electrons does not change the sign of the wavefunction. To satisfy the antisymmetry principle the wavefunction is written in the form of a determinant,

$$\Psi = \frac{1}{\sqrt{N!}}\begin{vmatrix} \chi_1(1) & \chi_2(1) & \cdots & \chi_N(1) \\ \chi_1(2) & \chi_2(2) & \cdots & \chi_N(2) \\ \vdots & \vdots & & \vdots \\ \chi_1(N) & \chi_2(N) & \cdots & \chi_N(N) \end{vmatrix} \tag{2.15}$$

This determinant is called a Slater determinant. If two rows in the determinant are exchanged, which would correspond to an exchange of two electrons, this leads to a change in sign of the determinant and the antisymmetry principle holds. If two rows are identical, this means that the two electrons are assigned to the same spin orbital and the determinant equals zero. This is explained by the Pauli principle, which states that two electrons cannot have both the same spatial and spin function. If the spatial functions are the same, meaning that the electrons occupy the same orbital, they need to have opposite spin.

When handling polyelectronic systems one has to account also for the presence of interactions between electrons. Apart from the core Hamiltonian operator ($\widehat{H}^{core}$) that only accounts for the kinetic energy of a single electron and the Coulombic attraction between the electron and the nuclei in a system with no interelectronic interactions, one has to add the Coulomb interaction between electrons (represented by the Coulomb operator ($\hat{J}_j(1)$) and the exchange integral ($\widehat{K}_j(1)$). The Fock operator $\hat{f}_i(1)$ includes all three operators, and is for a closed-shell system written,

$$\hat{f}_i(1) = \hat{H}^{core}(1) + \sum_{j=1}^{N/2} \{2\hat{J}_j(1) - \hat{K}_j(1)\} \quad (2.16)$$

The Fock operator acts on the spin orbital χ_i and generates the energy ε_i,

$$\hat{f}_i \chi_i = \varepsilon_i \chi_i \quad (2.17)$$

A common way to express molecular spin orbitals is to write them in the form of a linear combination of atomic orbitals (LCAO), one-electron orbitals (ϕ_μ) that are commonly called basis functions,

$$\psi_i = \sum_{\mu=1}^{K} c_{\mu i} \phi_\mu \quad (2.18)$$

In HF, initially a set of trial spin orbitals are obtained. The orbitals are used to construct the Fock operator, which upon acting on the orbitals generates a new set of orbitals, which are used in a following iteration. This procedure is called self-consistent field (SCF) and refines the energy in each iteration. The procedure is repeated until the difference in energy from one iteration to another is zero or below a certain threshold; the system has reached self-consistence.

The HF approach belongs to the group of *ab initio* (Latin for "from the beginning") QM methods, which means that the calculations are performed starting with no empirical or semi-empirical parameters as input, but derives all input from physical principles.

2.1.3. Basis sets

The atomic orbitals in a system are described by combinations of functions. These mathematical descriptions are called basis sets. An infinite number of functions represent a complete basis set. However, this is not possible to include in calculations. Finite basis sets include approximations that make calculations possible, and the number and type of functions used influence the

accuracy. The balance between accuracy and computational effort thus has to be considered.

The basis functions used are usually Slater type orbitals (STO)[237] or Gaussian type orbitals (GTO).[238] STOs have the following functional form,

$$\chi_{\zeta,n,l,m}(r,\theta,\varphi) = NY_{l,m}(\theta,\varphi)r^{n-1}e^{-\zeta r} \tag{2.19}$$

where N is a normalization constant, $Y_{l,m}$ are spherical harmonic functions, r is the radius, ζ is the orbital exponent, and n, l and m are quantum numbers. STOs are mainly used for small systems such as atoms and diatomic molecules when high accuracy is required.

GTOs can be written in Cartesian coordinates and have the following functional form,

$$\chi_{\zeta,l_x,l_y,l_z}(x,y,z) = Nx^{l_x}y^{l_y}z^{l_z}e^{-\zeta r^2} \tag{2.20}$$

where the sum of l_x, l_y and l_z determine the orbital type. GTOs are less accurate than STOs due to the r^2 dependence which makes it hard to correctly describe the function close to the nucleus and in the tail part. In general terms, three GTOs are required to achieve accuracy comparable to one STO. However, GTOs are easily integrated and this compensates for the increased number of functions required. Atomic orbitals are therefore generally represented as linear combinations of Gaussian functions.

A minimal basis set contains only the number of functions that are needed to describe all occupied orbitals in each atom. STO-3G is the simplest minimal basis set used in *ab initio* calculations. This basis set is a STO represented as a linear combination of three Gaussian functions. The minimal basis sets are usually not enough to correctly describe chemical systems and additional functions are therefore included. An extra basis function can be added to each atomic orbital, forming a double zeta (DZ) basis set that contains twice the number of basis functions as the minimal basis set. In the same way, three and four times the number of functions as the minimum basis forms triple and quadruple zeta basis sets. It is common to increase the number of functions for

the valence orbitals only, leaving the core orbitals unaffected. These basis sets go under the name split valence basis sets. As an example, the 6-31G basis set uses a minimal basis for the core orbitals, a linear combination (contraction) of six primitive GTOs, whereas each valence orbital is described by two contractions, one with three primitive GTOs and one with only one GTO. Triple split valence basis sets, such as 6-311G, in which the valence is split into three contractions, are also commonly applied.

Additional higher angular momentum functions for the valence electrons can improve the description, as these electrons are important participants in the chemistry of an atom. These functions are named polarization functions and are added to account for the altered charge distribution of an atom in a molecule. This allows the orbitals to change shape, as opposed to the split valence basis sets that only allow a change in size of the orbitals. p-orbitals are added to polarize s-orbitals of hydrogen, whereas d-orbitals are added to polarize p-orbitals. In order to extend the 6-31G basis set used in the example above, the 6-31G(d) basis set includes d-orbitals for heavy atoms, and the extended version 6-31G(d,p) includes d-orbitals for heavy atoms and additional p-orbitals for hydrogen. Another denotation for 6-31G(d) is 6-31G*, and 6-31G(d,p) can be written as 6-31G**. Multiple polarization functions can be added to increase the accuracy. 6-31G(2d) is an example of a basis set in which two d functions are added to each heavy atom. Highly accurate basis sets add both d and f functions to heavy atoms and p and d functions to hydrogens.

In order to correctly describe systems in which the electrons are located far away from the nucleus (anions, systems with lone pairs, excited states) it is often important to include diffuse functions, which are normally large s- and p-type functions. These functions allow for the orbital to occupy a larger region of space and thereby account for the electron density at large distances from the nucleus, where the amplitude of the Gaussian functions is low. The 6-31+G(d) basis set includes diffuse functions on heavy atoms, and the 6-31++G(d) basis set includes diffuse functions also on hydrogen.

Atoms larger than the third row elements are usually treated differently from smaller atoms, using combined basis sets. For these atoms, the core electrons are commonly treated with effective core potentials (ECPs) and the valence electrons with an appropriate valence basis set. LANL2DZ is one of the most widely used basis sets for large atoms.[239-241]

2.1.4. Density functional theory (DFT)

Instead of calculating the complicated *N*-electron wavefunction like in HF theory, it is possible to use single-electron wavefunctions to calculate the total electronic energy and the overall electronic density distribution. For an *N* electron system only three spatial variables are used in DFT compared to 4*N* variables (3*N* spatial and one spin) in HF. The electron density, ρ, is the fundamental quantity in DFT, based on the paper by Hohenberg and Kohn in 1964 that showed that the ground state energy and other properties of a system are defined by the electron density.[242] This means that the energy of a system can be defined as a functional of the electron density, E[ρ(**r**)]; that is, the energy (E) is a function of the electron density (ρ) which in turn is a function of the positions (**r**). The minimum energy corresponds to the exact ground state electron density, and according to the variational principle any incorrect electron density generates an energy value above the exact energy.

The energy of a system is defined as a sum of electronic density functionals,

$$E[\rho] = T[\rho] + E_{Ne}[\rho] + J[\rho] + E_{XC}[\rho] \qquad (2.21)$$

As it is hard to obtain the density of an interacting system, the common approach is to use a fictitious system of non-interacting electrons, called the Kohn-Sham system.[243] This system is created such that it has exactly the same density as the real system with interacting particles. $T[\rho]$ is thus the kinetic energy of non-interacting electrons. $E_{Ne}[\rho]$ is the attraction between the nuclei and the electrons and $J[\rho]$ is the Coulombic electron-electron repulsion energy. $E_{xc}[\rho]$ is the exchange-correlation energy that is added to account for the remaining interactions between the electrons; that is the kinetic energy of

interacting electrons and a non-classical electron-electron repulsion term that contains exchange and correlation.

Based on the introduction of a reference system of non-interacting electrons, the electron density can be written as a sum of the square of a set of one-electron orbitals (Kohn-Sham orbitals),[243]

$$\rho(\boldsymbol{r}) = \sum_{i=1}^{N} |\psi_i(\boldsymbol{r})|^2 \tag{2.22}$$

By using this expression for the electron density and applying the variational theorem to the electronic energy, the one-electron Kohn-Sham equations can be written as,

$$\left\{-\frac{\nabla_1^2}{2} - \left(\sum_{A=1}^{M} \frac{Z_A}{r_{1A}}\right) + \int \frac{\rho(\boldsymbol{r}_2)}{r_{12}} d\boldsymbol{r}_2 + V_{XC}[\boldsymbol{r}_1]\right\}\psi_i(\boldsymbol{r}_1) = \varepsilon_i \psi_i(\boldsymbol{r}_1) \tag{2.23}$$

where V_{XC} is the exchange-correlation functional and ε_i is the Kohn-Sham orbital energy. The Kohn-Sham equations for the non-interacting particles can be easily solved using a wavefunction represented as a Slater determinant of single-particle orbitals (Kohn-Sham orbitals).

The Kohn-Sham equations are solved in an iterative procedure starting with introducing an initial guess of the electron density into the Kohn-Sham equations, generating a set of orbitals that are used to calculate a new electron density. The new electron density is used as input to the second iteration and the procedure is repeated until convergence has been achieved. At this stage the total energy of the system is calculated.

The challenge in DFT is to find a way to describe the exchange-correlation term as correctly as possible. The accuracy of the method thus depends on the approximations used. A common approach is to initially divide the exchange-correlation functional into an exchange part and a correlation part, represented by an exchange functional and a correlation functional,

$$E^{XC}[\rho(\boldsymbol{r})] = E^{X}[\rho(\boldsymbol{r})] + E^{C}[\rho(\boldsymbol{r})] \tag{2.24}$$

The exchange and correlation terms are associated with the exchange-correlation hole that arises from the reduced probability to find two electrons close to each other due to their charge and spin. The exchange part is called the Fermi hole and corresponds to exchange between electrons of the same spin, whereas the correlation part is called the Coulomb hole. DFT methods contain one exchange functional and one correlation functional. There are several approaches available on how to approximate the two functionals.

The local density approximation (LDA) is based on a uniform electron gas model that considers the electron density to be constant throughout all space. In LDA the electron density in a volume element takes a constant value equal to the real electron density in a specific point within the volume element. Problems with LDA arise in regions close to the van der Waals radii where the electron density varies significantly over a short distance. To overcome this problem one can use infinitesimal volume elements or consider a non-uniform electron gas model, like in the generalized gradient approximation (GGA). In GGA the gradient of the density in each point in space is considered in addition to the absolute density value.

DFT methods are combinations of different exchange and correlation functionals. An example of a pure DFT method is BLYP that includes Becke's gradient-corrected exchange functional (B)[244] and the gradient-corrected correlation functional by Lee, Yang and Parr (LYP).[245]

2.1.4.1. Hybrid methods

The most widely used DFT methods today contain hybrid density functionals, in which a part of HF exchange energy is added to the exchange-correlation energy derived from a DFT approximation,

$$E_{hybrid}^{XC} = c_{HF}E_{HF}^{X} + c_{DFT}E_{DFT}^{XC} \quad (2.25)$$

where the *c*'s are parameters that determine the weight of each functional. The parameters are determined by fitting the predicted values to experimental

thermochemical data, such as atomization energies, ionization potentials, and proton affinities.

B3LYP (Becke three-parameter (exchange), Lee, Yang and Parr (correlation))[246] is one of the most successful hybrid methods and has been extensively used. The HF exchange in B3LYP amounts to 20%. B3LYP is considered to be an accurate DFT method that generates small errors in geometries[247] and energies.[248, 249]

Hybrid DFT functionals included in the studies reported herein, apart from B3LYP, include PBE0[250] and M06 functionals.[251-253] PBE0 (also known in the literature as PBE1PBE) is a hybrid with 25 % HF exchange based on the Perdew, Burke and Ernzerhof (PBE) functional.[254, 255] M06HF includes full HF exchange and thus possesses promising long-range properties.[251, 252] M06 and M062X are extensions of M06HF.[253]

Range-separated functionals include an increasing fraction of HF exchange as the interelectronic distance increases, in order to generate a more correct asymptotical behaviour. These functionals are expected to be useful in the context of excited state calculations as the non-Coulomb part of the exchange functional is not accurate at large distances. The exchange energy is split into a long-range part and a short-range part. The long-range part includes HF exchange and the short-range part includes DFT exchange. The exchange-correlation energy can be written,

$$E_{LC-DFT}^{XC} = E_{LR-HF}^{X} + E_{SR-DFT}^{X} + E_{DFT}^{C} \tag{2.26}$$

A parameter, ω, is introduced to control the range of the interelectronic separation.

Long-range corrected hybrid DFT functionals that were included in the studies presented herein include CAM-B3LYP,[256] LC-ωPBE,[257-260] and the ωB97 functional family.[261, 262] In CAM-B3LYP a Coulomb attenuating method is used to include long-range correction on B3LYP. LC-ωPBE is a long-range corrected version of PBE. Three functionals belong to the ωB97 family; ωB97,[261] ωB97X,[261] and ωB97XD.[262] ωB97 and ωB97X differ in the presence

of a small fraction of short-range HF exchange (the 'X' in ωB97X), an additional term that can be added in Equation 2.26. ωB97XD is an extension of ωB97X and contains empirical dispersion correction. CAM-B3LYP also contains a fraction of short-range HF exchange, whereas LC-ωPBE does not.

2.1.5. Time-dependent density functional theory (TD-DFT)

TD-DFT is applied in order to treat excitations and other time-dependent situations. This technique is related to time-dependent quantum mechanics, but as it is based on the one-body electron density, $\rho(\mathbf{r}, t)$, it has the advantage that it depends only on the three variables x, y and z. In TD-DFT, the time-dependent Kohn-Sham equations are utilized,[263, 264]

$$\left\{-\frac{\nabla_1^2}{2} - \left(\sum_{A=1}^{M} \frac{Z_A}{r_{1A}}\right) + \int \frac{\rho(\boldsymbol{r}_2, t)}{r_{12}} d\boldsymbol{r}_2 + V_{XC}[\boldsymbol{r}_1, t]\right\}\psi_i(\boldsymbol{r}_1, t) = \varepsilon_i \psi_i(\boldsymbol{r}_1, t) \tag{2.27}$$

and the density of the interacting system is calculated from the time-dependent Kohn-Sham orbitals of non-interacting electrons,

$$\rho(\boldsymbol{r}, t) = \sum_{i=1}^{N} |\psi_i(\boldsymbol{r}, t)|^2 \tag{2.28}$$

The exchange-correlation energy has to be approximated like in stationary-state DFT. However, approximations for time-dependent exchange-correlation functionals have not been as widely developed as time-independent approximations. The simplest and most widely used approximation is the adiabatic local density approximation, which resembles the LDA.

TD-DFT is one of the most commonly used methods to calculate excitation energies and has been found accurate in a large number of studies (Section 2.1.5.1). Absorption spectra can be calculated using two different procedures. The first one involves propagation of the time-dependent Kohn-Sham equations and the Kohn-Sham orbitals during time. The initial ground state with an

exchange-correlation potential such as LDA is propagated with a time-dependent exchange-correlation potential such as the adiabatic local density approximation.

The second procedure that is used to calculate absorption spectra involves linear-response theory. A perturbation in the form of an external potential added to the ground state nuclear potential induces a change in density of the system and the density can be written,

$$\rho(\boldsymbol{r},t) = \rho^{(0)}(\boldsymbol{r}) + \rho^{(1)}(\boldsymbol{r},t) + \rho^{(2)}(\boldsymbol{r},t) + \cdots \quad (2.29)$$

where $\rho^{(1)}$ is the density that depends linearly on the perturbation potential, $\rho^{(2)}$ depends quadratically on the perturbation, and so forth. In the case of a weak perturbation the only term to consider is the linear one. The density-density response function has poles that correspond to the excitation energies of the interacting system, and this function can be calculated with TD-DFT using a system of non-interacting electrons.[263]

2.1.5.1. Performance of functionals in TD-DFT excited state calculations

TD-DFT offers a significantly less computer-demanding approach to calculate excitations compared to correlated *ab initio* methods, and can thus be used to study large systems within a reasonable time frame. Despite the fact that TD-DFT lacks multireference treatment it has been found that the method can be used to accurately predict absorption spectra in many studies. The specific performance of TD-DFT, however, depends on the density functional used. The performance of correlated *ab initio* methods, on the other hand, strongly depends on the specific method used and the size of the active space. A large active space is often required in order to achieve high accuracy with these methods, hence making the study of large compounds a computer-demanding task. Combinations of DFT with single-excitation configuration interaction (CIS) and multireference configuration interaction (MRCI) have been more successful than pure *ab initio* methods in the prediction of absorption spectra of, as an example, porphyrin and chlorin.[265, 266]

Several benchmarking studies have been performed with the aim to evaluate the performance of various functionals used in TD-DFT in predicting absorption spectra, of which some are presented below. It is clear that the performance of the functionals in many cases is system dependent and when the studies are performed on large sets of compounds with different chemical structures, the results are often hard to interpret.

Perpète et al. studied the absorption maximum of 66 substituted anthraquinone dyes using B3LYP and PBE0 and found that PBE0 was more accurate than B3LYP, with a mean absolute error of 0.05 eV after a fitting procedure.[267] Charge-transfer and $\pi \rightarrow \pi^*$ transitions of a set of push-pull (donor-acceptor) chromophores was studied using several different functionals, but the results were hard to interpret due to a large spread in the data.[268] The performance for charge transfer and $\pi \rightarrow \pi^*$ transitions were not always in agreement. The value of the attenuation parameter (range-separation parameter) for the long-range corrected functionals was also an issue that could affect the results. PBE0 was however among the functionals that overall generated the most accurate results.

Jacquemin et al. performed a benchmarking study of 115 dyes using six pure and hybrid methods, including long-range corrected functionals such as LC-ωPBE and CAM-B3LYP, and found that PBE0 generated overall smallest errors.[269] Jacquemin et al. also performed a more extensive benchmarking study of singlet excitations of ~500 organic compounds with varying size using 29 functionals.[270] The performance of the functionals was clearly system dependent, but 'standard' hybrid type functionals such as PBE0, X3LYP, and B98 performed overall best, whereas hybrid functionals with a larger fraction of exact exchange tend to underestimate the transition energies.

The long-range corrected functionals in the ωB97 family were recently subject to a benchmarking study that showed that ωB97XD generated smallest errors within this family, in the same range as CAM-B3LYP.[271] ωB97 generated the largest errors, similar to LC-ωPBE. The ωB97 functionals were not able to perform better than B3LYP in calculations of singlet transitions.

However, all three ωB97 functionals were found to outperform B3LYP in calculations of triplet transitions. Also for triplet states ωB97XD was found to perform better than the two other ωB97 functionals.

Singlet-triplet transitions of 20 small- and medium-sized molecules were subject to a benchmarking study using 34 functionals.[272] The functionals showed mean absolute errors of 0.2-0.7 eV, and for many functionals the errors were larger than for singlet-singlet transitions. BMK and M06-2X showed overall good performance, whereas PBE0 and CAM-B3LYP generated larger errors.

In order to allow fast prediction of absorption properties, with applications for example in computational drug design, it is desirable to develop and evaluate TD-DFT approaches that can be applied with highly accurate outcome.

2.2. Molecular mechanics

2.2.1. Principles of molecular mechanics

In studies of large systems, such as DNA, proteins and membranes, it is a less straight-forward approach to apply QM methods due to the large number of electrons involved. In order to treat this type of system, MM is among the most commonly used approaches. In MM the electronic motions are ignored, which is possible due to the Born-Oppenheimer approximation that allows separation of the nuclear and electronic motions. The atoms are treated as hard spheres that are held together by means of potential functions, generating "classical" atoms. As no electrons are considered in MM, it is not possible to calculate properties that depend on the electronic distribution.

The potential energy of a system, $V(\boldsymbol{r})$, is written as a function of the nuclear positions, $\boldsymbol{r}$, of N particles. The potential energy expression in general includes functions that describe how bonds are stretched, angles are bent and bonds are rotated, as well as functions that describe interactions between non-bonded atoms. Potential functions are used to calculate the energy of each contribution and the sum of the energies constitutes the total potential energy of the system. The potential energy of a system with N particles can be written,

$$V(\boldsymbol{r}) = \sum_{bonds} \frac{k_b}{2}\left(l_i - l_{i,0}\right)^2 + \sum_{angles} \frac{k_\theta}{2}\left(\theta_i - \theta_{i,0}\right)^2 + \sum_{torsions} \frac{V_n}{2}[1 + \cos(n\omega - \gamma)]$$
$$+ \sum_{i=1}^{N} \sum_{j=i+1}^{N} \left(4\varepsilon_{ij} \left[\left(\frac{\sigma_{ij}}{r_{ij}}\right)^{12} - \left(\frac{\sigma_{ij}}{r_{ij}}\right)^{6} \right] + \frac{q_i q_j}{4\pi\varepsilon_0 r_{ij}} \right) \qquad (2.30)$$

where the terms correspond to bond stretching, angle bending, bond rotation (torsion), and non-bonded interactions, respectively.

Bond stretching is in this expression modelled by a harmonic function about the reference bond length $l_{i,0}$. The reference bond length represents the bond length when all other terms in the force field are set to zero. When the system is far away from equilibrium an anharmonic Morse potential can be more appropriate to use. Angle bending is also represented by a harmonic function

about the reference bond angle $\theta_{i,0}$. The function is defined for all combinations of three bonded atoms. k_b and k_θ are force constants. The torsional function describes the dihedral angle between four bonded atoms and is calculated using cosine functions. In the torsion expression above, V_n refers to the barrier height, n is the number of minima in the function when the bond is rotated 360°, ω is the torsion angle, and γ is the phase factor that determines where the minima are located.

The non-bonded interactions are divided into van der Waals interactions and electrostatic interactions and sums over all pairs of particles. The most common approach to describe the van der Waals interactions is by using the Lennard-Jones 12-6 potential. This interaction involves repulsive forces (that vary as $1/r^{12}$), acting at short distances, and attractive forces (that vary as $1/r^6$), acting when the distance between the atoms is longer. The repulsive forces are due to the Pauli exclusion principle that states that any two electrons in a system cannot have the same set of quantum numbers. As the repulsive forces arise from interaction between electrons with the same spin, they are also referred to as exchange forces. The repulsive contribution to the total energy is always positive. The attractive, or dispersive, forces are due to changes in dipole moments as the electron clouds fluctuate. A transient dipole in a molecule can induce transient dipoles in neighbouring atoms and generate attractive forces between them. The dispersive energy is always negative. The Lennard-Jones 12-6 potential contains two parameters; ε that is the depth of the potential well and σ that is the collision diameter, the inter-particle distance at which the energy is zero.

The electrostatic interactions are usually calculated as a sum of interactions between pairs of point charges q, by using Coulomb's law. The correct charge distribution in a molecule is described by a multipole expansion, a sum of all point multipoles; charge, dipole, quadrupole, octupole, and so forth. The energy of two interacting charge distributions is a series of terms with combinations of interactions between different multipoles. A common and accurate way to do the summation of electrostatic interaction energies is to use the Ewald

summation method, which splits the sum in two, one in real space and one in reciprocal space. This summation results in faster convergence. The Ewald sum method is commonly applied to periodic systems. An extension of the Ewald summation is the particle mesh Ewald (PME) summation.[273, 274]

Additional terms can be added to the expression of the potential energy. Out-of-plane bending terms, of which improper torsions are most commonly used, are added in order to ensure that a planar geometry is maintained. Cross terms can be included to couple the separate terms in the potential energy expression. As an example, bond stretching can be coupled to angle bending to account for the increase in bond lengths as the bond angle between the atoms is decreased, in order to reduce the interactions between the two outermost atoms.

All information needed for a MM calculation is present in the force field, in the form of potential functions, parameters, and atom types. Atom types describe not only the atom number but also specify the hybridization state and the local environment. The parameters are obtained either from experiments or QM calculations. Different force fields include different functional forms of the potential functions, and different parameters and atom types; these differences make the force fields suitable for different types of systems.

2.2.2. Molecular dynamics

Molecular dynamics (MD) is a technique used to simulate movements of particles according to how their positions and velocities vary with time, based on Newton's laws of motion. As this is a time-consuming technique, MD is usually carried out using MM. Newton's second law states that a body with mass m, on which a force F is acting, experiences an acceleration a in the same direction as the force, according to $F = ma$. The trajectory of an MD simulation is obtained by solving the differential equations in Newton's second law.

In each step of the simulation, the total force acting on each particle is calculated from the derivative of the potential energy obtained from Equation 2.30. The force is used to calculate the acceleration of the particles according to,

$$\frac{d^2x_i}{dt^2} = \frac{F_{x_i}}{m_i} \tag{2.31}$$

The acceleration is used, together with the positions and velocities, to calculate the positions and velocities in the next step of the simulation.

Several algorithms for integration of the equations of motion exist, all which apply Taylor series expansions as approximations of the positions, velocities and accelerations. The Verlet algorithm is one of the most widely used algorithms.[275] In the Verlet algorithm the positions and accelerations at time t are used together with the positions in the previous step t-δt to calculate the positions in the new step t+ δt. One of the drawbacks with the Verlet algorithm is that the velocities have to be calculated explicitly. An extension of this algorithm is the velocity Verlet algorithm, in which positions, velocities and accelerations are calculated at the same time.[276] The Leap-frog algorithm is an alternative approach to calculate the next step.[277] This algorithm calculates velocities at time t+(δt/2) using the velocities at time t-(δt/2) and the acceleration at time t. The velocities at time t+(δt/2) are then used together with the positions at time t to calculate the positions at time t+δt. The name Leap-frog thus comes from that the velocities leap over the positions as they are calculated at t+(δt/2), whereas the positions are calculated at time t.

The length of the time step, δt, used in a simulation is required to be significantly less than the period of the fastest motion in the system, such as vibrations of bonds. The time step is usually set to be on the order of femtoseconds (fs).

Thermodynamic properties, such as temperature and pressure, are calculated from microscopic information by means of statistical mechanics. The MD program controls the properties by modifying the algorithms. A common strategy in MD simulations is to allow either the volume or the pressure to fluctuate, while keeping the other properties constant. The constant NPT and the constant NVT ensembles are the most commonly applied ensembles.

2.2.3. Molecular docking

Molecular docking is a widely utilized method used to predict the binding orientation of a molecule with respect to another molecule. Docking is often used in drug design to model binding of potential drug molecules to a target protein. Docking is performed either to study a specific ligand binding to a protein or to search a database for potential molecules that can bind to a protein. The increasing number of protein structures available in the Protein Data Bank (PDB) enables studies of a larger number of proteins with respect to their potential as drug targets.

Docking can be divided into two tasks; initial posing of a ligand in an active site, followed by scoring of the poses in order to assess the strength of the binding. A large number of docking algorithms for posing a ligand in an active site exist. Early docking algorithms considered both the ligand and protein as rigid bodies, hence only taking into account the six translational and rotational degrees of freedom.[278] More reliable methods however involve flexible docking. The protein active site is often not considered to undergo any significant conformational changes upon binding of a ligand. The receptor is thus kept rigid and only conformational degrees of freedom of the ligand are considered. Flexible docking algorithms can be used with today's computers to search databases for possible ligands to a target protein. However, highly accurate algorithms can only be used in docking of a small number of ligands. Docking algorithms that allow both the receptor and the ligand to move are extremely time-consuming and have not been extensively developed.[279]

The docked poses are ranked using scoring functions that approximate the binding free energy of a ligand to a receptor. The scoring functions are required to be calculated rapidly during the docking run and are expressed as a sum of separate terms that describe the various contributions to binding. A large number of scoring functions are available, and differ in which terms that are included in the expression of the binding free energy. Terms expressing non-bonded interactions and solvation effects are commonly used in scoring

functions. In order to speed up calculations, the scoring functions can be parameterized against empirical data.

Promising poses generated by an initial placement algorithm can be further refined with for example energy minimization, followed by re-scoring.

2.2.4. Homology modelling

Homology modelling has become a useful tool in predicting structures of proteins for which NMR and X-ray models are not available. Homology modelling is not a pure QM or MM based method, but rather a separate method. However, homology modelling is commonly performed in molecular modelling programs in which force field methods are used in the optimization steps in the construction of the protein model; hence the method is included in the MM section.

Homology modelling is based on two fundamental observations. First, the amino acid sequence determines the structure of a protein, indicating that, at least in theory, all that is needed to predict a protein structure is the amino acid sequence.[280] Secondly, it has been found that during evolution the structure of a protein is more conserved than the sequence.[281, 282] This suggests that the structure of two proteins with low sequence identity still can fold similarly. By analysing proteins in the PDB, Rost was able to obtain a limit for the number of aligned residues and the percentage of identical residues that offers a "safe" zone for homology modelling.[283] With a small number of aligned residues a high percentage of identical residues is needed in order to expect the two proteins to exhibit similar structure. The larger the number of aligned residues is the lower is the percentage of identical residues needed in order to expect two proteins to share high structural similarities. The graph levels out with a large number of aligned residues, giving a near constant percentage of identical residues of about 20 %. This limit allows for a large number of proteins of unknown structure to be modelled, using sequences of proteins with similar structure as templates.

During the homology modelling procedure, the amino acid sequence of a protein with unknown structure, the target, is first aligned with a template sequence. A template protein is usually found through sequence alignment with proteins in the PDB using algorithms such as BLAST (Basic Local Alignment Search Tool)[284] or FASTA (FAST-AII),[285] followed by alignment corrections. Secondly, the structure of the target protein is built by first copying the coordinates of the template structure that was used in the alignment. For residues that differ between the two proteins, only the backbone coordinates are copied, whereas if the aligned residues are the same and the sequence identity is high, also the conformations of the side-chains (rotamers) are copied directly from the template. Side-chains that are not identical in the alignment are modelled using rotamer libraries and scored using energy functions. The next step in most cases is loop modelling, which is necessary if there are gaps in the target or template sequence. The created homology model is optimized, usually applying force field methods, and finally validated.[286]

CHAPTER 3. REDOX AND DEBROMINATION REACTIONS OF BROMINATED HYPERICIN (PAPER I)

Brominated hypericin derivatives have been suggested to constitute promising second-generation photosensitizers as heavy-atom substitution enhances intersystem crossing between the singlet and triplet state and thereby increases the quantum yield of ROS production.[180, 183] Possible redox and debromination reactions of brominated hypericin were studied in order to determine how these derivatives act as photosensitizers. Four monobrominated hypericin derivatives were studied, named **1**, **2**, **3**, and **4**, respectively, according to the position of the bromine (cf. Figure 1.2).

3.1. Computational methodology

Geometry optimizations of the neutral ground state of the monobrominated hypericins, their corresponding radical anions (generated by addition of an electron) and *bay* deprotonated anions, as well as the corresponding debrominated species, were performed in the Gaussian 03[287] program using the B3LYP functional.[246] Geometry optimizations were performed in vacuum (dielectric constant $\varepsilon = 1$) using the 6-31G(d,p) basis set, followed by single-point calculations in vacuum, water ($\varepsilon = 78.38$), and nonpolar medium ($\varepsilon = 4.34$; representing lipid environment) using the 6-311+G(d,p) basis set. The calculations in bulk solvation were carried out using the integral equation formalism of the polarizable continuum model (IEF-PCM).[288, 289] Frequency calculations were performed at the lower level of theory. Zero-point vibrational energies and the thermal correction to Gibbs free energy were added to the single point energies in vacuum and solvent, respectively.

Debromination was studied by increasing the C-Br bond length in 15 steps of 0.1 Å. All other geometrical parameters were re-optimized in each step. The scannings were performed in vacuum at the B3LYP/6-31G(d,p) level of theory, followed by single point calculations in water and nonpolar media at the same level. Full transition state optimizations and frequency calculations were

performed on possible transition states at the B3LYP/6-31G(d,p) level of theory, followed by single point calculations at the B3LYP/6-311+G(d,p) level of theory in solution.

3.2. Results and discussion

During the geometry optimizations of the brominated hypericin molecules, as well as unsubstituted hypericin, two closely located energy minima were found, corresponding to two torsional conformers; "propeller" and "double butterfly" (Figure 3.1). The two conformers differ by about 2 kcal/mol, for both unsubstituted and substituted hypericin, and the propeller conformer was found to be overall more stable than the double butterfly conformer. The two conformations of hypericin have previously been found in molecular mechanics MM2 calculations.[290, 291] An asterisk denotes the double butterfly conformer in the data presented herein.

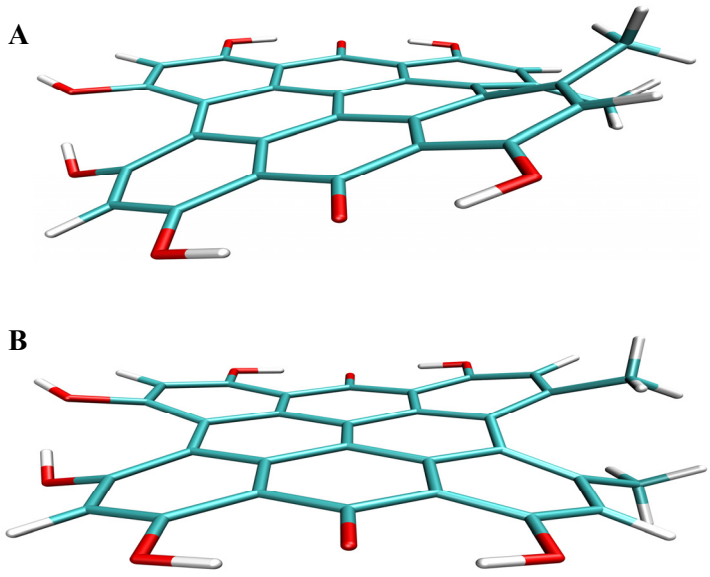

Figure 3.1. The two conformers of the hypericin molecule; (A) propeller and (B) double butterfly. Reproduced by permission of John Wiley & Sons. http://onlinelibrary.wiley.com/doi/10.1002/qua.21689/full

Adiabatic electron affinities (AEA; Table 3.1) were defined as the energy difference between the geometry optimized neutral molecules and the corresponding radical anions, and give a measure of the ability to extract an electron from the surrounding. Reduction was found to be spontaneous for all molecules, with an energy gain of about 3.7 eV in aqueous solution. The difference in AEA between the two conformers is small (less than 0.5 kcal/mol). However, the propeller compounds display overall slightly higher ability to extract an electron from the surroundings. The different positions of the bromine have a minor or negligible effect on the AEAs. A general trend observed is that the AEA increases with more polar medium, due to increased stabilization of charged species.

Table 3.1. Adiabatic electron affinities (eV) in different media.[a]

Bromin. site	*Vacuum*	*Lipid*	*Water*
1	2.53	3.48	3.74
2	2.53	3.48	3.74
3	2.53	3.47	3.74
4	2.53	3.46	3.73
1*	2.52	3.46	3.73
2*	2.52	3.46	3.73
3*	2.53	3.46	3.73
4*	2.52	3.45	3.72

[a] ZPE corrected energies (vacuum) and Gibbs free energies (solvent). Optimized structures, ZPE, and ΔG corrections: B3LYP/6-31G(d,p); Electronic and solvation energies: B3LYP/6-311+G(d,p).

As the AEA of oxygen in solution (3.9 eV)[292] is higher than the AEAs of the brominated hypericins in aqueous solution (~3.7 eV), it can be expected that, once the hypericin molecules are reduced, electron transfer to molecular oxygen most likely occurs with an energy gain, generating reactive superoxide radical anions. Superoxide can further react to form hydrogen peroxide and hydroxyl radicals. The electron affinity has been found to increase with increased number

of halogen substituents,[185] and the data for monobrominated hypericin indicates that the AEA increases by 0.22-0.24 eV when one bromine atom is added to unsubstituted hypericin.[58] The electron affinity of the triplet state is overall higher than the electron affinity of the ground singlet state for unsubstituted and halogenated hypericin, which indicates that the triplet state molecule also have the ability to quench superoxide.[58, 185]

In the absence of molecular oxygen in the closest vicinity of the reduced hypericin molecules, such as in the case of a locally anoxic environment, debromination reactions may occur and were studied through stepwise scanning of the C-Br bond. The energy of radical anion **1** during scanning of the C-Br bond is displayed in Figure 3.2. Possible transitions states were found for molecules **1**, **1***, **2**, and **2***, whereas for the molecules with the bromine atom positioned on the same side as the methyl groups, no transitions states could be identified. Table 3.2 displays the calculated reaction energies and transition barriers based on full optimization of the transition states of the molecules for which such were found.

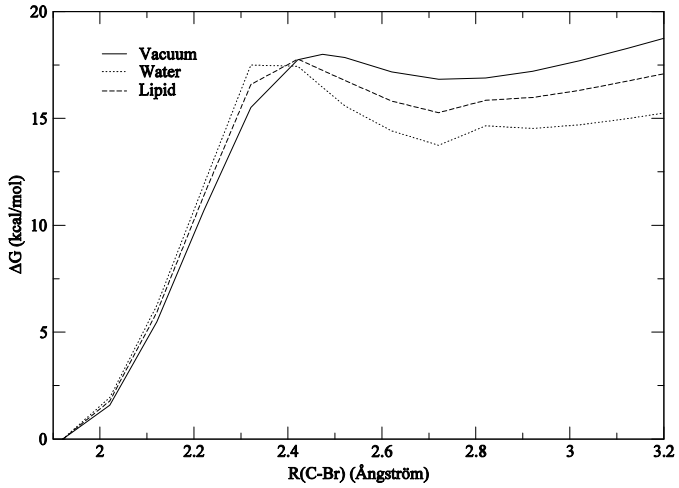

Figure 3.2. Results from scanning the C-Br distance in brominated hypericin radical anion **1**. All data at the B3LYP/6-31G(d,p) level. Reproduced by permission of John Wiley & Sons. http://onlinelibrary.wiley.com/doi/10.1002/qua.21689/full

Table 3.2. Debromination energies (kcal/mol) in different media.[a]

Bromin. site		*Vacuum*	*Lipid*	*Water*
1	Prod	53.9	24.8	12.1
	TS	15.5	14.1	12.9
2	Prod	53.9	24.8	12.1
	TS	15.6	13.7	12.6
1*	Prod	53.7	24.5	11.8
	TS	15.1	13.7	12.6
2*	Prod	53.7	24.5	11.8
	TS	15.1	13.7	12.6

[a] ZPE corrected energies (vacuum) and Gibbs free energies (solvent). Optimized structures, ZPE, and ΔG corrections: B3LYP/6-31G(d,p); Electronic and solvation energies: B3LYP/6-311+G(d,p).

The optimized C-Br distance of the transition state was found to be 2.465 Å for the double butterfly structures and 2.474 Å for the propeller structures. Compared with the data from the scannings, the transition states are lowered by full transition state optimization and inclusion of zero-point correction energies. The transition barriers are slightly decreased when going to more polar medium, whereas the overall reaction energies are significantly decreased by more polar medium. This finding is due to the fact that the bromine anion is more stabilized in solvents than in vacuum. The reactions are however still endergonic by ~12 kcal/mol in polar solvent. The reaction energies would most likely be altered by including a first solvation shell of water molecules, as the continuum models are not sufficient to describe solvated atomic anions. The relatively low reaction barriers (~13 kcal/mol) in aqueous solution, however, indicate that debromination may occur. Halogen-substituted pyrimidines, also potent antitumour and antiviral agents, have been shown to display similar types of reactions, involving formation of radical anions, followed by dissociation to from halide anions and pyrimidine radicals.[293]

Deprotonation of one of the hydroxyl groups in the *bay* region (cf. Figure 1.2) of brominated hypericin was studied as a possible alternative reaction that

can occur if the molecules are not directly reduced. Table 3.3 displays deprotonation energies, which were defined as the energy difference between the neutral molecules and the corresponding deprotonated anions. Adding the energy of a solvated proton, -268.67 kcal/mol (11.65 eV),[294] to the energies of the deprotonated species in polar environment gives either slightly exothermic (**1**, **2**, **1*-4***) or endothermic/thermoneutral (**3** and **4**) deprotonation in aqueous solution. *Bay* hydroxyl groups of hypericin have a pK_a value of 1.8 in polar solvents, indicating that the molecule would be deprotonated at physiological pH,[37] which is in agreement with the findings for a majority of the brominated species. However, the energy gain for deprotonation of the brominated molecules is overall lower compared to unsubstituted hypericin.[58] Deprotonation of the molecules most likely competes with the power of the molecules to extract an electron from the environment.

Table 3.3. Deprotonation energies (eV) in different media.[a]

Bromin. site	*Vacuum*	*Lipid*	*Water*
1	12.76	11.80	11.53
2	12.76	11.80	11.53
3	12.60	11.78	11.67
4	12.61	11.79	11.67
1*	12.74	11.77	11.51
2*	12.74	11.77	11.51
3*	12.52	11.70	11.59
4*	12.52	11.71	11.59

[a] ZPE corrected energies (vacuum) and Gibbs free energies (solvent). Optimized structures, ZPE, and ΔG corrections: B3LYP/6-31G(d,p); Electronic and solvation energies: B3LYP/6-311+G(d,p).

No transition states were found for the deprotonated molecules and the overall reaction energies were significantly higher than for the radical anions. Deprotonated hypericin is therefore unlikely to dissociate and would most probably stay in the deprotonated form.

Debromination of the neutral ground state molecules was not found to be energetically favourable either.

The present study shows that brominated hypericin has the ability to produce radical species through a mode of action slightly different from the ones that have been suggested for unsubstituted hypericin. Figure 3.3 displays the possible reactions that can occur for brominated hypericin after light excitation, as compared to unsubstituted hypericin for which possible reactions are displayed in Figure 1.3.

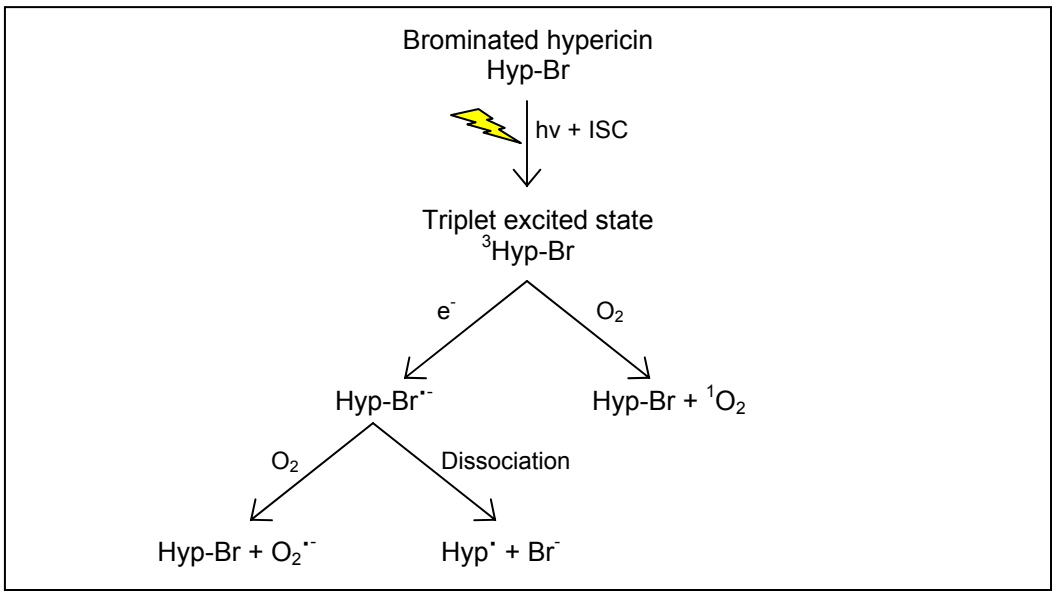

Figure 3.3. Possible photosensitized reactions for brominated hypericin.

If molecular oxygen is present in the closest vicinity of the photosensitizer, the triplet excitation energy of both unsubstituted and brominated hypericin can be directly transferred to molecular oxygen and form singlet oxygen. If reactions with molecular oxygen do not immediately occur, the hypericin molecule can instead extract an electron from the surrounding, generating a semiquinone radical anion that can further react. From the reduced hypericin molecule, an electron can be passed on to molecular oxygen to form superoxide, or, as was shown to be possible for some of the brominated hypericins, dissociation can occur. The dissociation reaction generates a hypericin radical that can either

react directly with biological molecules or react with molecular oxygen, forming superoxide. Brominated hypericin can consequently generate toxic species even in the absence of oxygen, which enables effective treatment of regions of tumours deficient in oxygen.

All possible reactive species; singlet oxygen, superoxide, hypericin radical anions, and neutral hypericin radicals, produced in the various possible reactions with brominated hypericin, can initiate damage to molecular targets. The specific species produced depends on the local environment of the photosensitizer, and the level of damage induced can depend on the specific reactive species formed and the concentration. As bromination enhances intersystem crossing to the triplet state compared to unsubstituted hypericin, a larger number of molecules are prone to further react and form any of the reactive species. This explains the increased quantum yield of ROS observed,[180, 183] and makes brominated hypericins likely to be more efficient therapeutic agents.

CHAPTER 4. PROPERTIES AND PERMEABILITY OF HYPERICIN AND BROMINATED HYPERICIN IN LIPID MEMBRANES (PAPER II AND IV)

Studies of the detailed mechanisms by which drug compounds interact with various biological molecules in the body are essential in the evaluation of their precise mode of therapeutic action. This information is also important in the development and evaluation of new therapeutic agents with improved properties. Computational techniques have evolved as useful tools in this field in the sense that interactions can be studied in detail at the atomic level. In the present and next chapter of this thesis, studies of hypericin in potential biomolecular systems that it possibly interacts with are presented.

The present chapter gives a detailed account of the behaviour of unsubstituted hypericin (Hy), monobrominated hypericin (Hy-Br; bromine at position 1, Figure 1.2), and tetrabrominated hypericin (Hy-4Br, bromines at positions 1-4, Figure. 1.2) in a pure DPPC lipid membrane (Paper II) and in two cholesterol containing membranes (Paper IV). The latter membranes contain 9 and 25 mol% cholesterol; concentrations that are commonly found in natural membranes. Lipid membranes with and without cholesterol have been subject to numerous computational studies applying Monte Carlo and MD simulation techniques. The studies have shown that computational methods have the ability to reproduce many of the experimental observations in membranes. Computational studies also contribute to information at the atomic level that is hard to obtain experimentally.

4.1. Computational methodology

The pure DPPC bilayer model was composed of 64 lipids and 3846 water molecules,[295, 296] whereas the model used to replace lipid molecules by cholesterol molecules was initially composed of 128 DPPC lipids and 3655 water molecules.[297-300] 12 and 32 lipids were randomly replaced in order to construct the 9 mol% and 25 mol% cholesterol membranes, respectively. The same number of lipids was replaced in each monolayer. Unconstrained

simulations with two hypericin molecules in each membrane were performed. After equilibration, the pure DPPC membrane system was simulated for 50 ns and the cholesterol containing systems for 100 ns.

Simulations with each hypericin derivative at constrained distances differing by 0.1 nm along the z axis direction were performed in order to collect the z-component of the force (F_z) acting on the molecule at each position along the z axis. The molecules were constrained in the z direction, but allowed to rotate. The free energy for the transfer process between z_i and z_f was calculated using,

$$\Delta G = G_{z_f} - G_{z_i} = -\int_{z_i}^{z_f} \langle F_z \rangle_z dz \tag{4.1}$$

where the bracket represents an average over the forces collected at each constrained distance.

The procedure developed by Marrink and Berendsen[301] was adopted to calculate permeability coefficients, based on the fluctuation dissipation theorem and using the deviation of the instantaneous force, $F(z,t)$, from the average force acting on the molecule obtained during the constrained simulations. The diffusion coefficient, D, is calculated from the autocorrelation function of the constrained force, $C(t)$,

$$D(z) = (RT)^2 / \int_0^{\infty} C(t)dt \tag{4.2}$$

where R is the gas constant and T is the absolute temperature.

The permeability coefficient, P, is calculated by integrating over the local resistance across the membrane, $R(z)$, which is obtained by dividing the exponential of the free energy, $\Delta G(z)$, by the diffusion coefficient, $D(z)$,

$$1/P = \int R(z)dz = \int_{z_i}^{z_f} \frac{exp(\Delta G(z)/kT)}{D(z)} dz \tag{4.3}$$

All simulations were performed in the GROMACS program (Paper II: version 3.3.3;[302, 303] Paper IV: version 4.0.4[304]) together with the united atom GROMACS force field. A time step of 2 fs was used throughout the study. The isothermal-isobaric ensemble (NPT) with a temperature of 323 K and pressure of 1 bar was applied.

4.2. Results and discussion

The unconstrained MD simulations were performed with two hypericin molecules of each derivative in the systems, one initially positioned in the water phase and one in the middle of the bilayer. All three hypericin molecules show strong preference to accumulate in the lipids, close to the polar headgroups and the interface between the lipids and water. Despite this being the densest region of the membrane, the large and inflexible hypericin molecules accumulate here due to favourable interactions between the hydroxyl groups and water molecules that penetrate into the lipid region. This region has also been found favourable for smaller drug molecules, such as psoralens, 5-ALA and derivatives thereof.[305, 306]

Snapshots from simulations of hypericin in the three membranes are displayed in Figure 4.1. As the pure DPPC membrane contains half the number of lipids compared to the cholesterol containing membranes, in order to compare the volumes of the three membranes properly, the volume of this membrane should be increased by a factor of 2. Taking this into account, it is clear that the presence of cholesterol in the membrane significantly reduces the area per lipid and induces higher order of the lipids. These effects are more prominent with increased concentration of cholesterol. The 25 mol% cholesterol membrane is compressed to half the original size of a pure DPPC membrane containing the same number of lipids. The calculated areas per lipid are in good agreement with results from previous computational studies.[307] The condensing and ordering effects of cholesterol on membranes have been well-documented in experimental[308-311] and computational studies.[307, 312-318]

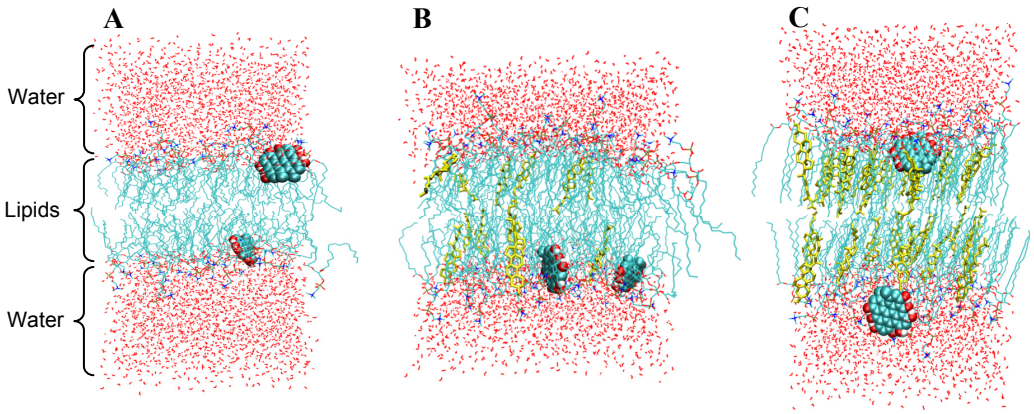

Figure 4.1. Snapshots from simulations showing two hypericin molecules in DPPC bilayers with (A) 0 mol%, (B) 9 mol% and (C) 25 mol% cholesterol. Cholesterol molecules are displayed in yellow. Reproduced by permission of the American Chemical Society. http://pubs.acs.org/doi/abs/10.1021/ct9002702, http://pubs.acs.org/doi/abs/10.1021/ct100528u

Figure 4.2 displays density profiles for all components in the systems during the MD simulations. The density profiles show that the preferred location for the hypericin molecules is not significantly affected by the presence of cholesterol in the membrane and it is clearly seen that the molecules preferentially accumulate in the headgroup region, approximately 1-2 nm from the bilayer centre, as was also seen in Figure 4.1. Although all three hypericin derivatives prefer this region in all membranes, some small variations are found. For Hy and Hy-Br, it is found that the molecule that enters the bilayer from the water phase in several cases ends up closer to the interface between the lipids and water than the molecule that was initially located in the lipids. Hy-4Br behaves slightly different from Hy and Hy-Br in that this molecule overall displays wider density profiles and moves closer to the bilayer centre. This location reduces the interactions with water molecules.

Free energy profiles for the transport process of the hypericin molecules across the bilayer were calculated using a potential of mean force formalism based on MD simulations with the hypericin molecules at constrained distances from the bilayer centre. Free energy profiles for the hypericin molecules in the three membranes are displayed in Figure 4.3.

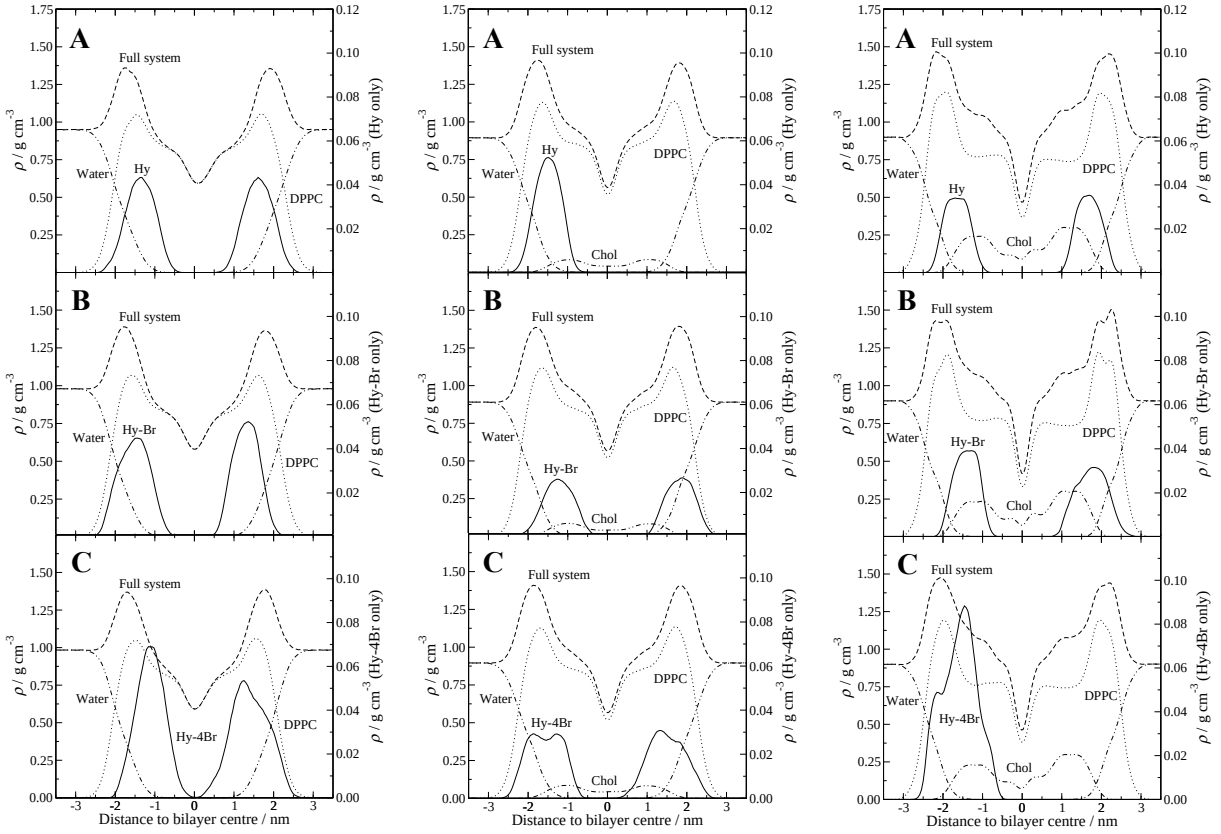

Figure 4.2. Density profiles for two hypericin derivatives (A, Hy; B, Hy-Br; C, Hy-4Br) in DPPC bilayers with 0 mol% cholesterol (left), 9 mol% cholesterol (middle) and 25 mol% cholesterol (right). Reproduced by permission of the American Chemical Society. http://pubs.acs.org/doi/abs/10.1021/ct9002702, http://pubs.acs.org/doi/abs/10.1021/ct100528u

Local minima were found in the region of the bilayer where the molecules were found to accumulate in the unconstrained simulations, indicating that transport into this region is associated with an energy gain. The size of the minima depends on the molecule and the amount of cholesterol in the membrane. Hy-Br displays the deepest minimum both in the cholesterol containing and cholesterol absent membranes, and this minimum becomes deeper with increased amount of cholesterol. This indicates that transport from the water phase into the lipids is most favourable for Hy-Br and that the presence of cholesterol enhances this transport. For Hy-4Br, the minimum also becomes deeper when cholesterol is included. However, the decrease in free

energy when the cholesterol concentration is increased from 9 to 25 mol% is almost negligible for this molecule. The energy of the minimum is overall higher for Hy-4Br than for Hy-Br. For Hy, the opposite pattern is found; the minimum becomes less deep with increased amount of cholesterol and the minimum for this molecule is overall higher than the two other molecules or equal to Hy-4Br. This finding indicates that diffusion into the lipids is least favourable for Hy and that cholesterol has a negative effect on the transport of this molecule.

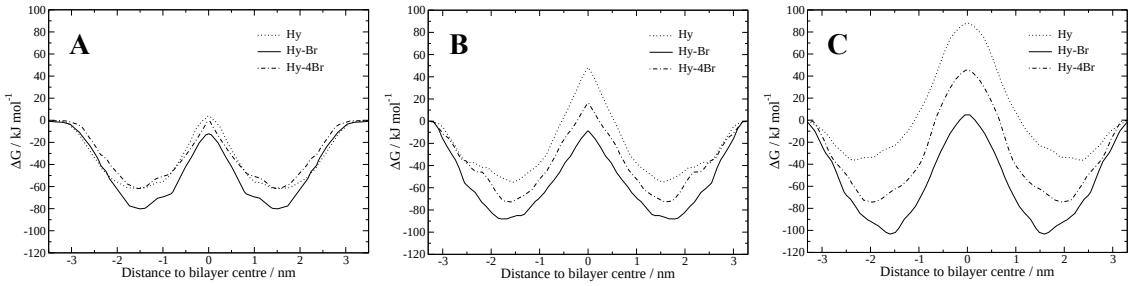

Figure 4.3. Free energy profiles for the hypericin derivatives inside the (A) 0 mol%, (B) 9 mol%, and (C) 25 mol% cholesterol membranes. Reproduced by permission of the American Chemical Society. http://pubs.acs.org/doi/abs/10.1021/ct9002702, http://pubs.acs.org/doi/abs/10.1021/ct100528u

As the molecules continue moving across the bilayer, the free energy increases and shows a maximum in the very middle of the bilayer. The free energy barriers in this region become higher for all three molecules with increased cholesterol concentration. This is explained by the fact that the two monolayers of the membrane are more separated in the more ordered systems with cholesterol and this gives a region of free space in the very centre of the bilayer. This free space offers less possible interactions with lipids for the hydrophobic hypericin molecules, and thereby generates a larger increase in free energy, indicating that this region is very unfavourable to diffuse into/across. The increased free space in the middle of the bilayer is most evident in the 25 mol% cholesterol membrane and the free energy barriers to pass

through this region are subsequently higher than in the membranes with lower cholesterol content. The increased bilayer thickness and the reduced DPPC density in the middle of the bilayer caused by cholesterol are also seen in Figure 4.1 and Figure 4.2. These observations have also been made in previous experimental and computational studies of cholesterol containing membranes.[307, 319]

The energy barrier in the middle of the bilayer is the lowest for Hy-Br in all three membranes. This together with the overall deepest free energy minima in the headgroup region indicates that Hy-Br would display the overall most favourable diffusion through a membrane, independent on the presence of absence of cholesterol.

In addition to the favourable free energy profiles for Hy-Br, calculated permeability coefficients show faster overall diffusion for Hy-Br in all three membranes, followed by Hy-4Br and Hy, respectively (Table 4.1). This gives further evidence for that Hy-Br would have the highest probability to translocate across a membrane. The permeation of Hy and Hy-4Br is significantly reduced in the cholesterol containing membranes, whereas Hy-Br is not considerably affected by the inclusion of cholesterol. The permeability coefficient for Hy-Br is only reduced by a factor of 10 in the 25 mol% cholesterol membrane compared to in the pure DPPC membrane, and this molecule even shows an increase in permeation in the 9 mol% cholesterol membrane compared to in the pure DPPC membrane. Hy displays the overall slowest diffusion through the membranes. This finding can be explained by stronger interactions with water molecules and possibly also with cholesterol molecules.

Halogenated drugs have previously been reported to display larger permeability coefficients compared to non-halogenated molecules.[320] Hy-4Br, however, shows a reduced permeability compared with Hy-Br, a finding that is probably an effect of the presence of four large bromine atoms that have an opposite effect on the ease of permeation.

Table 4.1. Permeability coefficients of the hypericin derivatives inside the membranes without and with cholesterol (cm s^{-1}).

Molecule	*0 mol% cholesterol*	*9 mol% cholesterol*	*25 mol% cholesterol*
Hy	4.21×10^{-4}	8.25×10^{-12}	1.63×10^{-17}
Hy-Br	4.94×10^{-3}	5.49×10^{-3}	4.12×10^{-4}
Hy-4Br	1.51×10^{-3}	3.31×10^{-6}	6.93×10^{-11}

The results from the presented studies indicate that hypericin molecules show strong preference for lipid membranes, in which they accumulate in the headgroup region, close to the interface between the lipids and water, due to favourable interactions with water molecules. The studies show that cholesterol, an essential component in natural membranes, is important to include in membrane models as its presence often affects the behaviour of drug molecules considerably. The three hypericin molecules are affected differently by the presence of cholesterol in the membrane, either by enhancing or counteracting permeation through the membrane.

It has recently been indicated that hypericin interacts strongly with cholesterol molecules in membranes due to the common planar structure that enables π electron interactions.[136] Unsubstituted hypericin was found to locate closest to cholesterol during the MD simulations. However, no direct interactions were found in the present studies. If hypericin were to strongly interact with cholesterol, this could explain transportation of hypericin between intracellular membrane sites mediated by cholesterol trafficking. Due to the limited amount of data from the present MD simulations, possible interactions with cholesterol can however not be completely ruled out.

The cholesterol molecules were not found to interact directly with each other at the studied concentrations; instead they prefer to be solvated by DPPC lipids, in agreement with previous theoretical observations.[321] The hypericin molecules were not found to interact with each other either at the low concentrations included in the studies. However, when the concentration of hypericin is increased (10 Hy), the molecules form dimers or aggregates of four molecules

positioned face to face in the water phase (unpublished data). The aggregates were not found to negatively alter the diffusion into the lipids significantly and the interactions between the molecules were maintained also inside the lipids. These aggregates have experimentally been observed for hypericin in solution.[118, 119]

Experimental studies have found hypericin in various intracellular components, indicating that the molecule has the ability to penetrate the plasma membrane. As the monobrominated hypericin molecule was found to have the highest capability to penetrate membranes, both with and without cholesterol, the probability to find this molecule within a cell would be higher than unsubstituted hypericin and tetrabrominated hypericin. A photosensitizer that to a higher degree is transported into a cell would generate a stronger photodynamic effect as a larger number of molecules are capable of being activated in the potential intracellular target site and produce radical species. This suggests that monobrominated hypericin likely displays more promising properties than unsubstituted hypericin for being utilized in PDT.

Unsubstituted hypericin and tetrabrominated hypericin are expected to accumulate to a higher extent in the plasma membrane compared to monobrominated hypericin, and this would thus result in that a smaller number of these molecules reaches the interior of a cell and possible targets therein. Photodamage can however also be initiated by molecules located within the plasma membrane,[137-139] and this can subsequently contribute to the damage caused by drug molecules that have reached intracellular sites.

It must however be stressed that diffusion is not the only possible way that drug molecules enter cells. Assisted transport by carriers such as LDL or liposomes that are able to solubilise the hydrophobic hypericin molecules in the blood can alter the mechanism by which the molecules are taken up by cells.

CHAPTER 5. SARCO(ENDO)PLASMIC RETICULUM Ca^{2+} ATPase IS A POSSIBLE TARGET FOR HYPERICIN (PAPER VII)

The studies presented in Chapter 4 provide details on the behaviour of hypericin and derivatives thereof in lipid membranes, information that is useful in predicting the ability of the molecules to penetrate the plasma membrane of a cell through diffusion. Hypericin clearly has the ability to enter a cell as the molecule has been identified in numerous intracellular locations that constitute possible sites for binding. However, the exact cellular target for hypericin has not yet been fully determined.

One of the organelles in which hypericin has been found is the ER, one of the most important intracellular Ca^{2+} stores.[85, 156, 157] Cells treated with PDT-hypericin display disruptions in the Ca^{2+} homeostasis, with increased Ca^{2+} concentration in the cytosole and decreased Ca^{2+} concentration in the lumen of the ER,[158] effects that have been observed for other photosensitizers as well.[322-325] The SERCA protein (Figure 5.1C) located in the ER membrane is essential for maintenance of a low resting concentration of Ca^{2+} in the cytosole and has been shown to be depleted in cells treated with hypericin,[158, 161] a finding that can explain the loss of pumping activity in the cells.

The damages caused by hypericin were found to be due to singlet oxygen production and resulted in cell death. Singlet oxygen can either be produced in the ER membrane from which it diffuses to the protein, or the photosensitizer itself can be located within the protein when it is activated. As singlet oxygen has a short lifetime and hence a small radius of action, the binding site of hypericin is likely within the protein or in the very close vicinity. Initial diffusion of hypericin into the ER membrane followed by diffusion to binding sites within the transmembrane region of the protein is a possible mechanism. The binding pockets of the known inhibitors thapsigargin (TG; Figure 5.1A[326-328]) and di-*tert*-butylhydroquinone (BHQ; Figure 5.1B[329, 330]) in the transmembrane region of SERCA are located at the same level in the membrane as the preferred location of hypericin in lipid membranes (cf. Chapter 4).

In order to study if the observed disruption in SERCA levels in hypericin treated cells possibly involves binding of hypericin to the protein, interactions between hypericin and SERCA were studied. The TG and BHQ inhibitors were included in the study for comparison. The inhibitors bind to the protein in the Ca^{2+} absent state and inhibit Ca^{2+} pumping by blocking Ca^{2+} binding or conformational changes in the protein. The binding of TG and BHQ to SERCA have previously been evaluated in computational docking studies.[331, 332] SERCA has also been used as target for virtual screening of potent inhibitors for use in prostate cancer treatment.[333]

5.1. Computational methodology

As no crystal structure of SERCA2, the isoform that most likely is present in tumour cells, exists, a homology model was created using the built-in methodology[334] in the YASARA program.[335] The splice variants SERCA2A and SERCA2B only differ in the C-terminus, in which residues 994-997 in SERCA2A are substituted with a longer tail, residues 994-1042, in SERCA2B. As the C-terminus (left-most helix in Figure 5.1C) is located in the cytosolic region and most likely does not alter the binding of drug molecules to the protein, a homology model of SERCA2A was created to represent the SERCA2 isoform. The crystal structure of rabbit SERCA1A (PDB ID: 2AGV;[336] Figure 5.1C) was used as the major template.

The SERCA1A crystal structure and the SERCA2A homology model were embedded in palmitoyloleoylphosphatidylethanolamine (POPE) lipid membranes and equilibrated for 38 ns. A snapshot from a simulation of SERCA1A embedded in a membrane is displayed in Figure 5.1D.

The Molecular Operating Environment (MOE) program[337] with the built-in Alpha Site Finder[338, 339] was initially used to locate probable binding sites in SERCA, other than the TG and BHQ binding sites. TG and BHQ were docked in their respective binding sites in the transmembrane region of the protein, and hypericin was, apart from in these two sites, docked in two additional sites

indicated by the Alpha Site Finder tool (Figure 5.1C). The same binding sites were considered in both SERCA1A and SERCA2A. The residues important for TG and BHQ binding are present in both isoforms. Docking was performed using Autodock[340] as implemented in YASARA. The docked ligands and the closest surrounding of the proteins were simulated for 20 ns. Binding energies of the ligands with respect to the protein were defined as the potential energy difference between the bound and unbound state (the ligand at infinite distance from the protein). Ensemble average binding energies were calculated from the energy minimized simulation snapshots of the last 15 ns of the MD simulations (600 snapshots for each system).

The AMBER03 force field[341] was used together with a multiple time step of 2×1.25 fs throughout the study. All simulations were performed at a temperature of 298 K. Snapshots were saved every 25 ps during the simulations.

5.2. Results and discussion

The homology model of SERCA2A and the SERCA1A crystal structure display highly similar structural features and superpose very well (Figure 5.2A), a finding that is expected due to the high sequence identity (84 %). In Figure 5.2C and 5.2E respectively, magnifications of the superposed TG and BHQ pockets of the crystal structure of SERCA1A and the homology model of SERCA2A are displayed, with the amino acids that are known to interact with the inhibitors highlighted. The binding pockets in the two isoforms clearly share high structural similarities.

During the membrane embedding and MD simulation, structural changes were however induced in the proteins, resulting in more pronounced differences between the two isoforms (Figure 5.2B). This is seen in the superposed TG pockets that display larger differences than before the MD simulation (Figure 5.2D), mainly due to that this pocket in SERCA1A became slightly enlarged during the simulation. The BHQ pockets were not significantly affected by the

membrane embedding and MD simulation, but larger structural differences between the isoforms are seen in this pocket as well compared to before the MD simulation (Figure 5.2F).

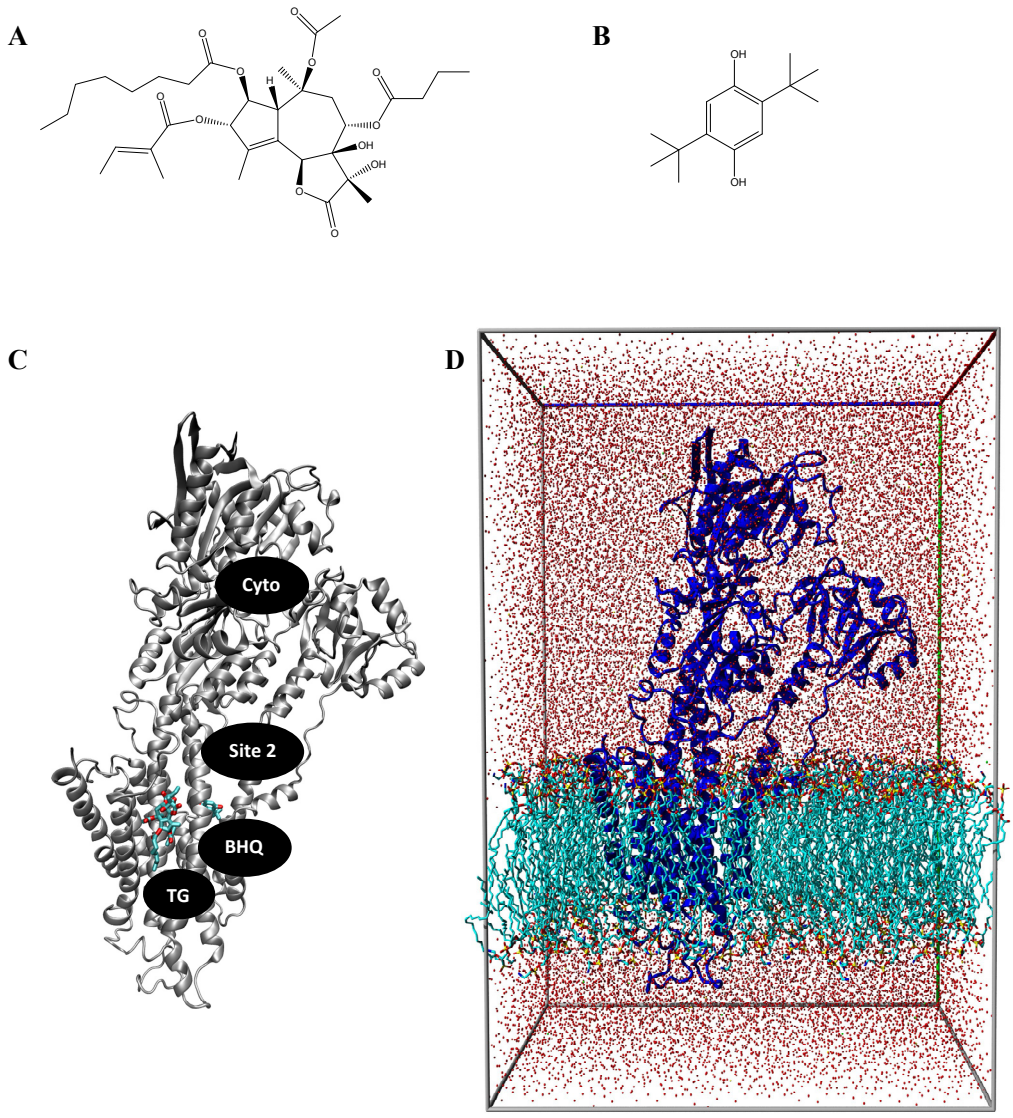

Figure 5.1. Chemical structures of (A) TG and (B) BHQ. (C) The crystal structure of SERCA1A with the bound TG and BHQ inhibitors (PDB ID: 2AGV[336]) and the binding pockets subject to docking of hypericin displayed, and (D) a snapshot from the MD simulation of SERCA1A in a membrane.

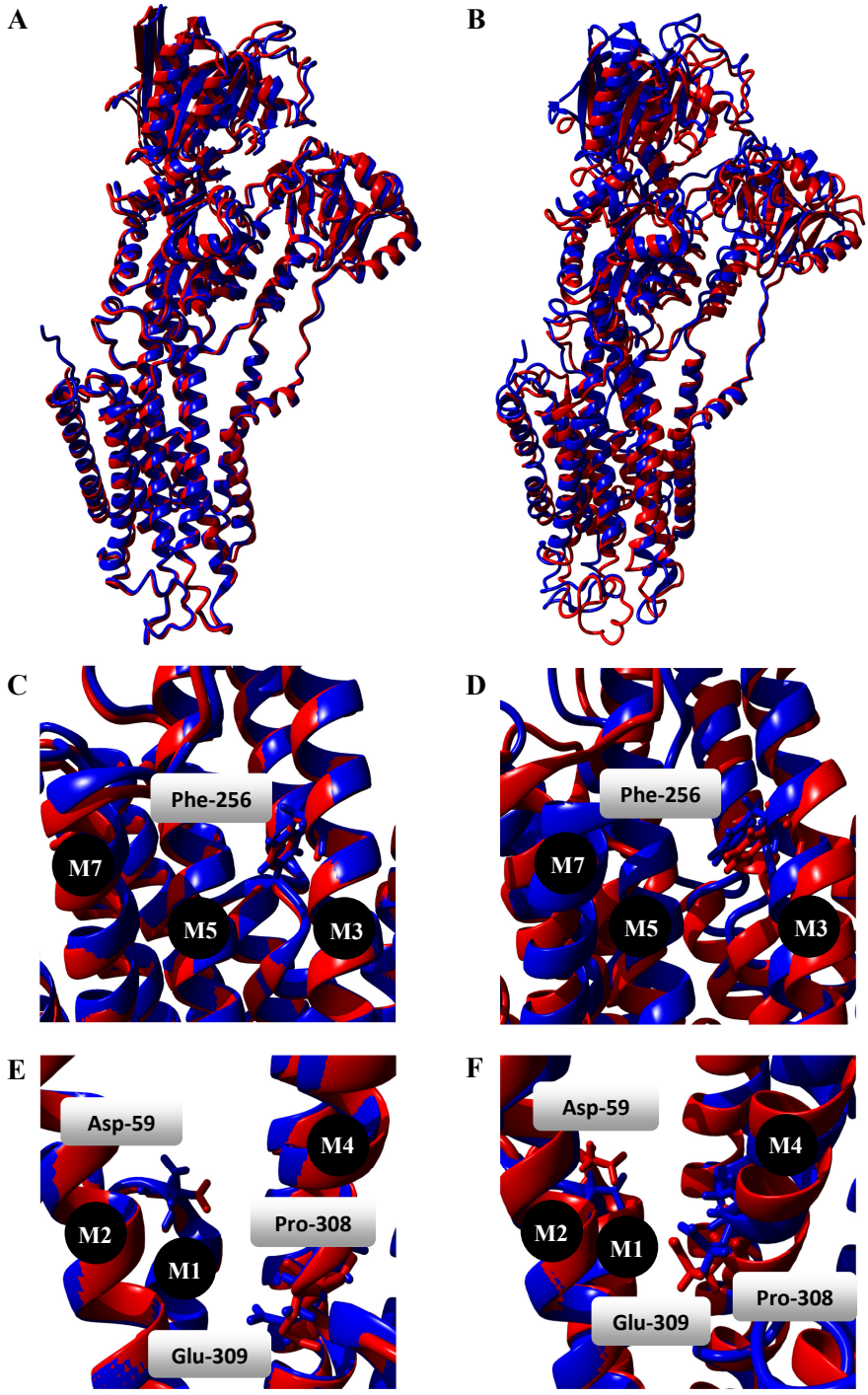

Figure 5.2. Superposed backbones of the homology model of SERCA2A (blue) with the major template of SERCA1A (red) (A) before and (B) after membrane embedding, MD simulation and energy minimization. Magnifications of the superposed (C and D) TG binding pockets and (E and F) the BHQ binding pockets.

Hypericin, TG, and BHQ were docked in the membrane-embedded SERCA1A and SERCA2A proteins. Hypericin was, apart from in the TG and BHQ binding pockets, docked in two possible sites found by the Alpha Site Finder in MOE; one in the cytoplasmic region of the protein close to the ATP binding site, and one close to the BHQ binding site, but closer to the cytosole. Ensemble average binding energies for the ligands with respect to the proteins in the different binding sites are displayed in Table 5.1.

The binding modes for TG and BHQ, together with the most favourable binding modes for hypericin in SERCA1A and SERCA2A are displayed in Figure 5.3 and Figure 5.4, respectively. Amino acid residues that the ligands interact with are highlighted.

Table 5.1. Ensemble average binding energies (kJ/mol) for ligands in SERCA1A and SERCA2A. The average of the absolute deviations from the mean are given in parenthesis.

Ligand	*Site*	*SERCA1A*	*SERCA2A*
TG	TG	364 (±11)	464 (±34)
TG	TG*	365 (±23)	286 (±33)
Hypericin	TG	264 (±31)	348 (±54)
Hypericin	TG*	297 (±36)	279 (±36)
BHQ	BHQ	126 (±40)	219 (±8)
Hypericin	BHQ	380 (±6)	281 (±20)
Hypericin	Site 2	399 (±31)	318 (±48)
Hypericin	Cytosole	421 (±18)	394 (±66)

* Docking performed without lipid in binding pocket.

Although the TG and BHQ binding pockets are located adjacent to each other in the transmembrane region of the protein, they differ significantly in structure and size; hence constitute specific affinities for the two structurally different inhibitors. The BHQ binding pocket is a small cavity made up by the M1, M2, and M4 helices (Figure 5.2E/F), whereas the TG binding pocket on

the other hand is narrow but extended in length, made up by the three almost parallel M3, M5, and M7 helices (Figure 5.2C/D). The shape and size of the TG binding pocket make this a suitable location for lipids, and during the MD simulations of the proteins in the membranes lipids find this location favourable. Docking of ligands with a lipid present in the TG binding pocket subsequently resulted in location of the ligands outside the pocket, and during the MD simulations neither TG nor hypericin had the ability to push the lipid out from the pocket, a situation that would require significantly longer simulation times. Docking of TG and hypericin in the TG pocket was performed with and without a lipid present in the pocket in order to sample both situations ('*' in Table 5.1 indicates that a lipid was removed before docking). Binding modes for TG generated after docking and MD simulation both with and without a lipid in the pocket are displayed in Figure 5.3 and 5.4.

The binding mode of TG in the TG pocket with no lipid in both SERCA1A and SERCA2A naturally resembles the one in the crystal structure of SERCA1A more than when a lipid is present. When a lipid is present in the pocket, TG binds above the location seen in the crystal structure, and in SERCA2A the binding is even higher up in the pocket than in SERCA1A. Despite the highly different binding modes of TG in the presence (Figure 5.3A) and absence (Figure 5.3B) of a lipid in SERCA1A, the ensemble average binding energies are the same. In SERCA2A, on the other hand, the two binding modes of TG differ significantly in binding energy, and the binding mode resulting from the presence of a lipid in the TG pocket (Figure 5.4A) generated the overall highest ensemble average binding energy throughout the study. In the absence of a lipid in the TG pocket of SERCA2A (Figure 5.4B), TG locates at the surface of the pocket, a location that generates very few interactions with amino acids and this explains the very low binding energy.

Docking of BHQ in both isoforms generated this molecule in a similar binding mode as in the crystal structure of SERCA1A. In SERCA1A, BHQ exhibited high flexibility and movement during the MD simulation and locates mainly in two regions of the pocket, one that allows close interaction with Glu-

309 (Figure 5.3D), whereas in the other binding mode less interactions with amino acids are possible and the binding energy is subsequently lower. The ensemble average binding energy during the MD simulation is the lowest found for any ligand in the present study. In SERCA2A the BHQ molecule displays significantly less flexibility and the binding mode after the MD simulation is similar to the one in the crystal structure of SERCA1A, with hydrogen bonds formed with Asp-59 and Pro-308 (Figure 5.4D). The binding energy in this isoform is more stable and overall higher than in SERCA1A. The binding energy for BHQ in both isoforms is significantly lower than that for TG, indicating that BHQ binds significantly weaker than TG, in agreement with experimental observations.[328, 329] The binding energy for BHQ is also overall lower than that for hypericin in all pockets included in this study.

For hypericin in the TG binding pocket of SERCA1A, neither the binding mode nor the binding energy was as affected by the presence or absence of a lipid as for TG, likely due to that hypericin has a planar structure that can fit into the TG pocket even when a lipid is present. In SERCA2A, on the other hand, the difference in both binding mode and binding energy for hypericin in the presence and absence of a lipid in the pocket is larger. When a lipid is present, hypericin binds high up in the TG pocket, close to the location of TG when a lipid is present. The binding energy for this mode is higher than that in the absence of a lipid, in which hypericin binds significantly further down in the pocket. The binding energy in the presence of a lipid is also higher than that for hypericin with and without a lipid in the TG pocket of SERCA1A. The binding of TG and hypericin high up in the TG binding site can be assumed to constitute alternative binding sites possible for binding in the case of an already occupied TG pocket, such as if the drug concentration is high.

Hypericin binds tightly in the BHQ pocket in both isoforms of SERCA and displays higher binding energy than BHQ. The binding mode of hypericin differs slightly between the two isoforms, resulting in interactions with different residues in the pocket. Hypericin binds significantly stronger in the BHQ pocket in SERCA1A than in SERCA2A. Both BHQ and hypericin interact

strongest with Glu-309 in SERCA1A, whereas in SERCA2A the binding of the molecules is shifted towards Asp-59. The strong interaction between Glu-309 and hypericin and BHQ in SERCA1A results in a shift of the sidechain of Glu-309 to the same side of the M4 helix as the BHQ binding pocket, such that it does not hinder Ca^{2+} to enter into the binding site at the other side of the M4 helix. This location of the sidechain is opposite to the one in the crystal structure in which the presence of BHQ hinders Glu-309 from opening the Ca^{2+} gate. It is possible that the Ca^{2+} gate in the locked open state, caused by the presence of BHQ or hypericin, can block Ca^{2+} transport as well, but this has not been observed experimentally. If this is possible, hypericin can inhibit SERCA through a light-independent mechanism, giving evidence for dark toxicity.

The overall most favourable binding site for hypericin in SERCA1A and SERCA2A was found to be neither the TG nor the BHQ pocket, but instead a pocket in cytoplasmic region of the protein, close to the ATP binding site (Figure 5.3C and 5.4C). The binding energy for hypericin in the cytoplasmic region is almost equally high in the two isoforms, although slightly lower in SERCA2A. In SERCA1A, this binding is even stronger than that for TG, whereas in SERCA2A, TG displays the strongest overall binding. Binding of hypericin in the cytoplasmic region of SERCA can influence phosphorylation of the protein as hypericin interacts strongly with Phe-487, a residue that is essential for ATP binding.[342] This can be a possible additional mechanism by which hypericin displays dark toxicity with SERCA.

Strong binding for hypericin in SERCA1A was also found in the BHQ binding pocket and in a site outside this pocket (‘Site 2’, cf. Figure 5.1C); two sites that are less favourable in SERCA2A. In SERCA2A, hypericin was bound relatively strongly in the TG binding site with a lipid present in the pocket. This is the only pocket in which hypericin binds stronger in SERCA2A than in SERCA1A.

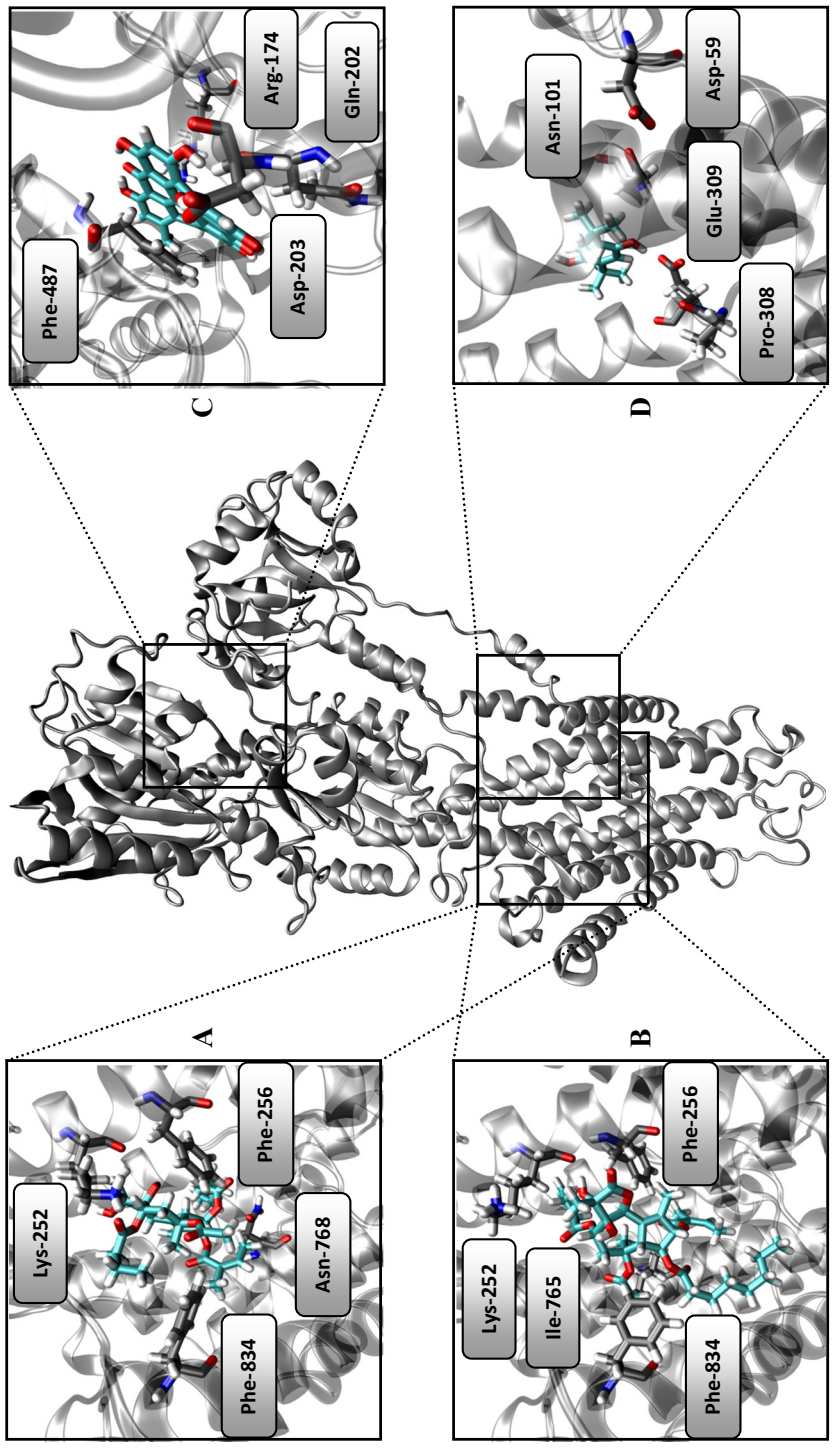

Figure 5.3. Binding modes for TG (docked (A) with and (B) without a lipid in the binding pocket) and (D) BHQ in their respective binding pockets, and (C) hypericin in the cytoplasmic region of SERCA1A. Carbon atoms of the ligands are displayed in cyan and carbon atoms of amino acid residues are displayed in grey.

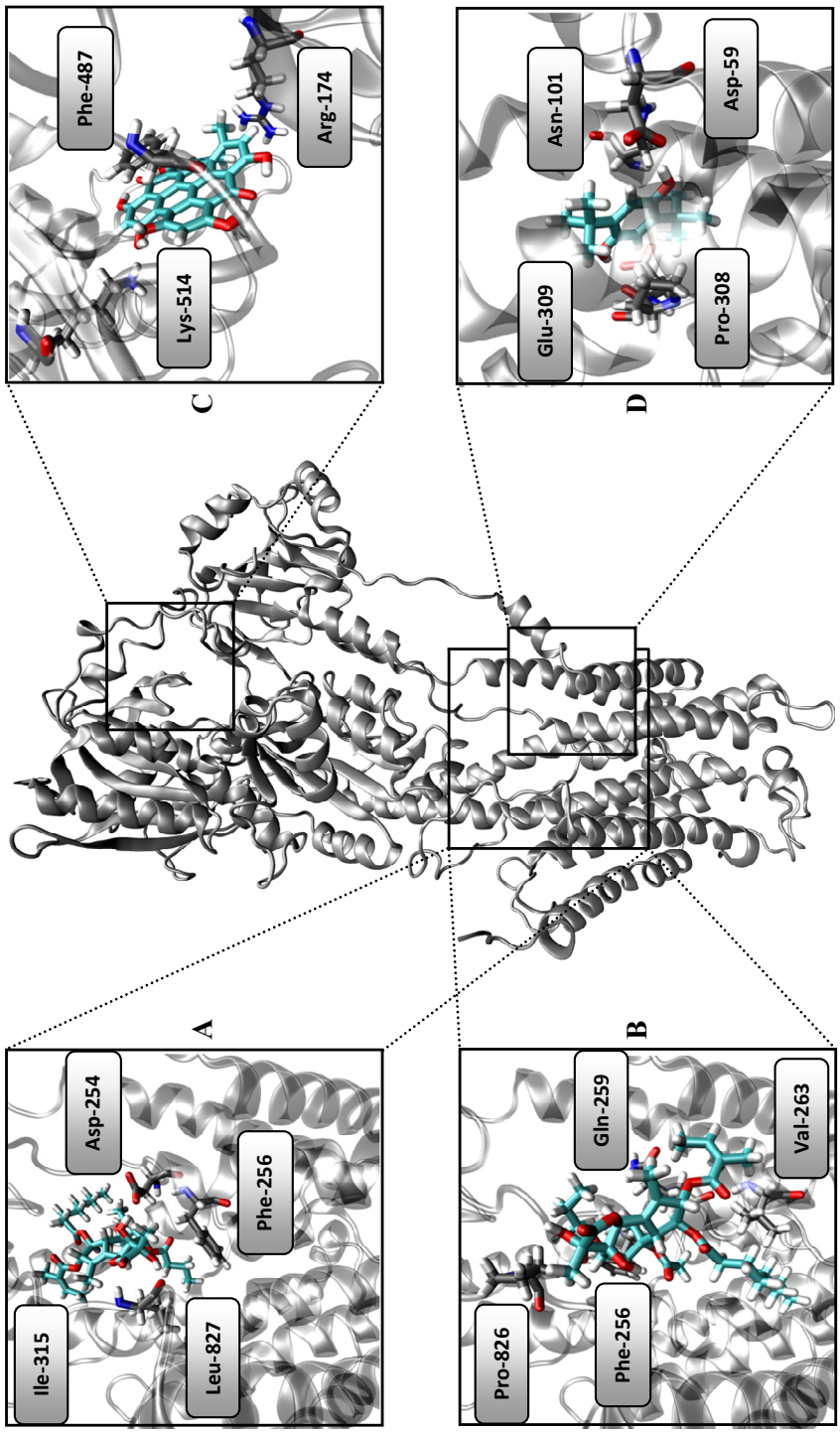

Figure 5.4. Binding modes for TG (docked (A) with and (B) without a lipid in the binding pocket) and (D) BHQ in their respective binding pockets, and (C) hypericin in the cytoplasmic region of SERCA2A. Carbon atoms of the ligands are displayed in cyan and carbon atoms of amino acid residues are displayed in grey.

The presented results show that hypericin most likely displays high binding affinity for SERCAs, which can explain the experimental observations of disrupted Ca^{2+} and protein levels in cells treated with hypericin. Hypericin was found to bind strongly both in pockets within the transmembrane region and in the cytoplasmic region of the protein; however, the two isoforms differed slightly in the preference for favourable binding sites.

Binding of hypericin in the TG or BHQ binding pockets can possibly stabilize the protein in a conformation that inhibits conformational changes or blocks Ca^{2+} binding essential for Ca^{2+} pumping, similar to the action of TG and BHQ, indicating that hypericin could display dark toxicity properties. However, in the presence of light in PDT treatment, the principal cause of action of hypericin would not be inhibition of conformational changes or blocking of Ca^{2+} binding as the excited molecule generates ROS that damage and degrades the protein, or induce lipid peroxidation, processes that lead to cell death.

The present study and the studies on the behaviour of hypericin in lipid membranes (Chapter 4) provide detailed information on possible mechanisms by which hypericin acts as a photosensitizer in cellular environments.

CHAPTER 6. CALCULATIONS OF ABSORPTION SPECTRA OF TETRAPYRROLE COMPOUNDS AND COMPUTATIONAL DESIGN OF NEW PHOTOSENSITIZERS FOR PDT (PAPER III, V AND VI)

Many photosensitizers available on the market today possess properties that do not make them ideal for being used in PDT. Long-lasting photosensitization and weak light absorption at wavelengths too short for optimal tissue penetration are among the most troublesome limitations associated with several known photosensitizers. One of the most important aspects to consider in the development of new photosensitizers is hence the absorption properties.

Computational techniques can be used to predict compounds with suitable properties that can be further tested experimentally for their possible application as photosensitizers in PDT. In order to be able to use computational techniques for this purpose, it is important to evaluate the performance of the methods with respect to available experimental data. Absorption spectra can be accurately calculated and have been subject to numerous studies. As most correlated *ab initio* methods are very computer-demanding when large systems are considered, a major aim would be to identify TD-DFT approaches with improved accuracy, with regards to calculations of spectroscopic properties, that can be used as efficient alternatives. In Section 2.1.5.1, several benchmarking studies of the performance of TD-DFT with various functionals on their ability to predict absorption spectra were presented. In PDT, light at long wavelengths is used to activate the photosensitizers and the ability to computationally reproduce the absorption in this region of the spectra is hence the main focus.

The performance of TD-DFT in combination with various functionals, among them newly developed long-range corrected functionals, in calculations of vertical low-lying singlet excitations of a set of photosensitizing tetrapyrrole compounds, was investigated in Paper III and V. Based on the results from the two benchmarking studies, modified chlorin based compounds were designed and their spectroscopic properties investigated in Paper VI.

6.1. Computational methodology

Different combinations of functionals were used in geometry optimizations and excited state TD-DFT calculations of various tetrapyrrole compounds. All calculations were carried out in the Gaussian 09 program.[343]

In the study of Tookad (Figure 1.5C) and its metal-free analogue BPheid (Paper III), B3LYP and M06 were used in geometry optimizations of the ground singlet states and B3LYP, M06HF and ωB97XD were used to calculate vertical singlet excitation energies in toluene and tetrahydrofuran (THF), applying the IEF-PCM model.[288, 289] For the Tookad and BPheid geometries optimized using B3LYP in toluene, vertical singlet excitation energies were also calculated using CAM-B3LYP, M06, M062X, ωB97X, ωB97, LC-ωPBE, and PBE0. The LanL2DZ basis set was used for Pd throughout the study, and the 6-31+G(d,p) basis set was used for all other atoms in the geometry optimizations, whereas 6-311+G(2d,2p) was used in the excited state calculations.

In the next study (Paper V), the ground singlet state of chlorin (Figure 1.4B), porphyrin (Figure 1.4A), protoporphyrin IX (Figure 1.5A), and phytoporphyrin (Figure 1.5B) was optimized with B3LYP, ωB97XD and M06 and vertical singlet excitation energies were calculated with ωB97, ωB97X, and ωB97XD. Foscan (Figure 1.5D), chlorin e6 (Figure 1.5E), and chlorin p6 (Figure 1.5F) were optimized with B3LYP, and ωB97X was used for the excited singlet state calculations. Triplet states were optimized with B3LYP, M06, PBE0, ωB97, ωB97X, and ωB97XD.

In the calculations of modified chlorin derivatives (Paper VI), B3LYP was used in geometry optimizations and ωB97X for vertical singlet excitations. Vertical triplet excitations were calculated using B3LYP and PBE0. In paper V and VI, the 6-311G(2d,2p) basis set was used throughout the calculations and solvation in THF was modelled by a conductor-like implementation of PCM.[344-346]

The calculated wavelengths are plotted against the oscillator strengths using a Gaussian line shape.

6.2. Can range-separated and hybrid DFT functionals predict low-lying excitations? A Tookad case study (Paper III)

Tookad is a promising photosensitizer with potential application in treatment of prostate cancer.[212-215] This compound holds effective photodynamic properties, such as strong absorption at wavelengths longer than a majority of other photosensitizers, a property that makes the treatment more effective due to increased light penetration depth into tissues.

The two lowest-lying absorption bands of Tookad and BPheid calculated in toluene and THF using the B3LYP, M06HF and ωB97XD functionals on B3LYP and M06 geometries are displayed in Table 6.1 and Table 6.2. Excited state calculations using the same functional on either the B3LYP or M06 geometry generates highly similar absorption wavelengths, indicating that the functional used in geometry optimization is not crucial. The functional used in excited state calculations does, on the other hand, play a more significant role. B3LYP overall generates the Q_y band (the red-most absorption band) at shorter wavelengths than M06HF and ωB97XD. Overestimation of excitation energies is a well-known problem of B3LYP. This functional in general overestimates excitation energies by ~0.1-0.2 eV, consistent with the errors of 0.15-0.19 eV found for the first excitation band of Tookad and BPheid.

For M06HF and ωB97XD the excitation energies are closer to the experimental values than for B3LYP, with errors in the range of 0-0.15 eV for M06HF and 0-0.05 eV for ωB97XD. For these two functionals the excitation energies are in some cases underestimated and in other cases overestimated with respect to the experimental data. ωB97XD overall generates absorption wavelengths closest to the experimental Q_y band for Tookad. For BPheid, ωB97XD generates the best result for the Q_y band in three cases out of four. However, in the fourth case M06HF and ωB97XD are almost equally close to the experimental value. M06HF is almost as accurate as ωB97XD in several cases, whereas in others the data for this functional deviate significantly more.

Table 6.1. Calculated low-lying absorption bands (nm) for Tookad in toluene and THF.

		Solvent = Toluene		*Solvent = THF*	
Opt	*TD-DFT*	Q_y	Q_x	Q_y	Q_x
B3LYP	B3LYP	695	528	693	530
B3LYP	M06HF	810	523	743	521
B3LYP	ωB97XD	769	528	750	527
M06	B3LYP	690	524	688	526
M06	M06HF	805	519	745	517
M06	ωB97XD	763	523	746	522
Exp		762[a]	535[a]	755[b]	529[b]

[a] Measured in toluene.[347] [b] Measured in THF.[348]

Table 6.2. Calculated low-lying absorption bands (nm) for BPheid in toluene and THF.

		Solvent = Toluene		*Solvent = THF*	
Opt	*TD-DFT*	Q_y	Q_x	Q_y	Q_x
B3LYP	B3LYP	681	554	679	554
B3LYP	M06HF	777	530	708	524
B3LYP	ωB97XD	759	553	738	550
M06	B3LYP	679	549	678	549
M06	M06HF	760	524	689	517
M06	ωB97XD	753	547	729	544
Exp		758[a]	531[a]	751[b]	527[b]

[a] Measured in toluene.[349] [b] Measured in THF.[349]

The error of the Q_x band (the second red-most absorption band) is overall smaller than for the Q_y band. For Tookad, the position of this band is almost independent of the functional used. However for BPheid the functionals do not perform as equally as for Tookad, and M06HF is found to predict this absorption peak more accurately than B3LYP and ωB97XD.

The different solvents were shown only to affect the Q_y band by a few nm for B3LYP and ωB97XD, whereas for M06HF the difference between the two

solvents is significantly larger. Compared with gas-phase data it was clear that inclusion of implicit solvent is often required in order to obtain reasonable excitation energies.

For the Tookad and BPheid geometries optimized using B3LYP, vertical singlet excitation energies in toluene were also calculated using the CAM-B3LYP, M06, M062X, ωB97, ωB97X, LC-ωPBE, and PBE0 functionals for comparison. The spectra calculated with these functionals together with data for B3LYP, M06HF and ωB97XD are displayed in Figure 6.1 and Figure 6.2 for Tookad and BPheid, respectively. The spectra display significant differences in the performance of the functionals, in particular for the low-lying excitations. For both Tookad and BPheid, ωB97XD is still the functional that displays the best positioned Q_y peak. CAM-B3LYP was found to perform best after ωB97XD, with only slightly overestimated excitation energies. CAM-B3LYP has also in studies of structurally related compounds shown to perform better than B3LYP in predicting low-lying excitation energies.[350, 351] Overall LC-ωPBE and ωB97 significantly underestimate the excitation energies, whereas the opposite was observed for B3LYP and PBE0 that significantly overestimate the excitation energies.

The overall spectra of Tookad and BPheid clearly show that the Q_y peak is the strongest one, a feature that is advantageous for photosensitizers used in PDT as lower light and drug doses are required. The Q_x peak is significantly weaker than the Q_y peak and the functionals perform more equally for this peak, in particular for Tookad. For the higher-lying excitations for Tookad, all functionals but B3LYP show two peaks, consistent with experimental data, whereas B3LYP shows an additional peak for which there is no experimental match. B3LYP, however, reproduces the two experimental peaks the best, whereas the other functionals show blue-shifted absorption in this region.

Comparing the overall spectra of Tookad and BPheid, it is clear that they are highly similar, with the absorption bands generated by the various functionals at almost the same wavelengths. However, the oscillator strength for Tookad is overall lower than for BPheid. This is partly supported by experimental data

that show a lower extinction coefficient for the higher energy bands of Pd-BChl compared to the metal-free counterpart, albeit a higher extinction coefficient for the red-most absorption band.[352]

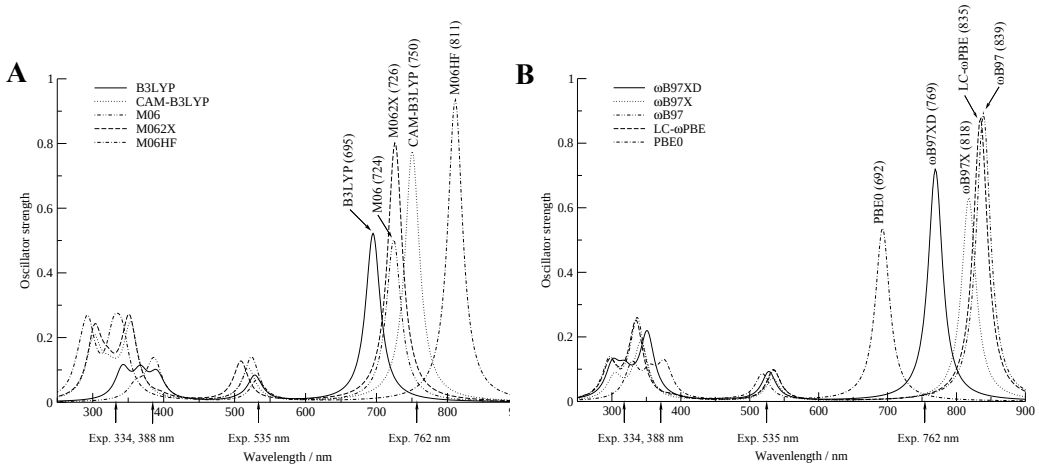

Figure 6.1. Absorption spectra of Tookad generated by (A) the B3LYP and M06 functional series and (B) the PBE and ωB97 functional series. Experimental values are displayed along the x axis. Reproduced by permission of the American Chemical Society. http://pubs.acs.org/doi/abs/10.1021/ct100148h

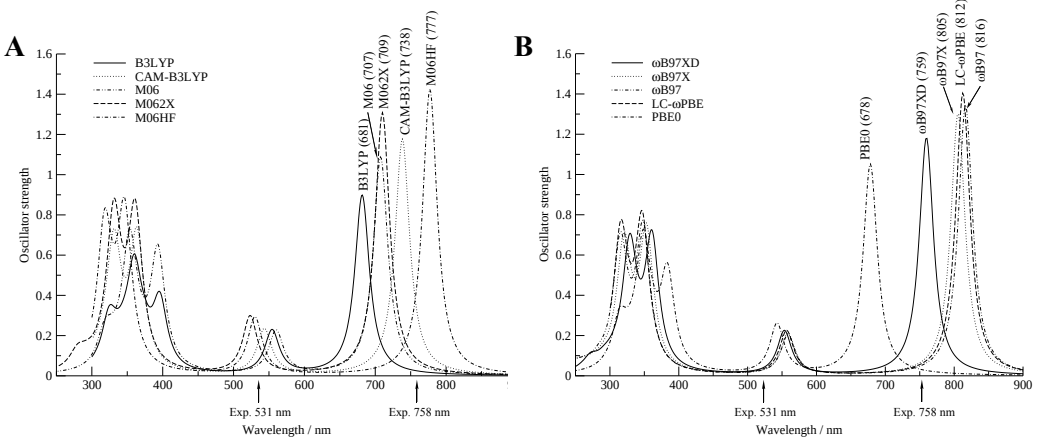

Figure 6.2. Absorption spectra of BPheid generated by (A) the B3LYP and M06 functional series and (B) the PBE and ωB97 functional series. Experimental values are displayed along the x axis. Reproduced by permission of the American Chemical Society. http://pubs.acs.org/doi/abs/10.1021/ct100148h

The effect of the basis set on the calculated absorption spectra was investigated among the 6-31G(d,p), 6-31+G(d,p) and 6-311+G(2d,2p) basis sets, but no large differences were found. The inclusion of diffuse functions, however, generated slightly better results. This conclusion was also confirmed by previous studies.[353, 354]

Table 6.3 shows the electron density differences between the ground state and the four lowest-lying excited states, corresponding to the peaks displayed in the spectra, of Tookad calculated with ωB97XD on the B3LYP geometry.

Table 6.3. Electron density differences between the ground and excited states of Tookad generated using the ωB97XD functional.

Excited state	*Excitation energy (eV)*	*Wavelength (nm)*	*Oscillator strength*	*Electron density difference between the ground state and excited state*
1	1.61	769	0.54	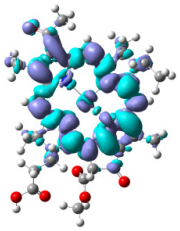
2	2.35	528	0.14	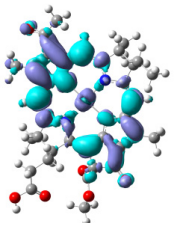
9	3.54	351	0.72	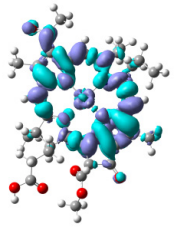
13	3.90	318	0.17	

Blue colour represents a decrease in electron density and purple an increase in electron density of the excited state compared to the ground state. The plots show that there are no dramatic restructuring in the electron distributions upon excitation, but mainly they involve pure $\pi \rightarrow \pi^*$ excitations within the aromatic macrocycle. Small changes in the metal d-orbitals are however observed during the excitations, but only the fourth excitation involves considerable interaction between the aromatic core and the metal.

The presented data show that ωB97XD is the most suitable functional to use in the study of low-lying excitations of Tookad and BPheid. However, it is important to stress that the study was conducted on a limited system and that the performance of the functionals can be system dependent.

The present study is followed by further benchmarking of the long-range corrected ωB97 functionals in predicting spectroscopic properties of porphyrin and chlorin based compounds in order to obtain further evidence for the performance of these functionals on a larger set of compounds.

6.3. Predictive power of long-range corrected functionals on the spectroscopic properties of tetrapyrrole derivatives for PDT (Paper V)

In order to follow up the study of Tookad and BPheid, the long-range corrected ωB97, ωB97X, and ωB97XD functionals were included in a study of low-lying excitations of a set of the structurally related compounds protoporphyrin IX, phytoporphyrin, Foscan, chlorin e6, and chlorin p6, along with unsubstituted porphyrin and chlorin.

In Figure 6.3A and Figure 6.3B two examples of calculated absorption spectra are shown. In Figure 6.3A, the calculated absorption spectra of chlorin with the functionals B3LYP, ωB97XD, and M06 used in geometry optimizations and ωB97X for excited state calculations are displayed, and in Figure 6.3B the absorption spectra of chlorin using the B3LYP geometry and ωB97, ωB97X, and ωB97XD in excited state calculations are displayed. The calculated wavelengths of the red-most absorption peak for chlorin, porphyrin, protoporphyrin IX and phytoporphyrin are displayed in Table 6.4 and Table 6.5.

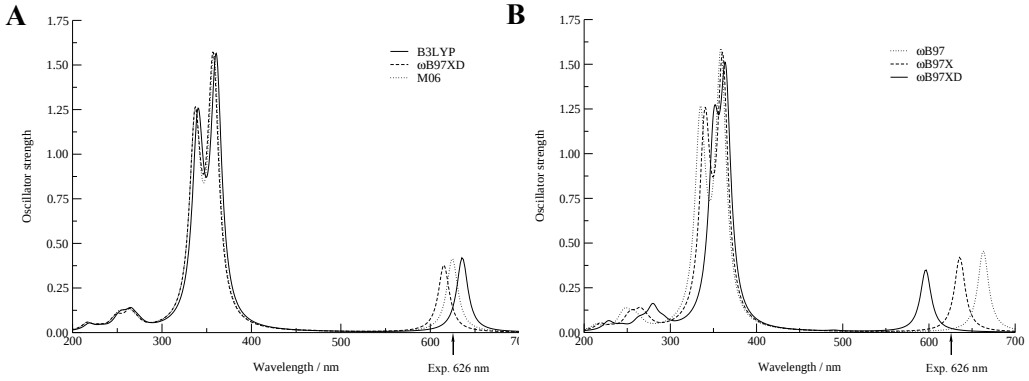

Figure 6.3. Absorption spectra of chlorin obtained using (A) ωB97X on the three different optimized chlorin geometries; (B) three different functionals on the B3LYP optimized geometry. Reproduced by permission of the PCCP Owner Societies. http://pubs.rsc.org/en/content/articlelanding/2011/CP/C0CP02792H

The data for chlorin, porphyrin and protoporphyrin IX show that the B3LYP geometry overall generates the red-most absorption peak at longest wavelength

and that the ωB97XD geometry generates the shortest wavelength, as is also seen in Figure 6.3. However, the functional used in geometry optimization is not as crucial for the resulting absorption spectra as the functional used in excited state calculations, clearly seen when comparing Figure 6.3A and Figure 6.3B. It is clear that the functionals used in excited state calculations display larger differences in their performance of reproducing the red-most absorption peak. This was also concluded in the study of Tookad and BPheid (Paper III).

The functional used in the excited state calculations that generates the red-most absorption peak closest to the experimental wavelength for chlorin, porphyrin and protoporphyrin IX is in most cases ωB97X. This absorption peak is located at either slightly shorter or longer wavelength with respect to the experimental peak, depending on the compound under study and the functional used in the geometry optimization. However, ωB97 generates the absorption peak closer to the experimental one for protoporphyrin IX optimized with ωB97XD, and ωB97 generates the red-most absorption peak equally close to the experimental one as ωB97X for chlorin optimized with ωB97XD, albeit at longer wavelength.

The ωB97X functional clearly generates overall smallest errors. The combination of B3LYP used in geometry optimization and ωB97X in excited state calculations overall generates the red-most absorption at longer wavelength than the experimental peak, with an error for chlorin, porphyrin and protoporphyrin IX in the range of 0.02-0.04 eV. ωB97X used in excited state calculations on either the ωB97XD or M06 geometry generates the red-most absorption peak at either shorter or longer wavelengths compared to the experimental peak depending on the compound. The combination of ωB97XD in geometry optimization and ωB97X in excited state calculations generates errors in the range of 0.01-0.09 eV, and the combination of M06 in geometry optimization and ωB97X in excited state calculations generates errors in the range of 0-0.02 eV. The errors were obtained by comparing the calculated data in THF with experimental data generated in benzene for chlorin and porphyrin, and in THF for protoporphyrin IX. The errors calculated with ωB97X for

chlorin and porphyrin are in the same range as those obtained with DFT/CIS[265] and DFT/MRCI[266] for the same compounds. The errors are significantly smaller than the ones obtained with large CASPT2 calculations of porphyrin.[355]

The difference between protonated and deprotonated protoporphyrin IX and phytoporphyrin was minor in most case. Hence, data for deprotonated species are not displayed. The errors listed above, however, consider data for both protonated and deprotonated protoporphyrin IX.

For the two functionals that do not generate as accurate results as ωB97X in predicting the position of the red-most absorption peak, it is clear that ωB97XD overall generates the absorption peak at too short wavelength whereas ωB97 on the other hand in most cases generates the absorption peak at too long wavelength. It is hence clear that ωB97XD overestimates the excitation energy and ωB97 underestimates the excitation energy.

Table 6.4. Red-most absorption wavelengths (nm), excitation energies (in parenthesis; eV) and oscillator strengths (*f*) of chlorin and porphyrin obtained using various combinations of functionals in geometry optimization and excited state calculations.

		Chlorin		*Porphyrin*	
Opt	*TD-DFT*	*Wavelength, E*	*f*	*Wavelength, E*	*f*
B3LYP	ωB97XD	596 (2.08)	0.154	584 (2.12)	0.001
B3LYP	ωB97X	636 (1.95)	0.147	631 (1.96)	0.004
B3LYP	ωB97	663 (1.87)	0.144	668 (1.86)	0.006
ωB97XD	ωB97XD	582 (2.13)	0.146	576 (2.15)	0.002
ωB97XD	ωB97X	615 (2.02)	0.139	621 (2.00)	0.005
ωB97XD	ωB97	637 (1.95)	0.135	656 (1.89)	0.008
M06	ωB97XD	588 (2.11)	0.155	576 (2.15)	0.001
M06	ωB97X	625 (1.99)	0.148	621 (2.00)	0.003
M06	ωB97	649 (1.91)	0.144	655 (1.89)	0.005
Exp		626[a] (1.98)	-	613[b] (2.02) 617[c] (2.01)	-

[a] Measured in benzene.[190] [b] Measured in ethanol.[189] [c] Measured in benzene.[189]

Table 6.5. Red-most absorption wavelengths (nm), excitation energies (in parenthesis; eV) and oscillator strengths (*f*) of protoporphyrin IX and phytoporphyrin obtained using various combinations of functionals in geometry optimization and excited state calculations.

		Protoporphyrin IX		*Phytoporphyrin*	
Opt	*TD-DFT*	*Wavelength, E*	*f*	*Wavelength, E*	*f*
B3LYP	ωB97XD	599 (2.07)	0.022	587 (2.11)	0.032
B3LYP	ωB97X	643 (1.93)	0.029	599 (2.07)	0.039
B3LYP	ωB97	674 (1.84)	0.034	598 (2.07)	0.046
ωB97XD	ωB97XD	582 (2.13)	0.027	527 (2.35)	0.030
ωB97XD	ωB97X	613 (2.02)	0.036	529 (2.35)	0.007
ωB97XD	ωB97	629 (1.97)	0.043	528 (2.35)	0.006
M06	ωB97XD	591 (2.10)	0.023	576 (2.15)	0.031
M06	ωB97X	632 (1.96)	0.030	584 (2.12)	0.039
M06	ωB97	660 (1.88)	0.035	583 (2.13)	0.045
Exp		633[a] (1.96)	-	580[b] (2.14) 638[c] (1.94)	-

[a] Measured in THF.[356] [b] Measured in DMSO.[357] [c] Measured in ethyl ether-acetic acid.[204]

The finding that ωB97X generates the most accurate absorption spectra is supported by a study of potent organic dyes for solar cells, in which it was found that ωB97X generates more accurate absorption spectra than ωB97.[358] However, these results contradict the conclusion from the study of Tookad and BPheid where it was found that ωB97XD was the most accurate functional in this family. A benchmarking study of the ωB97 functional family also concluded that ωB97XD generates smallest errors.[271] The overall errors calculated with the three ωB97 functionals for chlorin and porphyrin are, however, smaller than previously calculated with other well-established functionals, such as BLYP, B3LYP, and PBE0.[359, 360]

For phytoporphyrin (Table 6.5), the calculated absorption data are harder to interpret than for chlorin, porphyrin and protoporphyrin IX for which the

behaviour of the functionals was fairly similar. For phytoporphyrin, the data diverges from the pattern observed for the other compounds and it is clear that in most cases the functional used in geometry optimization has a larger influence on the red-most absorption than the functional used in excited state calculations. The sparse experimental data available for phytoporphyrin and the large difference in the experimental peaks in the two solvents (580[357] vs 638[204] nm) makes it difficult to conclude which combination of functionals is more appropriate here. The red-most absorption peaks calculated on the B3LYP and the M06 geometries lie close to the experimental peak at 580 nm, whereas the absorption peaks generated on the ωB97XD geometry are found at too short wavelength. No match for the experimental peak at 638 nm was found.

Comparing the oscillator strengths of the four compounds, it is clearly seen that chlorin displays significantly stronger absorption than the porphyrin compounds. This property makes chlorin based compounds more promising to use in PDT.

Based on the initial benchmarking results, B3LYP was used in geometry optimizations and ωB97X in excited state calculations of Foscan, chlorin e6, and chlorin p6. Calculated red-most absorptions for these compounds are displayed in Table 6.6. ωB97X reproduces the red-most peak for Foscan only 1 nm from the experimentally measured one. For chlorin e6 and chlorin p6, the calculated wavelengths are blue-shifted compared with experiments. The errors for chlorin e6 and chlorin p6 are larger than for Foscan and also larger than the ones calculated for chlorin, porphyrin, and protoporphyrin IX at the same level.

In order to estimate the ability of a newly developed compound to generate singlet oxygen, the energy gap between the ground singlet state and the first excited triplet state is considered and gives a good measurement of the photodynamic efficiency of the compound. As the energy released from the photosensitizer when it returns to the ground singlet state from the triplet state is used to excite molecular oxygen, this energy gap is required to be at least 0.98 eV,[21] the energy that is needed to excite ground triplet state oxygen to its singlet state. The performance of different functionals in calculations of triplet

state energies is consequently important to consider in the evaluation of their computational applicability in predicting photodynamic properties. Benchmarking studies of singlet-triplet transitions of large sets of compounds have shown large variations among the functionals used.[272, 361] In order to take into account geometrical differences between the ground singlet state and the first triplet state, the molecules were optimized in each state using six functionals and energy differences between the states were calculated. The data are displayed in Table 6.7.

Table 6.6. Red-most absorption wavelengths (nm), excitation energies (in parenthesis; eV) and oscillator strengths (*f*) of Foscan, chlorin e6 and chlorin p6 compared at the TD-ωB97X//B3LYP level.

Compound	*Wavelength, E*	*f*	*Exp (nm)*
Foscan	651 (1.91)	0.139	650,[a] 652[b]
Chlorin e6	629 (1.97)	0.223	655,[c] 664[d]
Chlorin p6	635 (1.95)	0.238	659,[e] 666,[f] 667,[g] 669[h]

[a] Measured in methanol.[217] [b] Measured in fetal-bovine serum.[217] [c] Measured in phosphate-buffered saline.[228] [d] Measured in dimethylformamide.[228] [e] Measured in buffer.[229] [f] Measured in methanol.[229] [g] Measured in fetal-bovine serum.[229] [h] Measured in *n*-hexane.[229]

B3LYP, M06, and PBE0 overall generate higher triplet state energies than ωB97, ωB97X, and ωB97XD, and the triplet state energies are more consistent than the ones generated with the long-range corrected functionals. The triplet state energies for porphyrin obtained with B3LYP, M06, and PBE0 are higher than the experimental value[362] and previously calculated data,[363-365] whereas the ωB97, ωB97X, and ωB97XD triplets state energies are lower. B3LYP generates highest triplet state energies in all cases but one and ωB97 consistently generates lowest triplet state energies. The largest difference between these two functionals is found for porphyrin (0.74 eV).

All seven compounds are known to generate singlet oxygen and as all functionals generate triplet excitation energies close to or higher than 0.98 eV, this indicates that they can be used to predict reasonable triplet state energies.

Table 6.7. Energy differences (eV) between the ground singlet state and the first excited triplet state optimized with various functionals.

Compound	*B3LYP*	*M06*	*PBE0*	*ωB97XD*	*ωB97X*	*ωB97*
Chlorin	1.60	1.52	1.58	1.26	1.32	1.24
Porphyrin	1.77	1.78	1.76	1.34	1.15	1.03
Protoporphyrin IX	1.58	1.56	1.56	1.41	1.25	1.18
Phytoporphyrin	1.39	1.38	1.35	1.23	1.12	1.07
Foscan	1.39	1.34	1.35	1.17	0.98	0.92
Chlorin e6	1.26	1.27	1.25	1.09	1.00	0.99
Chlorin p6	1.26	1.24	1.25	1.10	1.01	0.98

The presented benchmarking studies performed on photosensitizing porphyrin and chlorin based compounds show that computational methodology can be used to accurately predict spectroscopic properties. Despite the lack of multi-reference treatment in TD-DFT, this method in combination with suitable functionals often performs better or comparable to more computer-demanding correlated *ab initio* methods. Overall it was found that at least one of the long-range corrected ωB97 functionals performs better in predicting low-lying excitations than conventional functionals such as B3LYP for the systems under study. However, the performance among the ωB97 functionals can clearly be system dependent. For chlorin, porphyrin and protoporphyrin IX, the ωB97X functional performs overall best, whereas for the structurally related compounds Tookad and BPheid, the ωB97XD functional is more suitable. This emphasizes the importance of initial benchmarking prior to calculations to predict properties of new compounds, as an ideal single functional that can be applied to accurately predict absorption spectra of any compound most likely is impossible to find.

6.4. Computational design of chlorin based photosensitizers with enhanced absorption properties (Paper VI)

Improved photosensitizers are desirable to develop in order to reduce side effects and make PDT treatment more effective. Based on the results from the benchmarking studies of porphyrin and chlorin based compounds (Paper III and V), one of the long-range corrected ωB97 functionals that was found suitable for prediction of low-lying excitations in TD-DFT calculations of this type of systems was used to study new chlorin derivatives that can potentially be used as photosensitizers in PDT. The chlorin parent compound was used as basis for modifications as chlorin based compounds display stronger absorption at long wavelengths compared to porphyrins. Chlorin was modified with the aim to increase the conjugation and subsequently strengthen and shift the red-most absorption to longer wavelengths, thereby making the compounds suitable for application in PDT due to the beneficial properties of light at long wavelengths.

Singlet excitation energies of the newly designed compounds were calculated with TD-DFT in combination with the ωB97X functional. In the previous study of chlorin, porphyrin, and protoporphyrin IX the excitation energy calculated with this combination of functionals was underestimated by 0.02-0.04 eV (Paper V), and the error is hence expected to be in the same range for the new compounds for which no experimental data is available.

Mono-, di- and tetrasubstituted chlorin derivatives with vinyl groups (-$CH{=}CH_2$) and carboxylic acids (methanoic acid: -COOH, and propenoic acid: -CH=CH-COOH) at various positions of the chlorin molecule were studied (all positions refer to the numbering system in Figure 1.4A). These substituents are small enough to enable a large number of compounds to be studied computationally. Larger conjugated substituents such as phenyl groups are not always ideal to include in photosensitizers as these groups rarely enhance the absorption due to their position that does not contribute to the conjugation. This is observed for Foscan that possesses similar absorption as the unsubstituted chlorin despite four highly conjugated phenyl groups. Also, in order to reduce

problems related to solubility when the drug is administrated systematically, large aromatic substituents should be avoided.

Initially, one substituent (vinyl or carboxylic acid) at the time was added to four *beta* positions (2, 7, 12, and 17; cf. Figure 1.4A) and four *meso* positions (5, 10, 15, and 20; cf. Figure 1.4A) of chlorin. The calculated red-most absorptions are displayed in Table 6.8 and show that one carboxylic acid shifts the absorption more than one vinyl group. One vinyl group shifts the absorption at most 13 nm towards longer wavelengths, compared to the calculated absorption of unsubstituted chlorin, whereas one methanoic acid shifts the absorption at most 27 nm and one propenoic acid 28 nm. The position at which substitution is made often considerably affects the absorption. Even among the positions that are involved in the conjugated ring system, some positions are favourably substituted whereas some are not affected at all by substitution, or even generate blue-shifted absorption. The position at which vinyl substitution was made was not found to significantly affect the absorption. However, different positions substituted with carboxylic acids generate more diversity in the position of the red-most absorption peak. Both substitution with methanoic acid and propenoic acid at position 12 provides the largest shift in absorption.

As the carboxylic acids were able to shift the absorption more than a vinyl group, further substitution with two substituents was made with carboxylic acids only. The di-substituted compounds that generated largest red-shifted absorption are displayed in Table 6.9 and show that carboxylic acids at positions 10 and 12 shift the absorption the most, consistent with the mono-substituted derivatives where these positions are also favourable when substituted individually. The absorption was shifted at most 70 nm (10,12-methanoic acid) compared to the calculated absorption for unsubstituted chlorin. Pure methanoic acids and propenoic acids as well as one substituent of each were found to be favourable. Also the combinations of carboxylic acids at positions 2 and 12, 10 and 13, and 5 and 10 were found to be able to considerably shift the absorption, however not as much as when substitution was made at positions 10 and 12.

Table 6.8. Red-most absorption wavelengths (nm), excitation energies (in parenthesis; eV) and oscillator strengths (*f*) of modified chlorin derivatives substituted with one vinyl, methanoic acid, or propenoic acid substituent at different positions.[a]

	Vinyl		*Methanoic acid*		*Propenoic acid*	
Position	*Wavelength, E*	*f*	*Wavelength, E*	*f*	*Wavelength, E*	*f*
beta						
2	649 (1.91)	0.201	628 (1.97)	0.202	650 (1.91)	0.254
7	634 (1.96)	0.132	604 (2.05)	0.076	615 (2.02)	0.092
12	647 (1.92)	0.199	663 (1.87)	0.206	664 (1.87)	0.266
17	635 (1.95)	0.143	633 (1.96)	0.138	635 (1.95)	0.144
meso						
5	646 (1.92)	0.121	651 (1.90)	0.149	660 (1.88)	0.116
10	636 (1.95)	0.106	645 (1.92)	0.170	661 (1.87)	0.114
15	643 (1.93)	0.141	635 (1.95)	0.173	643 (1.93)	0.169
20	643 (1.93)	0.141	635 (1.95)	0.173	643 (1.93)	0.169

[a] Calculated absorption for unsubstituted chlorin at the same level of theory: 636 nm (Paper V), experimental absorption for unsubstituted chlorin in benzene: 626 nm.[190]

Table 6.9. Red-most absorption wavelengths (nm), excitations energies (eV) and oscillator strengths (*f*) of a selected set of modified chlorin derivatives substituted with two carboxylic acids.[a]

Substituents	*Wavelength*	*ΔE*	*f*
10,12-methanoic acid	706	1.76	0.212
10-propenoic acid-12-methanoic acid	697	1.78	0.175
10-methanoic acid-12-propenoic acid	691	1.80	0.241
10,12-propenoic acid	694	1.79	0.195
2,12-methanoic acid	689	1.80	0.248
10,13-methanoic acid	681	1.82	0.232
5,10-methanoic acid	679	1.83	0.146

[a] Calculated absorption for unsubstituted chlorin at the same level of theory: 636 nm (Paper V), experimental absorption for unsubstituted chlorin in benzene: 626 nm.[190]

Modelling of tetra-substituted chlorin derivatives was based on the most favourable di-substituted chlorin derivatives with carboxylic acids at positions 10 and 12. Two additional carboxylic acids were added to different positions and also two vinyl groups at different positions were added to the di-substituted compounds. A number of additional combinations not including positions 10 and 12 were also tested. However, they were not found to be as favourable as when substitution was made at positions 10 and 12. The absorption wavelengths of the derivatives that generated the largest shifts are displayed in Table 6.10 and Table 6.11.

Longest absorption wavelength was achieved for the tetra-substituted derivatives with only carboxylic acids (Table 6.10), whereas the combinations of two carboxylic acids and two vinyl groups (Table 6.11) generate overall slightly shorter absorption wavelengths, and the oscillator strengths are also overall lower.

Table 6.10. Red-most absorption wavelengths (nm), excitations energies (eV) and oscillator strengths (*f*) of the modified chlorin derivatives substituted with four carboxylic acids having the most red-shifted absorption, as well as data for substituted porphyrin and pure *meso*-substituted porphyrin.[a]

Substituents	*Wavelength*	*ΔE*	*f*
3,5,10,12-methanoic acid	747	1.66	0.226
3,10,12,15-methanoic acid	741	1.67	0.268
2,10,12,15-propenoic acid	744	1.67	0.352
3,10,12,15-propenoic acid	755	1.64	0.329
Porphyrin-3,10,12,15-propenoic acid	708	1.75	0.046
5,10,15,20-methanoic acid	679	1.83	0.189
5,10,15,20-propenoic acid	693	1.79	0.114

[a] Calculated absorption for unsubstituted chlorin at the same level of theory: 636 nm (Paper V), experimental absorption for unsubstituted chlorin in benzene: 626 nm.[190]

Table 6.11. Red-most absorption wavelengths (nm), excitations energies (eV) and oscillator strengths (*f*) of modified chlorin derivatives substituted with two carboxylic acids and two vinyl groups.[a]

Substituents	*Wavelength*	*ΔE*	*f*
2,15-vinyl-10,12-methanoic acid	735	1.69	0.261
3,15-vinyl-10,12-methanoic acid	742	1.67	0.269
2,20-vinyl-10,12-methanoic acid	735	1.69	0.258
15,20-vinyl-10,12-methanoic acid	735	1.69	0.211
2,15-vinyl-10,12-propenoic acid	734	1.69	0.263
3,15-vinyl-10,12-propenoic acid	740	1.68	0.247

[a] Calculated absorption for unsubstituted chlorin at the same level of theory: 636 nm (Paper V), experimental absorption for unsubstituted chlorin in benzene: 626 nm.[190]

Propenoic acids at positions 3, 10, 12 and 15 (Figure 6.4) were found to generate the longest wavelength, at 755 nm, which is a shift of 119 nm compared to the calculated red-most absorption wavelength for unsubstituted chlorin. Taking into account the error of the B3LYP/ωB97X combination obtained from the previous calculations of chlorin, porphyrin and protoporphyrin IX (Paper V), the experimental absorption of this derivative is expected to be in the range of 730-740 nm. The optimized geometry of chlorin-3,10,12,15-propenoic acid is displayed in Figure 6.4. Substitution with four carboxylic acids disrupts the planar geometry of the conjugated π-system. However, this out-of-plane bending has clearly no negative effect on the absorption as the most disrupted structures are found in the compounds that shift the absorption the most.

The full absorption spectra of chlorin-3,10,12,15-propenoic acid is displayed in Figure 6.5 together with the spectra for unsubstituted chlorin for comparison. Apart from the large shift in the red-most absorption and increased oscillator strength, additional features are observed for the new chlorin derivative. The second red-most absorption band for this compound, which is too low to be observed for unsubstituted chlorin, is positioned at a wavelength slightly below the red-most absorption of unsubstituted chlorin and possesses a considerable

oscillator strength. The higher-lying absorption bands are also red-shifted and the stronger one of these two peaks is positioned at shorter wavelength than the lower peak, whereas the opposite is observed for unsubstituted chlorin.

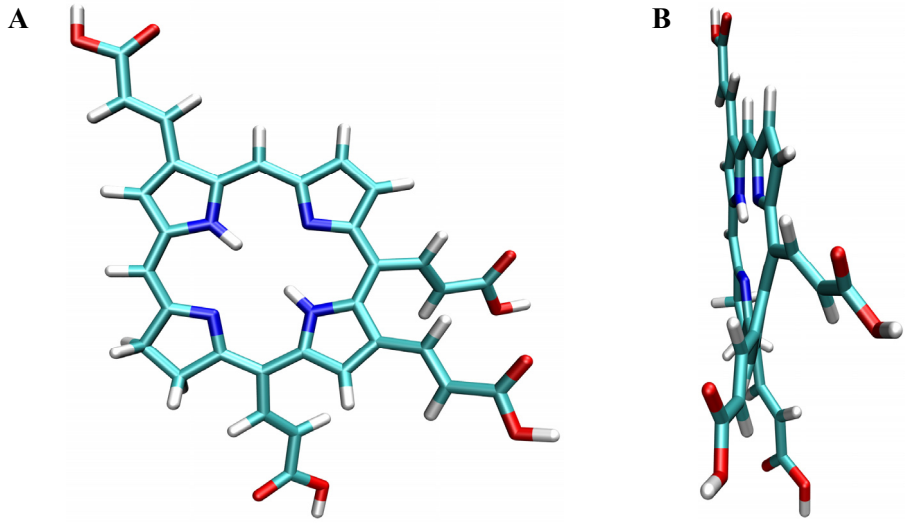

Figure 6.4. Optimized structure of chlorin-3,10,12,15-propenoic acid; (A) front view and (B) side view. Reproduced by permission of the PCCP Owner Societies. http://pubs.rsc.org/en/content/articlelanding/2011/cp/c1cp20715f

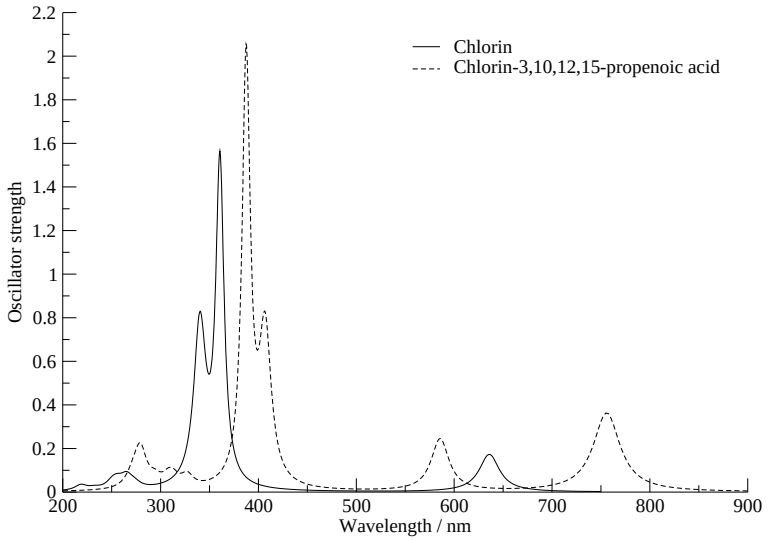

Figure 6.5. Calculated absorption spectra for unsubstituted chlorin and chlorin-3,10,12,15-propenoic acid. Reproduced by permission of the PCCP Owner Societies. http://pubs.rsc.org/en/content/articlelanding/2011/cp/c1cp20715f

The oscillator strength of the red-most absorption peak of several of the tetra-substituted chlorin derivatives is significantly increased compared to that of unsubstituted chlorin (0.147 at the same level of theory). Strong absorption of a photosensitizer in the therapeutic window for PDT requires lower light and drug doses.

For comparison, the red-most absorption of the porphyrin parent compound substituted with propenoic acids at the same four positions that generated the most red-shifted absorption with chlorin was calculated and is included in Table 6.10 (porphyrin-3,10,12,15-propenoic). This shows that the porphyrin structure is significantly less potent to exhibit absorption at long wavelength, generating the absorption of this derivative at 47 nm shorter wavelength than the corresponding chlorin derivative. The oscillator strength for the porphyrin derivative is also significantly lower than the chlorin derivative.

In Table 6.10, tetra-substituted chlorin with carboxylic acids at the four *meso*-positions, the positions that are substituted with phenyl groups in Foscan, are also displayed. The derivatives substituted at these four positions are significantly less capable of shifting the absorption compared to the most favourably substituted derivatives and their oscillator strengths are lower. However, the absorption of these derivatives is red-shifted more than when the same positions are phenolated, such as in Foscan (calculated red-most absorption wavelength for Foscan is 651 nm; Paper V).

Comparing the red-most absorption wavelengths of the most favourably substituted chlorin derivatives with the corresponding absorption of known photosensitizers such as Photofrin (red-most absorption at 630 nm[36]) and Foscan (red-most absorption at 650/652 nm[217]), the new compounds possess significantly improved absorption properties that would enable deeper light penetration into tissues. The red-most absorption of some of the new compounds is in the same range as highly promising photosensitizers such as Tookad (red-most absorption at 763 nm[205]), Lutrin (motexafin lutetium, Lu-Tex; red-most absorption at 732 nm[366]), and phthalocyanines (red-most absorption at 670-770 nm[367]).

Substitution with carboxylic acids instead of highly aromatic groups such as phenyl groups is favourable when considering solubility aspects of a compound to be used as a therapeutic agent. This is important in order to reduce the need of solubilising agents when the drug is being administrated into the blood. However, in order to diffuse through the plasma membrane of a cell, a compound is required to possess some lipophilic properties. Carboxylic acids focused on one side of the chlorin macrocycle gives the compound both hydrophilic and lipophilic properties and introduces amphiphilic character. The chlorin-3,10,12,15-propenoic acid that generated the largest shift in absorption would possess some amphiphilic character, similar to the one of chlorin e6 and chlorin p6, compounds that have been shown to possess photocytotoxic activity. The red-most absorption of these two compounds is however significantly blue-shifted as they do not contain as many groups that contribute to the conjugation as the tetra-substituted chlorin derivatives studied herein.

Calculated triplet excitation energies were used to measure the ability of the newly developed compounds to generate singlet oxygen. Vertical triplet state energies of the compounds with the most red-shifted absorption were calculated using PBE0 and B3LYP and are displayed in Table 6.12 together with the calculated absorption wavelengths. PBE0 and B3LYP are known to give consistently reliable data for triplets.[272, 361, 368]

The calculated data show that the chlorin compounds that possess promising absorption properties have triplet state energies above or close to 0.98 eV, the energy required to excite ground triplet state oxygen to its singlet state. This indicates that a majority of the compounds would likely be able to generate singlet oxygen. The highest triplet state energy was found for chlorin substituted with methanoic acids at positions 3, 5, 10 and 12. This compound obviously has both a favourable red-shifted absorption and appropriate triplet energy.

The present study shows that it is possible to achieve suitable spectroscopic properties by only a few and rather simple substituents, provided that substitution is made at favourable positions on the chlorin macrocycle. The

compounds were constructed with the aim to avoid large complex structures that possibly obstruct synthesis and administration.

Table 6.12. Triplet state energies (eV) of the compounds with the most red-shifted absorption calculated with PBE0 and B3LYP, and the corresponding singlet absorption wavelengths (nm).

		Triplet state energy	
Substituents	*Wavelength*	*PBE0*	*B3LYP*
3,5,10,12-methanoic acid	747	1.20	1.33
3,10,12,15-methanoic acid	741	1.16	1.27
2,10,12,15-propenoic acid	744	0.97	1.08
3,10,12,15-propenoic acid	755	0.92	1.05
2,15-vinyl-10,12-methanoic acid	735	1.14	1.27
3,15-vinyl-10,12-methanoic acid	742	1.10	1.21
2,20-vinyl-10,12-methanoic acid	735	1.15	1.26
15,20-vinyl-10,12-methanoic acid	735	1.09	1.22
2,15-vinyl-10,12-propenoic acid	734	1.00	1.13
3,15-vinyl-10,12-propenoic acid	740	0.98	1.11

The newly designed chlorin compounds show promising properties for being used in PDT in that they absorb light in the region of the spectra that enables deep light penetration into tissues and are capable of producing singlet oxygen. The compounds constitute useful starting points for further modifications that can improve additional properties in order to obtain appropriate photosensitizers for application in PDT.

CONCLUSIONS

Hypericin and tetrapyrrole compounds were computationally studied in the context of their potential application as photosensitizers in PDT.

Brominated hypericins have been suggested to possess more suitable properties than unsubstituted hypericin for being utilized in PDT as bromine enhances intersystem crossing to the triplet state, from which further reactions are possible. In the absence of oxygen, monobrominated hypericin was found to possibly dissociate and form a hypericin radical that is prone to react with biological molecules. This pathway constitutes an additional reaction mechanism that possibly contributes to increased production of reactive species that can initiate damage to molecular targets, even in oxygen deficient regions. Monobrominated hypericin was found to display enhanced permeation through lipid membranes compared to unsubstituted and tetrabrominated hypericin, indicating that a larger number of these molecules would have the ability to pass through the plasma membrane and reach intracellular targets. Taking this into account together with increased production of ROS and red-shifted absorption, properties that indicate enhanced and deeper therapeutic action on tumour tissue, brominated hypericins represent highly potent photosensitizers that would increase the efficiency of PDT treatment.

A possible intracellular target for hypericin after it has reached the inside of a cell is the ER Ca^{2+} ATPase SERCA that has been found to be depleted in cells treated with hypericin. Interactions with SERCA was shown to be favourable and the protein thus constitutes a highly possible intracellular target in which the hypericin molecules can be activated and radical species formed, leading to disrupted Ca^{2+} and SERCA levels and consequent cell death.

As the wavelength at which a photosensitizer absorbs determines the light penetration depth into tissues, it is one of the most important properties to consider in the design of new photosensitizers. A thorough investigation of the performance of functionals used in TD-DFT to predict absorption properties of a set of photosensitizing tetrapyrrole compounds was performed and showed

that the long-range corrected ωB97 functionals are able to generate accurate data, albeit system dependency among the functionals was found.

Second generation photosensitizers with red-shifted absorption are desirable goals in the development of more efficient PDT treatment schemes, as light at long wavelengths has the ability to penetrate deep into tissues. Potential photosensitizers with significantly red-shifted and strengthened absorption, predicted by one of the long-range corrected functionals, were designed by adding a small number of conjugating groups at favourable positions of the chlorin parent compound. The chlorin derivatives represent useful starting points for further experimental testing and additional modifications can be introduced to optimize other properties and possibly generate more ideal photosensitizers.

As computational methods in general can be used to study large numbers of compounds within a reasonable time frame, they constitute valuable tools in drug design. The studies presented in this thesis give further evidence for the advantageous application of computational tools in studies of drug compounds as they provide detailed information on hypericin and tetrapyrrole compounds that can be of great importance in the development of photosensitizers for improved cancer treatment with PDT.

ACKNOWLEDGEMENTS

I am extremely grateful to many people who have contributed, in one way or another, to make my Ph.D. studies an unforgettable time.

First of all I would like to express my gratitude to my supervisor Prof. Leif Eriksson for help, support and encouragement during my studies.

I am immensely grateful to Dr. Daniel dos Santos and Dr. Rita Guedes at the Department of Pharmacy, University of Lisbon, Portugal, for great supervision and valuable discussions during our collaboration.

I would like to thank Dr. Eric Patridge and all members in Sartorelli research group at Yale University School of Medicine, United States, for making my research visit extremely interesting and enjoyable.

I have been fortunate to work with great people of whom I would like to explicitly thank the former and present members and collaborators; Ane, Ann-Louise, Boxue, Chunxia, Dragan, Edvin, Ismael, Javier, Joakim, Klefah, Li, Magnus, Min, Oles, Patricia, Salama, Samuel, Viraja, and Yaoquan.

I also wish to thank a countless number of other people at the School of Science and Technology at Örebro University and the School of Chemistry at the National University of Ireland - Galway for making my studies memorable.

I acknowledge the School of Science and Technology, the Life Science Research School, and the Modelling and Simulation Research School at Örebro University, the School of Chemistry at the National University of Ireland - Galway, and Sparbanksstiftelsen Nya for financial support.

Finally, I would like to thank my family for love and encouragement, and for constantly supporting me in everything I do.

REFERENCES

1 R. Roelandts, *J. Am. Acad. Dermatol.* **2002**, *46*, 926-30.

2 J. A. Parrish, T. B. Fitzpatrick, L. Taneubaum, M. A. Pathac, *N. Engl. J. Med.* **1974**, *291*, 1207-1211.

3 H. von Tappeiner, A. Jesionek, *Munch. Med. Wochenschr.* **1903**, *47*, 2042-2044.

4 A. Jesionek, H. von Tappeiner, *Dtsch. Arch. Klin. Med.* **1905**, *82*, 223-227.

5 F. Meyer-Betz, *Dtsch. Arch. Klin. Med.* **1913**, *112*, 476-503.

6 I. Diamond, A. F. McDonagh, C. B. Wilson, S. G. Granelli, S. Nielsen, R. Jaenicke, *Lancet* **1972**, *300*, 1175-1177.

7 T. J. Dougherty, G. B. Grindey, R. Fiel, K. R. Weishaupt, D. G. Boyle, *J. Natl. Cancer Inst.* **1975**, *55*, 115-121.

8 J. F. Kelly, M. E. Snell, M. C. Berenbaum, *Br. J. Cancer* **1975**, *31*, 237-244.

9 J. F. Kelly, M. E. Snell, *J. Urol.* **1976**, *115*, 150-151.

10 T. J. Dougherty, J. E. Kaufman, A. Goldfarb, K. R. Weishaupt, D. G. Boyle, A. Mittleman, *Cancer Res.* **1978**, *38*, 2628-2635.

11 Y. K. Tandon, M. F. Yang, E. D. Baron, *Photodermatol. Photoimmunol. Photomed.* **2008**, *24*, 222-230.

12 F. H. Sakamoto, J. D. Lopes, R. R. Anderson, *J. Am. Acad. Dermatol.* **2010**, *63*, 183-193.

13 A. F. Cruess, G. Zlateva, A. M. Pleil, B. Wirostko, *Acta Ophthalmol.* **2009**, *87*, 118-132.

14 M. B. Ericson, A.-M. Wennberg, O. Larkö, *Ther. Clin. Risk Manag.* **2008**, *4*, 1-9.

15 E. Ben-Hur, A. C. E. Moor, H. Margolis-Nunno, P. Gottlieb, M. M. Zuk, S. Lustigman, B. Horowitz, A. Brand, J. van Steveninck, T. M. Dubbelman, *Transfus. Med. Rev.* **1996**, *10*, 15-22.

16 M. Wainwright, *J. Antimicrob. Chemother.* **1998**, *42*, 13-28.

17 K. O'Riordan, O. E. Akilov, T. Hasan, *Photodiagnosis Photodyn. Ther.* **2005**, *2*, 247-262.

18 M. C. DeRosa, R. J. Crutchley, *Coord. Chem. Rev.* **2002**, *233*, 351-371.

19 J. A. Parrish, F. Anderson, D. Urbach, *UV-A: Biological effects of ultraviolet radiation with emphasis on human responses to longwave ultraviolet*. Plenum Press, New York, **1978**.

20 L. O. Svaasand, R. Ellingsen, *Photochem. Photobiol.* **1983**, *38*, 293-299.

21 L. Herzberg, G. Herzberg, *Astrophys. J.* **1947**, *105*, 353-359.

22 J. Moan, K. Berg, *Photochem. Photobiol.* **1991**, *53*, 549-553.

23 K. Plaetzer, T. Kiesslich, B. Krammer, P. Hammerl, *Photochem. Photobiol. Sci.* **2002**, *1*, 172-177.

24 N. L. Oleinick, R. L. Morris, T. Belichenko, *Photochem. Photobiol. Sci.* **2002**, *1*, 1-21.

25 Y. K. Ho, R. G. Smith, M. S. Brown, J. L. Goldstein, *Blood* **1978**, *52*, 1099-1114.

26 S. Vitols, G. Gahrton, A. Ost, C. Peterson, *Blood* **1984**, *63*, 1186-1193.

27 S. G. T. Smith, J. Bedwell, A. J. Macrobert, M. H. Griffiths, S. G. Bown, M. R. Hetzel, *Thorax* **1993**, *48*, 474-480.

28 D. Yova, V. Hovhannisyan, T. Theodossiou, *J. Biomed. Optics* **2001**, *6*, 52-57.

29 M. A. Elfar, N. R. Pimstone, *Cell Biochem. Func.* **1985**, *3*, 115-119.

30 J. L. Wike-Hooley, J. Haveman, H. S. Reinhold, *Radiother. Oncol.* **1984**, *2*, 343-366.

31 I. F. Tannock, D. Rotin, *Cancer Res.* **1989**, *49*, 4373-4384.

32 J. Moan, Q. Peng, J. F. Evensen, K. Berg, A. Western, C. Rimington, *Photochem. Photobiol.* **1987**, *46*, 713-721.

33 Y. N. Konan, R. Gurny, E. Allemann, *J. Photochem. Photobiol. B Biol.* **2002**, *66*, 89-106.

34 T. J. Dougherty, W. R. Potter, K. R. Weishaupt, *Prog. Clin. Biol. Res.* **1984**, *170*, 301-314.

35 C. J. Byrne, L. V. Marshallsay, A. D. Ward, *J. Photochem. Photobiol. B Biol.* **1990**, *6*, 13-27.

36 T. J. Dougherty, C. J. Gomer, B. W. Henderson, G. Jori, D. Kessel, M. Korbelik, J. Moan, Q. Peng, *J. Natl. Cancer Inst.* **1998**, *90*, 889-905.

37 H. Falk, *Angew. Chem. Int. Ed.* **1999**, *38*, 3117-3136.

38 K. Linde, C. D. Mulrow, M. Berner, M. Egger, *Cochrane Database of Systematic Reviews* **2005**, 73.

39 N. Pace, *Am. J. Physiol.* **1942**, *136*, 650-656.

40 A. C. Giese, *Photochem. Photobiol. Rev.* **1980**, *5*, 229-255.

41 O. S. Araya, E. J. H. Ford, *J. Comp. Pathol.* **1981**, *91*, 135-141.

42 C. Cerny, *Hoppe-Seyler's Z. Phys. Chem.* **1911**, *73*, 371-382.

43 H. Brockmann, F. Pohl, K. Maier, M. N. Haschad, *Justus Liebigs Ann. Chem.* **1942**, *553*, 1-52.

44 H. Brockmann, E. H. Falkenhausen, A. Dorlares, *Naturwissenschaften* **1950**, *37*, 540.

45 H. Falk, W. Schmitzberger, *Monatsh. Chem.* **1992**, *123*, 731-739.

46 H. Brockmann, F. Kluge, H. Muxfeldt, *Chem. Ber.* **1957**, *90*, 2302-2318.

47 H. Falk, J. Meyer, M. Oberreiter, *Monatsh. Chem.* **1993**, *124*, 339-341.

48 H. Falk, G. Schoppel, *Monatsh. Chem.* **1991**, *122*, 739-744.

49 H. J. Banks, D. W. Cameron, W. D. Raverty, *Aust. J. Chem.* **1976**, *29*, 1509-1521.

50 M. Gill, A. Gimenez, R. W. McKenzie, *J. Nat. Prod.* **1988**, *51*, 1251-1256.

51 J. A. Rideout, M. D. Sutherland, *Aust. J. Chem.* **1985**, *38*, 793-808.

52 F. De Riccardis, M. Iorizzi, L. Minale, R. Riccio, B. Richer de Forges, C. Debitus, *J. Org. Chem.* **1991**, *56*, 6781-6787.

53 P. A. Cohen, G. H. N. Towers, *J. Nat. Prod.* **1995**, *58*, 520-526.

54 P. A. Cohen, G. H. N. Towers, *Phytochemistry* **1995**, *40*, 911-915.

55 H. Brockmann, H. Lackner, *Tetrahedron Lett.* **1979**, *18*, 1575-1578.

56 J. L. Wynn, T. M. Cotton, *J. Phys. Chem.* **1995**, *99*, 4317-4323.

57 S. M. Arabei, J. P. Galaup, P. Jardon, *Chem. Phys. Lett.* **1997**, *270*, 31-36.

58 R. C. Guedes, L. A. Eriksson, *J. Photochem. Photobiol. Chem.* **2005**, *172*, 293-299.

59 C. S. Foote, *Photochem. Photobiol.* **1991**, *54*, 659-659.

60 Z. J. Diwu, J. W. Lown, *Free Radic. Biol. Med.* **1993**, *14*, 209-215.

61 S. Rahimipour, C. Palivan, D. Freeman, F. Barbosa, M. Fridkin, L. Weiner, Y. Mazur, G. Gescheidt, *Photochem. Photobiol.* **2001**, *74*, 149-156.

62 J. Malkin, Y. Mazur, *Photochem. Photobiol.* **1993**, *57*, 929-933.

63 L. Burel, P. Jardon, J. C. Lepretre, *New J. Chem.* **1997**, *21*, 399-403.

64 S. M. Ali, S. K. Chee, G. Y. Yuen, M. Olivo, *Int. J. Mol. Med.* **2002**, *9*, 461-472.

65 P. Jardon, N. Lazortchak, R. Gautron, *J. Chim. Phys. Phys. Chim. Biol.* **1987**, *84*, 1141-1145.

66 H. Racinet, P. Jardon, R. Gautron, *J. Chim. Phys. Phys. Chim. Biol.* **1988**, *85*, 971-977.

67 A. P. Darmanyan, L. Burel, D. Eloy, P. Jardon, *J. Chim. Phys. Phys. Chim. Biol.* **1994**, *91*, 1774-1785.

68 H. Bouirig, D. Eloy, P. Jardon, *J. Chim. Phys. Phys. Chim. Biol.* **1992**, *89*, 1391-1411.

69 B. Ehrenberg, J. L. Anderson, C. S. Foote, *Photochem. Photobiol.* **1998**, *68*, 135-140.

70 L. Weiner, Y. Mazur, *J. Chem. Soc. Perkin Trans. 2* **1992**, 1439-1442.

71 F. Gai, M. J. Fehr, J. W. Petrich, *J. Am. Chem. Soc.* **1993**, *115*, 3384-3385.

72 F. Gai, M. J. Fehr, J. W. Petrich, *J. Phys. Chem.* **1994**, *98*, 8352-8358.

73 D. S. English, W. Zhang, G. A. Kraus, J. W. Petrich, *J. Am. Chem. Soc.* **1997**, *119*, 2980-2986.

74 D. S. English, K. Das, K. D. Ashby, J. Park, J. W. Petrich, E. W. Castner, *J. Am. Chem. Soc.* **1997**, *119*, 11585-11590.

75 R. A. Obermüller, G. J. Schutz, H. J. Gruber, H. Falk, *Monatsh. Chem.* **1999**, *130*, 275-281.

76 C. Thomas, L. Pardini, R. S. Pardini, 3rd Biennial Meeting of the International Photodynamic Association Buffalo, NY, July 17-21, **1990**.

77 P. S. Chung, C. K. Rhee, K. H. Kim, W. Paek, J. Chung, M. B. Paiva, A. A. Eshraghi, D. J. Castro, R. E. Saxton, *Laryngoscope* **2000**, *110*, 1312-1316.

78 C. S. Head, Q. Luu, J. Sercarz, R. Saxton, *World J. Surg. Oncol.* **2006**, *4*, 87.

79 C. D. Liu, D. Kwan, R. E. Saxton, D. W. McFadden, *J. Surg. Res.* **2000**, *93*, 137-143.

80 M. Alecu, C. Ursaciuc, F. Halalau, G. Coman, W. Merlevede, E. Waelkens, P. de Witte, *Anticancer Res.* **1998**, *18*, 4651-4654.

81 C. Thomas, R. S. Pardini, *Photochem. Photobiol.* **1992**, *55*, 831-837.

82 A. Andreoni, A. Colasanti, P. Colasanti, M. Mastrocinque, P. Riccio, G. Roberti, *Photochem. Photobiol.* **1994**, *59*, 529-533.

83 Q. M. van der Werf, R. E. Saxton, A. Chang, D. Horton, M. B. Paiva, J. Anderson, C. Foote, J. Soudant, A. Mathey, D. J. Castro, *Laryngoscope* **1996**, *106*, 479-483.

84 A. R. Kamuhabwa, P. M. Agostinis, M. A. D'Hallewin, L. Baert, P. A. de Witte, *Photochem. Photobiol.* **2001**, *74*, 126-32.

85 E. M. Delaey, R. Obermuëller, I. Zupko, D. De Vos, H. Falk, P. A. M. de Witte, *Photochem. Photobiol.* **2001**, *74*, 164-171.

86 G. Seitz, S. W. Warmann, S. Armeanu, H. Heitmann, P. Ruck, R. M. Hoffman, J. Fuchs, J. T. Wessels, *Int. J. Oncol.* **2007**, *30*, 615-20.

87 G. Seitz, R. Krause, J. Fuchs, H. Heitmann, S. Armeanu, P. Ruck, S. W. Warmann, *Oncol. Rep.* **2008**, *20*, 1277-82.

88 J. T. Wessels, A. C. Busse, M. Rave-Frank, S. Zanker, R. Hermann, E. Grabbe, G. A. Müller, *Photochem. Photobiol.* **2008**, *84*, 228-35.

89 V. Stupakova, L. Varinska, A. Mirossay, M. Sarissky, J. Mojzis, R. Dankovcik, P. Urdzik, A. Ostro, L. Mirossay, *Phytother. Res.* **2009**, *23*, 827-32.

90 M. A. D'Hallewin, P. A. De Witte, E. Waelkens, W. Merlevede, L. Baert, *J. Urol.* **2000**, *164*, 349-351.

91 M. A. D'Hallewin, A. R. Kamuhabwa, T. Roskams, P. A. M. De Witte, L. Baert, *BJU Int.* **2002**, *89*, 760-763.

92 M. Olivo, W. Lau, V. Manivasager, P. H. Tan, K. C. Soo, C. Cheng, *Int. J. Oncol.* **2003**, *23*, 983-990.

93 G. Lavie, F. Valentine, B. Levin, Y. Mazur, G. Gallo, D. Lavie, D. Weiner, D. Meruelo, *Proc. Ntl Acad. Sci. USA* **1989**, *86*, 5963-5967.

94 I. Lopezbazzocchi, J. B. Hudson, G. H. N. Towers, *Photochem. Photobiol.* **1991**, *54*, 95-98.

95 J. B. Hudson, I. Lopezbazzocchi, G. H. N. Towers, *Antivir. Res.* **1991**, *15*, 101-112.

96 S. Degar, A. M. Prince, D. Pascual, G. Lavie, B. Levin, Y. Mazur, D. Lavie, L. S. Ehrlich, C. Carter, D. Meruelo, *AIDS Res. Hum. Retrovir.* **1992**, *8*, 1929-1936.

97 J. B. Hudson, L. Harris, G. H. N. Towers, *Antivir. Res.* **1993**, *20*, 173-178.

98 J. Lenard, A. Rabson, R. Vanderoef, *Proc. Ntl. Acad. Sci. USA* **1993**, *90*, 158-162.

99 G. Moraleda, T. T. Wu, A. R. Jilbert, C. E. Aldrich, L. D. Condreay, S. H. Larsen, J. C. Tang, J. M. Colacino, W. S. Mason, *Antivir. Res.* **1993**, *20*, 235-247.

100 J. Tang, J. M. Colacino, S. H. Larsen, W. Spitzer, *Antivir. Res.* **1990**, *13*, 313-325.

101 D. O. Andersen, N. D. Weber, S. G. Wood, B. G. Hughes, B. K. Murray, J. A. North, *Antivir. Res.* **1991**, *16*, 185-196.

102 P. A. Cohen, J. B. Hudson, G. H. N. Towers, *Experientia* **1996**, *52*, 180-183.

103 S. Degar, G. Lavie, D. Meruelo, *Virology* **1993**, *197*, 796-800.

104 G. A. Kraus, W. J. Zhang, S. Carpenter, Y. Wannemuehler, *Bioorg. Med. Chem. Lett.* **1995**, *5*, 2633-2636.

105 D. Meruelo, G. Lavie, D. Lavie, *Proc. Ntl. Acad. Sci. USA* **1988**, *85*, 5230-5234.

106 R. F. Schinazi, C. K. Chu, J. R. Babu, B. J. Oswald, V. Saalmann, D. L. Cannon, B. F. H. Eriksson, M. Nasr, *Antivir. Res.* **1990**, *13*, 265-272.

107 N. R. Stevenson, J. Lenard, *Antivir. Res.* **1993**, *21*, 119-127.

108 C. Holden, *Science* **1991**, *254*, 522.

109 W. C. Cooper, J. James, Int. Conf. AIDS, **1990**.

110 F. T. Valentine, V. Itri, N. Kudler, R. Georgescu, Int. Conf. AIDS **1991**; Vol. 7, pp. 97.

111 A. Steinbeck-Klose, P. Wernet, Int. Conf. AIDS **1993**; Vol. 9, pp. 470.

112 R. M. Gulick, V. McAuliffe, J. Holden-Wiltse, C. Crumpacker, L. Liebes, D. S. Stein, P. Meehan, S. Hussey, J. Forcht, F. T. Valentine, *Ann. Intern. Med.* **1999**, *130*, 510-514.

113 J. M. Jacobson, L. Feinman, L. Liebes, N. Ostrow, V. Koslowski, A. Tobia, B. E. Cabana, D. H. Lee, J. Spritzler, A. M. Prince, *Antimicrob. Agents Chemother.* **2001**, *45*, 517-524.

114 S. Carpenter, M. J. Fehr, G. A. Kraus, J. W. Petrich, *Proc. Ntl Acad. Sci. USA* **1994**, *91*, 12273-12277.

115 J. Wen, P. Chowdhury, N. J. Wills, Y. Wannemuehler, J. Park, S. Kesavan, S. Carpenter, G. A. Kraus, J. W. Petrich, *Photochem. Photobiol.* **2002**, *76*, 153-157.

116 G. Lavie, Y. Mazur, D. Lavie, A. M. Prince, D. Pascual, L. Liebes, B. Levin, D. Meruelo, *Transfusion* **1995**, *35*, 392-400.

117 A. M. Prince, D. Pascual, D. Meruelo, L. Liebes, Y. Mazur, E. Dubovi, M. Mandel, G. Lavie, *Photochem. Photobiol.* **2000**, *71*, 188-195.

118 H. Falk, J. Meyer, *Monatsh. Chem.* **1994**, *125*, 753-762.

119 L. Burel, P. Jardon, *J. Chim. Phys. Phys. Chim. Biol.* **1996**, *93*, 300-316.

120 B. Chen, Y. Xu, T. Roskams, E. Delaey, P. Agostinis, J. R. Vandenheede, P. de Witte, *Int. J. Canc.* **2001**, *93*, 275-282.

121 J. C. Maziere, P. Morliere, R. Santus, *J. Photochem. Photobiol. B Biol.* **1991**, *8*, 351-360.

122 M. Korbelik, *Photochem. Photobiol.* **1993**, *57*, 846-850.

123 G. Jori, E. Reddi, *Int. J. Biochem.* **1993**, *25*, 1369-1375.

124 S. Kascakova, M. Refregiers, D. Jancura, F. Sureau, J. C. Maurizot, P. Miskovsky, *Photochem. Photobiol.* **2005**, *81*, 1395-1403.

125 P. Mukheriee, R. Adhikary, M. Halder, J. W. Petrich, P. Miskovsky, *Photochem. Photobiol.* **2008**, *84*, 706-712.

126 S. Kascakova, Z. Nadova, A. Mateasik, J. Mikes, V. Huntosova, M. Refregiers, F. Sureau, J. C. Maurizot, P. Miskovsky, D. Jancura, *Photochem. Photobiol.* **2008**, *84*, 120-7.

127 T. Peters, *Adv. Protein Chem.* **1985**, *37*, 161-245.

128 I. Sjöholm, B. Ekman, A. Kober, I. Ljungstedt-Pahlman, B. Seiving, T. Sjödin, *Mol. Pharmacol.* **1979**, *16*, 767-777.

129 M. Kohler, J. Gafert, J. Friedrich, H. Falk, J. Meyer, *J. Phys. Chem.* **1996**, *100*, 8567-8572.

130 P. Miskovsky, D. Jancura, S. Sanchez-Cortes, E. Kocisova, L. Chinsky, *J. Am. Chem. Soc.* **1998**, *120*, 6374-6379.

131 P. Miskovsky, J. Hritz, S. Sanchez-Cortes, F. Fabriciova, J. Ulicny, L. Chinsky, *Photochem. Photobiol.* **2001**, *74*, 172-183.

132 S. Vemuri, C. T. Rhodes, *Pharm. Acta Helv.* **1995**, *70*, 95-111.

133 A. S. L. Derycke, P. A. M. de Witte, *Adv. Drug Deliv. Rev.* **2004**, *56*, 17-30.

134 S. Sattler, U. Schaefer, W. Schneider, J. Hoelzl, C. M. Lehr, *J. Pharmaceut. Sci.* **1997**, *86*, 1120-1126.

135 A. Vantieghem, Z. Assefa, P. van den Abeele, W. Declercq, S. Courtois, J. R. van den Heede, W. Merlevede, P. de Witte, P. Agostinis, *FEBS Lett.* **1998**, *440*, 19-24.

136 Y. F. Ho, M. H. Wu, B. H. Cheng, Y. W. Chen, M. C. Shih, *Biochim. Biophys. Acta Biomembr.* **2009**, *1788*, 1287-1295.

137 V. Senthil, L. R. Jones, K. Senthil, L. I. Grossweiner, *Photochem. Photobiol.* **1994**, *59*, 40-47.

138 C. Hadjur, M. J. Richard, M. O. Parat, P. Jardon, A. Favier, *Photochem. Photobiol.* **1996**, *64*, 375-381.

139 R. Chaloupka, T. Obsil, J. Plasek, F. Sureau, *Biochim. Biophys. Acta Biomembr.* **1999**, *1418*, 39-47.

140 S. M. Ali, M. Olivo, *Int. J. Oncol.* **2002**, *21*, 531-540.

141 T. A. Theodossiou, A. Noronha-Dutra, J. S. Hothersall, *Int. J. Biochem. Cell Biol.* **2006**, *38*, 1946-1956.

142 L. M. Davids, B. Kleemann, D. Kacerovska, K. Pizinger, S. H. Kidson, *J. Photochem. Photobiol. B Biol.* **2008**, *91*, 67-76.

143 C. Thomas, R. S. Macgill, G. C. Miller, R. S. Pardini, *Photochem. Photobiol.* **1992**, *55*, 47-53.

144 L. Miccoli, A. Beurdeley-Thomas, G. De Pinieux, F. Sureau, S. Oudard, B. Dutrillaux, M. F. Poupon, *Cancer Res.* **1998**, *58*, 5777-5786.

145 T. A. Theodossiou, A. Papakyriakou, J. S. Hothersall, *Free Radic. Biol. Med.* **2008**, *45*, 1581-1590.

146 F. Sureau, P. Miskovsky, L. Chinsky, P. Y. Turpin, *J. Am. Chem. Soc.* **1996**, *118*, 9484-9487.

147 T. A. Theodossiou, J. S. Hothersall, P. A. De Witte, A. Pantos, P. Agostinis, *Mol. Pharm.* **2009**, *6*, 1775-1789.

148 A. Vantieghem, Y. Xu, P. van den Abeele, G. Denecker, J. R. van den Heede, W. Merlevede, P. A. de Witte, P. Agostinis, *Photochem. Photobiol.* **2001**, *74*, 133-142.

149 R. D. Almeida, B. J. Manadas, A. P. Carvalho, C. B. Duarte, *Biochim. Biophys. Acta Rev. Canc.* **2004**, *1704*, 59-86.

150 E. Buytaert, M. Dewaele, P. Agostinis, *Biochim. Biophys. Acta Rev. Canc.* **2007**, *1776*, 86-107.

151 C. M. Schempp, B. Simon-Haarhaus, C. C. Termeer, J. C. Simon, *FEBS Lett.* **2001**, *493*, 26-30.

152 S. M. Ali, S. K. Chee, G. Y. Yuen, M. Olivo, *Int. J. Mol. Med.* **2002**, *9*, 601-616.

153 S. M. Ali, S. K. Chee, G. Y. Yuen, M. Olivo, *Int. J. Mol. Med.* **2002**, *9*, 257-270.

154 K. M. Boatright, G. S. Salvesen, *Curr. Opin. Cell Biol.* **2003**, *15*, 725-731.

155 M. Holtta-Vuori, E. Ikonen, *Biochem. Soc. Trans.* **2006**, *34*, 392-394.

156 A. L. Vandenbogaerde, E. M. Delaey, A. M. Vantieghem, B. E. Himpens, W. J. Merlevede, P. A. de Witte, *Photochem. Photobiol.* **1998**, *67*, 119-125.

157 A. B. Uzdensky, L. W. Ma, V. Iani, G. O. Hjortland, H. B. Steen, J. Moan, *Laser Med. Sci.* **2001**, *16*, 276-283.

158 E. Buytaert, G. Callewaert, N. Hendrickx, L. Scorrano, D. Hartmann, L. Missiaen, J. R. Vandenheede, I. Heirman, J. Grooten, P. Agostinis, *Faseb J.* **2006**, *20*, 756-758.

159 D. Ron, P. Walter, *Nat. Rev. Mol. Cell Biol.* **2007**, *8*, 519-529.

160 E. Buytaert, J. Y. Matroule, S. Durinck, P. Close, S. Kocanova, J. R. Vandenheede, P. A. Witte, J. Piette, P. Agostinis, *Oncogene* **2008**, *27*, 1916-1929.

161 E. Buytaert, G. Callewaert, J. R. Vandenheede, P. Agostinis, *Autophagy* **2006**, *2*, 238-240.

162 P. Miskovsky, F. Sureau, L. Chinsky, P. Y. Turpin, *Photochem. Photobiol.* **1995**, *62*, 546-549.

163 D. S. English, R. T. Doyle, J. W. Petrich, P. G. Haydon, *Photochem. Photobiol.* **1999**, *69*, 301-305.

164 P. Miskovsky, L. Chinsky, G. V. Wheeler, P. Y. Turpin, *J. Biomol. Struct. Dynam.* **1995**, *13*, 547-552.

165 S. Sánchez-Cortés, P. Miskovsky, D. Jancura, A. Bertoluzza, *J. Phys. Chem.* **1996**, *100*, 1938-1944.

166 E. Kocisova, L. Chinsky, P. Miskovsky, *J. Biomol. Struct. Dynam.* **1998**, *15*, 1147-1154.

167 E. Ben-Hur, T. Fujihara, F. Suzuki, M. M. Elkind, *Photochem. Photobiol.* **1987**, *45*, 227-230.

168 F. Bordin, C. Marzano, C. Gatto, F. Carlassare, P. Rodighiero, F. Baccichetti, *J. Photochem. Photobiol. B Biol.* **1994**, *26*, 197-201.

169 J. A. Hartley, S. R. McAdam, S. Das, M. C. Roldan, M. K. Haskell, M. Lee, *Anti Canc. Drug Des.* **1994**, *9*, 181-197.

170 M. Lee, M. C. Roldan, M. K. Haskell, S. R. McAdam, J. A. Hartley, *J. Med. Chem.* **1994**, *37*, 1208-1213.

171 G. Siboni, H. Weitman, D. Freeman, Y. Mazur, Z. Malik, B. Ehrenberg, *Photochem. Photobiol. Sci.* **2002**, *1*, 483-491.

172 B. Lackner, H. Falk, *Monatsh. Chem.* **2002**, *133*, 717-721.

173 B. Lackner, Y. Popova, C. Etzlstorfer, A. A. Smelcerovic, C. W. Klampfl, H. Falk, *Monatsh. Chem.* **2005**, *136*, 777-793.

174 R. A. Obermüller, C. Etzlstorfer, H. Falk, *Monatsh. Chem.* **2002**, *133*, 89-96.

175 M. Waser, H. Falk, *Eur. J. Org. Chem.* **2006**, 1200-1206.

176 A. B. Uzdensky, D. E. Bragin, M. S. Kolosov, A. Kubin, H. G. Loew, J. Moan, *J. Photochem. Photobiol. B. Biol.* **2003**, *72*, 27-33.

177 A. Kubin, P. Meissner, F. Wierrani, U. Burner, A. Bodenteich, A. Pytel, N. Schmeller, *Photochem. Photobiol.* **2008**, *84*, 1560-3.

178 J. Zuschrader, W. Schöfberger, H. Falk, *Monatsh. Chem.* **2008**, *139*, 1387-1390.

179 I. Crnolatac, A. Huygens, A. van Aerschot, R. Busson, J. Rozenski, P. A. de Witte, *Bioorg. Med. Chem.* **2005**, *13*, 6347-53.

180 M. Roslaniec, H. Weitman, D. Freeman, Y. Mazur, B. Ehrenberg, *J. Photochem. Photobiol. B Biol.* **2000**, *57*, 149-158.

181 J. Zuschrader, G. Reiter, H. Falk, *Monatsh. Chem.* **2008**, *139*, 995-998.

182 B. Hager, W. S. L. Strauss, H. Falk, *Photochem. Photobiol.* **2009**, *85*, 1201-1206.

183 E. Delaey, I. Zupko, B. Chen, A. Derycke, F. van Laar, D. De Vos, P. De Witte, *Int. J. Oncol.* **2003**, *23*, 519-524.

184 J. B. Hudson, E. Delaey, P. A. M. de Witte, *Photochem. Photobiol.* **1999**, *70*, 820-822.

185 R. C. Guedes, L. A. Eriksson, *J. Photochem. Photobiol. Chem.* **2006**, *178*, 41-49.

186 H. Falk, W. Schmitzberger, *Monatsh. Chem.* **1993**, *124*, 77-81.

187 S. Aigner, H. Falk, *Monatsh. Chem.* **2008**, *139*, 1513-1518.

188 X. Y. Schneider-Yin, A. Kurmanaviciene, M. Roth, M. Roos, A. Fedier, E. I. Minder, H. Walt, *Photodiagnosis Photodyn. Ther.* **2009**, *6*, 12-18.

189 L. Edwards, D. H. Dolphin, M. Gouterman, A. D. Adler, *J. Mol. Spectrosc.* **1971**, *38*, 16-32.

190 U. Nagashima, T. Takada, K. Ohno, *J. Chem. Phys.* **1986**, *85*, 4524-4529.

191 N. Fotinos, M. A. Campo, F. Popowycz, R. Gurny, N. Lange, *Photochem. Photobiol.* **2006**, *82*, 994-1015.

192 R. M. Szeimies, P. Calzavara-Pinton, S. Karrer, B. Ortel, M. Landthaler, *J. Photochem. Photobiol. B Biol.* **1995**, *36*, 213-219.

193 J. C. Kennedy, R. H. Pottier, D. C. Pross, *J. Photochem. Photobiol. B Biol.* **1990**, *6*, 143-148.

194 R. van Hillegersberg, J. W. O. van den Berg, W. J. Kort, O. T. Terpstra, J. H. P. Woilson, *Gastroenterology* **1992**, *103*.

195 R. M. Szeimies, S. Karrer, S. Radakovic-Fijan, A. Tanew, P. G. Calzavara-Pinton, C. Zane, A. Sidoroff, M. Hempel, J. Ulrich, T. Proebstle, H. Meffert, M. Mulder, D. Salomon, H. C. Dittmar, J. W. Bauer, K. Kernland, L. Braathen, *J. Am. Acad. Dermatol.* **2002**, *47*, 258-62.

196 D. M. Pariser, N. J. Lowe, D. M. Stewart, M. T. Jarratt, A. W. Lucky, R. J. Pariser, P. S. Yamauchi, *J. Am. Acad. Dermatol.* **2003**, *48*, 227-32.

197 A. M. Soler, T. Warloe, A. Berner, K. E. Giercksky, *Br. J. Dermatol.* **2001**, *145*, 467-71.

198 M. Horn, P. Wolf, H. C. Wulf, T. Warloe, C. Fritsch, L. E. Rhodes, R. Kaufmann, M. De Rie, F. J. Legat, I. M. Stender, A. M. Soler, A. M. Wennberg, G. A. Wong, O. Larko, *Br. J. Dermatol.* **2003**, *149*, 1242-9.

199 L. E. Rhodes, M. de Rie, Y. Enstrom, R. Groves, T. Morken, V. Goulden, G. A. Wong, J. J. Grob, S. Varma, P. Wolf, *Arch. Dermatol.* **2004**, *140*, 17-23.

200 C. Vinciullo, T. Elliott, D. Francis, K. Gebauer, L. Spelman, R. Nguyen, W. Weightman, A. Sheridan, C. Reid, D. Czarnecki, D. Murrell, *Br. J. Dermatol.* **2005**, *152*, 765-72.

201 N. Lange, P. Jichlinski, M. Zellweger, M. Forrer, A. Marti, L. Guillou, P. Kucera, G. Wagnieres, H. van den Bergh, *Br. J. Cancer* **1999**, *80*, 185-93.

202 P. Jichlinski, L. Guillou, S. J. Karlsen, P. U. Malmström, D. Jocham, B. Brennhovd, E. Johansson, T. Gartner, N. Lange, H. van den Bergh, H. J. Leisinger, *J. Urol.* **2003**, *170*, 226-9.

203 J. Schmidbauer, F. Witjes, N. Schmeller, R. Donat, M. Susani, M. Marberger, *J. Urol.* **2004**, *171*, 135-8.

204 D. D. Perrin, *Biochem. J.* **1958**, *68*, 314-318.

205 A. Scherz, Y. Salomon, A. Brandis, H. Scheer, Palladium-substituted bacteriochlorophyll derivatives and use thereof, U. S. Patent 6,569,846, **2003**.

206 Q. Chen, Z. Huang, D. Luck, J. Beckers, P. H. Brun, B. C. Wilson, A. Scherz, Y. Salomon, F. W. Hetzel, *Photochem. Photobiol.* **2002**, *76*, 438-445.

207 S. Schreiber, S. Gross, A. Brandis, A. Harmelin, V. Rosenbach-Belkin, A. Scherz, Y. Salomon, *Int. J. Canc.* **2002**, *99*, 279-285.

208 N. V. Koudinova, J. H. Pinthus, A. Brandis, O. Brenner, P. Bendel, J. Ramon, Z. Eshhar, A. Scherz, Y. Salomon, *Int. J. Canc.* **2003**, *104*, 782-789.

209 F. Borle, A. Radu, C. Fontolliet, H. van den Bergh, P. Monnier, G. Wagnieres, *Br. J. Canc.* **2003**, *89*, 2320-2326.

210 F. Borle, A. Radu, P. Monnier, H. van den Bergh, G. Wagnieres, *Photochem. Photobiol.* **2003**, *78*, 377-383.

211 D. Preise, O. Mazor, N. Koudinova, M. Liscovitch, A. Scherz, Y. Salomon, *Neoplasia* **2003**, *5*, 475-480.

212 J. Trachtenberg, A. Bogaards, R. A. Weersink, M. A. Haider, A. Evans, S. A. McCluskey, A. Scherz, M. R. Gertner, C. Yue, S. Appu, A. Aprikian, J. Savard, B. C. Wilson, M. Elhilali, *J. Urol.* **2007**, *178*, 1974-1979.

213 M. A. Haider, S. R. H. Davidson, A. V. Kale, R. A. Weersink, A. J. Evans, A. Toi, M. R. Gertner, A. Bogaards, B. C. Wilson, J. L. Chin, M. Elhilali, J. Trachtenberg, *Radiology* **2007**, *244*, 196-204.

214 R. A. Weersink, J. Forbes, S. Bisland, J. Trachtenberg, M. Elhilali, P. H. Brun, B. C. Wilson, *Photochem. Photobiol.* **2005**, *81*, 106-113.

215 J. Trachtenberg, R. A. Weersink, S. R. H. Davidson, M. A. Haider, A. Bogaards, M. R. Gertner, A. Evans, A. Scherz, J. Savard, J. L. Chin, B. C. Wilson, M. Elhilali, *BJU Int.* **2008**, *102*, 556-562.

216 P. H. Brun, J. L. DeGroot, E. F. G. Dickson, M. Farahani, R. H. Pottier, *Photochemical & Photobiological Sciences* **2004**, *3*, 1006-1010.

217 R. Bonnett, R. D. White, U. J. Winfield, M. C. Berenbaum, *Biochem. J.* **1989**, *261*, 277-280.

218 S. Mitra, T. H. Foster, *Photochem. Photobiol.* **2005**, *81*, 849-859.

219 A. C. Kubler, J. de Carpentier, C. Hopper, A. G. Leonard, G. Putnam, *Int. J. Oral Maxillofac. Surg.* **2001**, *30*, 504-509.

220 C. Hopper, A. Kubler, H. Lewis, I. BingTan, G. Putnam, *Int. J. Cancer* **2004**, *111*, 138-146.

221 A. K. D'Cruz, M. H. Robinson, M. A. Biel, *Head Neck* **2004**, *26*, 232-240.

222 A. Zimmermann, M. Ritsch-Marte, H. Kostron, *Photochem. Photobiol.* **2001**, *74*, 611-616.

223 E. Zenkevicha, E. Saguna, V. Knyukshtoa, A. Shulgaa, A. Mironovb, O. Efremovab, R. Bonnettc, S. P. Songcac, M. Kassem, *J. Photochem. Photobiol. B Biol.* **1996**, *33*, 171-180.

224 J. M. Fernandez, M. D. Bilgin, L. I. Grossweiner, *J. Photochem. Photobiol. B* **1997**, *37*, 131-140.

225 J. K. Hoober, T. W. Sery, N. Yamamoto, *Photochem. Photobiol.* **1988**, *48*, 579-582.

226 T. Ando, K. Irie, K. Koshimizu, T. Takemuraa, H. Nishinob, A. Iwashimab, N. S., I. Sakata, *Tetrahedron* **1990**, *46*, 5921-5930.

227 G. A. Kostenich, I. N. Zhuravkin, A. V. Furmanchuk, E. A. Zhavrid, *J. Photochem. Photobiol. B Biol.* **1991**, *11*, 307-318.

228 R. Bachor, C. R. Shea, R. Gillies, T. Hasan, *Proc. Natl. Acad. Sci. USA* **1991**, *88*, 1580-1584.

229 K. Das, A. Dube, P. K. Gupta, *Dyes Pigments* **2005**, *64*, 201-205.

230 S. W. Taber, V. H. Fingar, C. T. Coots, T. J. Wieman, *Clin. Cancer Res.* **1998**, *4*, 2741-2746.

231 H. Kato, K. Furukawa, M. Sato, T. Okunaka, Y. Kusunoki, M. Kawahara, M. Fukuoka, T. Miyazawa, T. Yana, K. Matsui, T. Shiraishi, H. Horinouchi, *Lung Cancer* **2003**, *42*, 103-111.

232 A. R. Leach, *Molecular Modelling. Principles and Applications*. 2nd ed., Prentice Hall, Harlow, U.K., **2001**.

233 W. Koch, M. C. Holthausen, *A Chemist's Guide to Density Functional Theory*. 2nd ed., Wiley-VCH, Weinheim, Germany, **2001**.

234 C. J. Cramer, *Essentials of Computational Chemistry. Theories and Models.* 2nd ed., Wiley, Chichester, U.K., **2004**.

235 F. Jensen, *Introduction to Computational Chemistry*. 2nd ed., Wiley, Chichester, U.K., **2007**.

236 M. Born, J. R. Oppenheimer, *Ann. Physik* **1927**, *84*, 457-484.

237 D. H. Slater, *Phys. Rev.* **1930**, *36*, 57-64.

238 S. F. Boys, *Proc. Roy. Soc. Lond.* **1950**, *A 200*, 542-554.

239 P. J. Hay, W. R. Wadt, *J. Chem. Phys.* **1985**, *82*, 270-283.

240 W. R. Wadt, P. J. Hay, *J. Chem. Phys.* **1985**, *82*, 284-298.

241 P. J. Hay, W. R. Wadt, *J. Chem. Phys.* **1985**, *82*, 299-310.

242 P. Hohenberg, W. Kohn, *Phys. Rev.* **1964**, *136*, 864-871.

243 W. Kohn, L. J. Sham, *Phys. Rev.* **1965**, *140*, 1133-1138.

244 A. D. Becke, *Phys. Rev. A* **1988**, *38*, 3098-3100.

245 C. T. Lee, W. T. Yang, R. G. Parr, *Phys. Rev. B* **1988**, *37*, 785-789.

246 A. D. Becke, *J. Chem. Phys.* **1993**, *98*, 5648-5652.

247 C. W. Bauschlicher Jr., *Chem. Phys. Lett.* **1995**, *246*, 40-44.

248 L. A. Curtiss, P. C. Redfern, K. Raghavachari, *J. Chem. Phys.* **2005**, *123*, 124107.

249 J. Tirado-Rives, W. L. Jorgensen, *J. Chem. Theory Comput.* **2008**, *4*, 297-306.

250 C. Adamo, V. Barone, *J. Chem. Phys.* **1999**, *110*, 6158-6170.

251 Y. Zhao, D. G. Truhlar, *J. Phys. Chem.* **2006**, *110*, 5121-5129.

252 Y. Zhao, D. G. Truhlar, *J. Phys. Chem.* **2006**, *110*, 13126-13130.

253 Y. Zhao, D. G. Truhlar, *Theor. Chem. Acc.* **2008**, *120*, 215-241.

254 J. P. Perdew, K. Burke, M. Ernzerhof, *Phys. Rev. Lett.* **1996**, *77*, 3865-3 868.

255 J. P. Perdew, K. Burke, M. Ernzerhof, *Phys. Rev. Lett.* **1997**, *78*, 1396.

256 T. Yanai, D. P. Tew, N. C. Handy, *Chem. Phys. Lett.* **2004**, *393*, 51-57.

257 Y. Tawada, T. Tsuneda, S. Yanagisawa, T. Yanai, K. Hirao, *J. Chem. Phys.* **2004**, *120*, 8425-8433.

258 O. A. Vydrov, G. E. Scuseria, *J. Chem. Phys.* **2006**, *125*, 234109.

259 O. A. Vydrov, J. Heyd, A. V. Krukau, G. E. Scuseria, *J. Chem. Phys.* **2006**, *125*, 074106.

260 O. A. Vydrov, G. E. Scuseria, J. P. Perdew, *J. Chem. Phys.* **2007**, *126*, 154109.

261 J. D. Chai, M. Head-Gordon, *J. Chem. Phys.* **2008**, *128*, 084106.

262 J. D. Chai, M. Head-Gordon, *Phys. Chem. Chem. Phys.* **2008**, *10*, 6615-6620.

263 M. A. L. Marques, E. K. U. Gross, *Primer in Density Functional Theory* **2003**, *620*, 144-184.

264 N. L. Doltsinis, in *Computational Nanoscience: Do It Yourself!*, ed. by J. Grotendorst, S. Blügel, D. Marx, John von Neumann Institute for Computing, Jühlich, **2006**, Vol. 31, pp. 357-373.

265 A. B. J. Parusel, A. Ghosh, *J. Phys. Chem. A* **2000**, *104*, 2504-2507.

266 A. B. J. Parusel, S. Grimme, *J. Porphyrins Phthalocyanines* **2001**, *5*, 225-232.

267 E. A. Perpète, V. Wathelet, J. Preat, C. Lambert, D. Jacquemin, *J. Chem. Theory Comput.* **2006**, *2*, 434-440.

268 J. Andzelm, B. C. Rinderspacher, A. Rawlett, J. Dougherty, R. Baer, N. Govind, *J. Chem. Theory Comput.* **2009**, *5*, 2835-2846.

269 D. Jacquemin, E. A. Perpète, G. E. Scuseria, I. Ciofini, C. Adamo, *J. Chem. Theory Comput.* **2008**, *4*, 123-135.

270 D. Jacquemin, V. Wathelet, E. A. Perpète, C. Adamo, *J. Chem. Theory Comput.* **2009**, *5*, 2420-2435.

271 D. Jacquemin, E. A. Perpète, I. Ciofini, C. Adamo, *Theor. Chem. Acc.* **2010**, 1-10.

272 D. Jacquemin, E. A. Perpète, I. Ciofini, C. Adamo, *J. Chem. Theory Comput.* **2010**, *6*, 1532-1537.

273 T. Darden, D. York, L. Pedersen, *J. Chem. Phys.* **1993**, *98*, 10089-10092.

274 U. Essmann, L. Perera, M. L. Berkowitz, T. Darden, H. Lee, L. G. Pedersen, *J. Chem. Phys.* **1995**, *103*, 8577-8593.

275 L. Verlet, *Phys. Rev.* **1967**, *159*, 98-103.

276 W. C. Swope, H. C. Andersen, P. H. Berens, K. R. Wilson, *J. Chem. Phys.* **1982**, *76*, 637-649.

277 R. W. Hockney, *Meth. Comput. Phys.* **1970**, *9*, 136-211.

278 I. D. Kuntz, J. M. Blaney, S. J. Oatley, R. Langridge, T. E. Ferrin, *J. Mol. Biol.* **1982**, *161*, 269-288.

279 A. R. Leach, *J. Mol. Biol.* **1994**, *235*, 345-356.

280 C. J. Epstein, R. F. Goldberger, C. B. Anfinsen, *Cold Spring Harb. Symp. Quant. Biol.* **1963**, *28*, 439-449.

281 C. Chothia, A. M. Lesk, *EMBO J.* **1986**, *5*, 823-826.

282 C. Sander, R. Schneider, *Proteins* **1991**, *9*, 56-68.

283 B. Rost, *Protein Eng.* **1999**, *12*, 85-94.

284 S. F. Altschul, W. Gish, W. Miller, E. W. Myers, D. J. Lipman, *J. Mol. Biol.* **1990**, *215*, 403-410.

285 W. R. Pearson, *Methods Enzymol.* **1990**, *183*, 63-98.

286 E. Krieger, S. B. Nabuurs, G. Vriend, in *Structural Bioinformatics*, ed. by P. E. Bourne, H. Weissig, Wiely-Liss, **2003**.

287 M. J. Frisch, G. W. Trucks, H. B. Schlegel, G. E. Scuseria, M. A. Robb, J. R. Cheeseman, J. A. M. Jr., T. Vreven, K. N. Kudin, J. C. Burant, J. M. Millam, S. S. Iyengar, J. Tomasi, V. Barone, B. Mennucci, M. Cossi, G. Scalmani, N. Rega, G. A. Petersson, H. Nakatsuji, M. Hada, M. Ehara, K. Toyota, R. Fukuda, J. Hasegawa, M. Ishida, T. Nakajima, Y. Honda, O. Kitao, H. Nakai, M. Klene, X. Li, J. E. Knox, H. P. Hratchian, J. B. Cross, C. Adamo, J. Jaramillo, R. Gomperts, R. E. Stratmann, O. Yazyev, A. J. Austin, R. Cammi, C. Pomelli, J. W. Ochterski, P. Y. Ayala, K. Morokuma, G. A. Voth, P. Salvador, J. J. Dannenberg, V. G. Zakrzewski, S. Dapprich, A. D. Daniels, M. C. Strain, O. Farkas, D. K. Malick, A. D. Rabuck, K. Raghavachari, J. B. Foresman, J. V. Ortiz, Q. Cui, A. G. Baboul, S. Clifford, J. Cioslowski, B. B. Stefanov, G. Liu, A. Liashenko, P. Piskorz, I. Komaromi, R. L. Martin, D. J. Fox, T. Keith, M. A. Al-Laham, C. Y. Peng, A. Nanayakkara, M. Challacombe, P. M. W. Gill, B. Johnson, W. Chen, M. W. Wong, C. Gonzalez, J. A. Pople, Gaussian 03, Gaussian, Inc., Pittsburgh PA, **2003**.

288 B. Mennucci, R. Cammi, J. Tomasi, *J. Chem. Phys.* **1998**, *109*, 2798-2807.

289 D. M. Chipman, *J. Chem. Phys.* **2000**, *112*, 5558-5565.

290 C. Etzlstorfer, H. Falk, N. Müller, W. Schmitzberger, U. G. Wagner, *Monatsh. Chem.* **1993**, *124*, 751-761.

291 C. Etzlstorfer, H. Falk, *Monatsh. Chem.* **1993**, *124*, 1031-1039.

292 J. Llano, J. Raber, L. A. Eriksson, *J. Photochem. Photobiol. Chem.* **2003**, *154*, 235-243.

293 S. D. Wetmore, R. J. Boyd, L. A. Eriksson, *Chem. Phys. Lett.* **2001**, *343*, 151-158.

294 J. Llano, L. A. Eriksson, *J. Chem. Phys.* **2002**, *117*, 10193-10206.

295 S. J. Marrink, O. Berger, P. Tieleman, F. Jahnig, *Biophys. J.* **1998**, *74*, 931-943.

296 Biocomputing at the University of Calgary, Structures and Topologies. http://moose.bio.ucalgary.ca/index.php?page=Structures_and_Topologies, File: dppc64.pdb (Accessed Dec. 1, 2007)

297 D. P. Tieleman, H. J. C. Berendsen, *J. Chem. Phys.* **1996**, *105*, 4871-4880.

298 M. Patra, M. Karttunen, M. T. Hyvönen, E. Falck, P. Lindqvist, I. Vattulainen, *Biophys. J.* **2003**, *84*, 3636-3645.

299 M. Patra, M. Karttunen, M. T. Hyvönen, E. Falck, I. Vattulainen, *J. Phys. Chem. B* **2004**, *108*, 4485-4494.

300 Biological Physics & Soft Condensed Matter Group of Prof. Mikko Karttunen, Dept. of Applied Mathematics, University of Western Ontario, SoftSimu - Downloads Zone. http://www.apmaths.uwo.ca/~mkarttu/downloads.shtml, File: dppc-128-100.pdb (Accessed Feb. 1, 2009)

301 S. J. Marrink, H. J. C. Berendsen, *J. Phys. Chem.* **1994**, *98*, 4155-4168.

302 E. Lindahl, B. Hess, D. van der Spoel, *J. Mol. Model.* **2001**, *7*, 306-317.

303 D. van der Spoel, E. Lindahl, B. Hess, G. Groenhof, A. E. Mark, H. J. C. Berendsen, *J. Comput. Chem.* **2005**, *26*, 1701-1718.

304 B. Hess, C. Kutzner, D. van der Spoel, E. Lindahl, *J. Chem. Theor. Comput.* **2008**, *4*, 435-447.

305 D. J. V. A. dos Santos, L. A. Eriksson, *Biophys. J.* **2006**, *91*, 2464-2474.

306 E. Erdtman, D. J. V. A. dos Santos, L. Löfgren, L. A. Eriksson, *Chem. Phys. Lett.* **2008**, *463*, 178-182.

307 A. M. Smondyrev, M. L. Berkowitz, *Biophys. J.* **1999**, *77*, 2075-2089.

308 J. M. Boggs, J. C. Hsia, *Biochim. Biophys. Acta* **1972**, *290*, 32-42.

309 E. Oldfield, M. Meadows, D. Rice, R. Jacobs, *Biochemistry* **1978**, *17*, 2727-2740.

310 D. Marsh, I. C. P. Smith, *Biochim. Biophys. Acta* **1973**, *298*, 133-144.

311 P. L. Yeagle, *Biochim. Biophys. Acta* **1985**, *822*, 267-287.

312 M. Pasenkiewicz-Gierula, T. Róg, K. Kitamura, A. Kusumi, *Biophys. J.* **2000**, *78*, 1376-1389.

313 T. Róg, M. Pasenkiewicz-Gierula, *Biophys. J.* **2001**, *81*, 2190-2202.

314 S. W. Chiu, E. Jakobsson, H. L. Scott, *J. Chem. Phys.* **2001**, *114*, 5435-5443.

315 S. W. Chiu, E. Jakobsson, R. J. Mashl, H. L. Scott, *Biophys. J.* **2002**, *83*, 1842-1853.

316 C. Hofsäss, E. Lindahl, O. Edholm, *Biophys. J.* **2003**, *84*, 2192-2206.

317 E. Falck, M. Patra, M. Karttunen, M. T. Hyvönen, I. Vattulainen, *Biophys. J.* **2004**, *87*, 1076-1091.

318 P. S. Niemelä, S. Ollila, M. T. Hyvönen, M. Karttunen, I. Vattulainen, *PLos Comput. Biol.* **2007**, *3*, 304-312.

319 J. P. Douliez, A. Leonard, E. J. Dufourc, *J. Phys. Chem.* **1996**, *100*, 18450-18457.

320 G. Gerebtzoff, X. Li-Blatter, H. Fischer, A. Frentzel, A. Seelig, *ChemBioChem* **2004**, *5*, 676-684.

321 H. Martinez-Seara, T. Róg, M. Karttunen, I. Vattulainen, R. Reigada, *PLos One* **2010**, *5*.

322 H. Tajiri, A. Hayakawa, Y. Matsumoto, I. Yokoyama, S. Yoshida, *Cancer Lett.* **1998**, *128*, 205-210.

323 O. Inanami, A. Yoshito, K. Takahashi, W. Hiraoka, M. Kuwabara, *Photochem. Photobiol.* **1999**, *70*, 650-655.

324 D. J. Granville, D. O. Ruehlmann, J. C. Choy, B. A. Cassidy, D. W. C. Hunt, C. van Breemen, B. M. McManus, *Cell Calcium* **2001**, *30*, 343-350.

325 D. Grebenova, K. Kuzelova, K. Smetana, M. Pluskalova, H. Cajthamlova, I. Marinov, O. Fuchs, J. Soucek, P. Jarolim, Z. Hrkal, *J. Photochem. Photobiol. B* **2003**, *69*, 71-85.

326 U. Rasmussen, S. B. Christensen, *Acta Pharm. Suecica* **1978**, *15*, 133-140.

327 O. Thastrup, P. J. Cullen, B. K. Drobak, M. R. Hanley, A. P. Dawson, *Proc. Ntl. Acad. Sci. USA* **1990**, *87*, 2466-2470.

328 Y. Sagara, G. Inesi, *J. Biol. Chem.* **1991**, *266*, 13503-13506.

329 Y. M. Khan, M. Wictome, J. M. East, A. G. Lee, *Biochemistry* **1995**, *34*, 14385-14393.

330 M. Floreani, A. Forlin, S. Bellin, F. Carpenedo, *Gen. Pharmacol.* **1996**, *27*, 873-878.

331 S. Paula, W. J. Ball, *Proteins* **2004**, *56*, 595-606.

332 M. Lape, C. Elam, M. Versluis, R. Kempton, S. Paula, *Proteins* **2008**, *70*, 639-649.

333 J. Deye, C. Elam, M. Lape, R. Ratliff, K. Evans, S. Paula, *Bioorg. Med. Chem.* **2009**, *17*, 1353-1360.

334 E. Krieger, K. Joo, J. Lee, J. Lee, S. Raman, J. Thompson, M. Tyka, D. Baker, K. Karplus, *Proteins* **2009**, *77 (Suppl. 9)*, 114-122.

335 E. Krieger, T. Darden, S. B. Nabuurs, A. Finkelstein, G. Vriend, *Proteins* **2004**, *57*, 678-683.

336 K. Obara, N. Miyashita, C. Xu, L. Toyoshima, Y. Sugita, G. Inesi, C. Toyoshima, *Proc. Natl. Acad. Sci. USA* **2005**, *102*, 14489-14496.

337 Molecular Operating Environment, Chemical Computing Group, Montreal, QC, **2009**.

338 H. Edelsbrunner, *Technical Paper of the Department of Computer Science of the University of Illinois at Urbana-Champaign; Urbana, Illinois.*

339 H. Edelsbrunner, M. Facello, R. Fu, J. Liang, Proceedings of the 28th Hawaii International Conference on Systems Science **1995**; pp. 256-264.

340 G. M. Morris, D. S. Goodsell, R. S. Halliday, R. Huey, W. E. Hart, R. K. Belew, A. J. Olson, *J. Comput. Chem.* **1998**, *19*, 1639-1662.

341 Y. Duan, C. Wu, S. Chowdhury, M. C. Lee, G. M. Xiong, W. Zhang, R. Yang, P. Cieplak, R. Luo, T. Lee, J. Caldwell, J. M. Wang, P. Kollman, *J. Comput. Chem.* **2003**, *24*, 1999-2012.

342 D. B. McIntosh, D. G. Woolley, B. Vilsen, J. P. Andersen, *J. Biol. Chem.* **1996**, *271*, 25778-25789.

343 M. J. Frisch, G. W. Trucks, H. B. Schlegel, G. E. Scuseria, M. A. Robb, J. R. Cheeseman, G. Scalmani, V. Barone, B. Mennucci, G. A. Petersson, H. Nakatsuji, M. Caricato, X. Li, H. P. Hratchian, A. F. Izmaylov, J. Bloino, G. Zheng, J. L. Sonnenberg, M. Hada, M. Ehara, K. Toyota, R. Fukuda, J. Hasegawa, M. Ishida, T. Nakajima, Y. Honda, O. Kitao, H. Nakai, T. Vreven, J. A. Montgomery, Jr., J. E. Peralta, F. Ogliaro, M. Bearpark, J. J. Heyd, E. Brothers, K. N. Kudin, V. N. Staroverov, R. Kobayashi, J. Normand, K. Raghavachari, A. Rendell, J. C. Burant, S. S. Iyengar, J. Tomasi, M. Cossi, N. Rega, J. M. Millam, M. Klene, J. E. Knox, J. B. Cross, V. Bakken, C. Adamo, J. Jaramillo, R. Gomperts, R. E. Stratmann, O. Yazyev, A. J. Austin, R. Cammi, C. Pomelli, J. W. Ochterski, R. L. Martin, K. Morokuma, V. G. Zakrzewski, G. A. Voth, P. Salvador, J. J. Dannenberg, S. Dapprich, A. D. Daniels, O. Farkas, J. B. Foresman, J. V. Ortiz, J. Cioslowski, D. J. Fox, Gaussian 09, Gaussian, Inc., Wallingford, CT, **2009**.

344 A. Klamt, G. Schüürmann, *J. Chem. Soc. Perkin Trans. 2* **1993**, 799-805.

345 V. Barone, M. Cossi, *J. Phys. Chem.* **1998**, *102*, 1995-2001.

346 M. Cossi, N. Rega, G. Scalmani, V. Barone, *J. Comput. Chem.* **2003**, *24*, 669-681.

347 C. Musewald, G. Hartwich, F. Pollinger-Dammer, H. Lossau, H. Scheer, M. E. Michel-Beyerle, *J. Phys. Chem.* **1998**, *102*, 8336-8342.

348 C. Geskes, G. Hartwich, H. Scheer, W. Mantele, J. Heinze, *J. Am. Chem. Soc.* **1995**, *117*, 7776-7783.

349 L. Limantara, S. Sakamoto, Y. Koyama, H. Nagae, *Photochem. Photobiol.* **1997**, *65*, 330-337.

350 R. Kobayashi, R. D. Amos, *Chem. Phys. Lett.* **2006**, *420*, 106-109.

351 N. Govind, M. Valiev, L. Jensen, K. Kowalski, *J. Phys. Chem. A* **2009**, *113*, 6041-6043.

352 G. Hartwich, L. Fiedor, I. Simonin, E. Cmiel, W. Schafer, D. Noy, A. Scherz, H. Scheer, *J. Am. Chem. Soc.* **1998**, *120*, 3675-3683.

353 K. A. Nguyen, P. N. Day, R. Pachter, *J. Chem. Phys.* **1999**, *110*, 9135-9144.

354 K. A. Nguyen, R. Pachter, *J. Chem. Phys.* **2001**, *114*, 10757-10767.

355 M. Merchán, E. Ortí, B. O. Roos, *Chem. Phys. Lett.* **1994**, *226*, 27-36.

356 J. Dalton, D. H. Slater, C. A. McAuliff, *Nature* **1972**, *235*, 388-392.

357 E. Scheie, A. Flaoyen, J. Moan, K. Berg, *New Zealand Vet. J.* **2002**, *50*, 104-110.

358 D. Casanova, F. P. Rotzinger, M. Gratzel, *J. Chem. Theory Comput.* **2010**, *6*, 1219-1227.

359 L. Petit, A. Quartarolo, C. Adamo, N. Russo, *J. Phys. Chem. B* **2006**, *110*, 2398-2404.

360 M. Palma, G. I. Cardenas-Jiron, M. I. M. Rodriguez, *J. Phys. Chem. A* **2008**, *112*, 13574-13583.

361 K. A. Nguyen, J. Kennel, R. Pachter, *J. Chem. Phys.* **2002**, *117*, 7128-7136.

362 M. Gouterman, G. Khalil, *J. Mol. Spectrosc.* **1974**, *53*, 88-100.

363 K. A. Nguyen, P. N. Day, R. Pachter, *J. Phys. Chem. A* **2000**, *104*, 4748-4754.

364 D. Sundholm, *Phys. Chem. Chem. Phys.* **2000**, *2*, 2275-2281.

365 O. Loboda, I. Tunell, B. Minaev, H. Ågren, *Chem. Phys.* **2005**, *312*, 299-309.

366 S. W. Young, K. W. Woodburn, M. Wright, T. D. Mody, Q. Fan, J. L. Sessler, W. C. Dow, R. A. Miller, *Photochem. Photobiol.* **1996**, *63*, 892-897.

367 E. A. Lukyanets, *J. Porphyrins Phthalocyanines* **1999**, *3*, 424-432.

368 A. D. Quartarolo, E. Sicilia, N. Russo, *J. Chem. Theory Comput.* **2009**, *5*, 1849-1857.